

5-2017

## Characterization of the RNAP Binding Sites on a $\lambda$ DNA using a Solid State Nanopore Combined with a Tuning Fork Force Sensing Probe Tip

Harpreet Kaur  
*University of Arkansas, Fayetteville*

Follow this and additional works at: <https://scholarworks.uark.edu/etd>



Part of the [Biophysics Commons](#)

---

### Citation

Kaur, H. (2017). Characterization of the RNAP Binding Sites on a  $\lambda$  DNA using a Solid State Nanopore Combined with a Tuning Fork Force Sensing Probe Tip. *Graduate Theses and Dissertations* Retrieved from <https://scholarworks.uark.edu/etd/1900>

This Dissertation is brought to you for free and open access by ScholarWorks@UARK. It has been accepted for inclusion in Graduate Theses and Dissertations by an authorized administrator of ScholarWorks@UARK. For more information, please contact [uarepos@uark.edu](mailto:uarepos@uark.edu).

Characterization of the RNAP Binding Sites on a  $\lambda$  DNA using a Solid State Nanopore  
Combined with a Tuning Fork Force Sensing Probe Tip

A dissertation submitted in partial fulfillment  
of the requirements for the degree of  
Doctor of Philosophy in Physics

by

Harpreet Kaur  
Panjab University, Chandigarh  
Bachelor of Science in Physics, Chemistry and Mathematics, 2006  
Punjabi University, Patiala  
Master of Science in Physics, 2008  
University of Arkansas  
Master of Science in Physics, 2016

May 2017  
University of Arkansas

This dissertation is approved for recommendation to the Graduate Council.

---

Dr. Jiali Li  
Dissertation Director

---

Dr. Surendra Singh  
Committee Member

---

Dr. Paul Thibado  
Committee Member

---

Dr. David McNabb  
Committee Member

---

Dr. Woodrow Shew  
Committee Member

## Abstract

In this dissertation, the binding positions of RNAP holoenzyme on  $\lambda$  DNA are characterized using an apparatus that integrates a Solid State Nanopore with a Tuning Fork based Force sensing probe (SSN-TFFSP). The SSN-TFFSP system combines the measurement of ionic current through a solid-state nanopore with a DNA tethered probe tip. The position of the tip is sensed by a tuning fork force sensor and is controlled with a nanopositioning system. With this apparatus, translocation speed of DNA through solid state nanopores has been brought down to 100  $\mu\text{s}/\text{base}$ . Such a controlled movement of DNA through a solid state nanopore can provide enough temporal resolution to determine the individual binding site of a RNAP on a  $\lambda$  DNA. Three signals measured simultaneously from this apparatus were: ionic current through a nanopore, tip position, and tip vibrational amplitude. These signals were measured when a probe tip was approaching towards the nanopore and was being lifted away from the pore. The  $\lambda$  DNA+ RNAP<sub>complex</sub> tethered to the probe tip can be captured by the electric field near a nanopore. The nanopore current signal measured during the capture of RNAP bound  $\lambda$  DNA provides new insights to the dynamics of  $\lambda$  DNA+RNAP<sub>complex</sub> molecules inside a nanopore. The binding positions of RNAP on a  $\lambda$  DNA are measured directly from the tip position signal corresponding to the distinct current drop within  $\lambda$  DNA current blockage level. The resolution limit of this apparatus is estimated to be 100 nm or 300 bp for RNAP binding sites. The resolution limit was further compared with the free translocation data set of  $\lambda$  DNA+RNAP<sub>complex</sub> through the solid state nanopore.

© 2017 by Harpreet Kaur  
All Rights Reserved

## Acknowledgments

ज्ञानशक्तिसमारूढः तत्त्वमालाविभूषितः ।  
भुक्तिमुक्तिप्रदाता च तस्मै श्रीगुरवे नमः ॥

“Salutation to that noble Guru, who is established in the power of knowledge, adorned with the garland of various principles and is the bestower of prosperity and liberation”.(<http://sanskrit.samskrutam.com/en.literature-shloka-guru-vandanaa.ashx>)

With this Sanskrit quote, first I would like to thank all my teachers who have taught me from pre School to PhD. I gratefully thank my adviser Dr. Jiali Li for all her support and encouragement to accomplish this project. I express my sincere gratitude to Dr. Surendra Singh and Dr. Reeta Vyas for extreme care and mental support that they have provided me through out my stay in Fayetteville. I would like to thank all of my committee members for being there for me.

I would like to acknowledge Dr. David McNabb and Dr. Ines Pinto for providing me access to their lab facilities for the preparation of DNA samples. Thank you to Dr. Min Xiao for letting me continue my experiments with a single molecule set up in his lab. I would like to thank Dr. Derek Stain at Brown University for providing me nanopores from his lab. Thanks a lot Mr. Richard W. Penhallegon and Mr. Brandon Rogers for all the quick help to fix my equipment so that I could perform my experiments without delay.

I would like to acknowledge Dr. Changbae Hyun, Dr. Tao Haung and Dr. Ryan Rollings for imparting the initial training in Dr. Li's lab. I would like to thank Santoshi Nandiwada and Mitu Chandra Acahrjee for providing nanopores for my experiments and Joel for all his care and midnight snacks that I took from his table during my experiments.

I can not thank my family members enough. I would like to express my deepest gratitude

to my mother, Mrs. Amrit Kaur, who taught me to value education. Thank you so much ma and papa for all your support and love at every step of my life. I express the greatest appreciation to my brothers Narinderpal Singh and Davinderpal Singh who have endlessly supported all my dreams with patience and love.

I feel fortunate to have a sister/best friend, Dr. Sarbjeet Makkar, with me for the past 13 years. Without her and her family's efforts, starting my PhD would not have been possible. I am indebted to them for all the love and unconditional support, they have given me as their own daughter. Aunti, Mrs. Jaspal Kaur ji, thank you so much for all your guidance and love.

Special Thanks to Sarbjeet Makkar and Mandeep Gill for sharing all of the great times at the beginning of my PhD program and taking care of me as a family during all the hard times.

Thank you, Desalgn Debu and Hemlin Swaran Rag, for all the useful discussions and training in Matlab. This last stretch of my PhD would not have been so smooth without you guys. Bala thanks a ton for all your help and care.

I am grateful to Hemlin for motivating me to push all the boundaries and continue in my endeavors.

Finally thanks to the, Physics Department, for giving me the opportunity to pursue a doctoral degree at the University of Arkansas.

## **Dedication**

“If the poor cannot come to Education, education must go to him”.  
Swami Vivekananda, 1863-1902

This dissertation is dedicated to all the children, who are deprived of Education.

# Contents

<b>Overview of the Dissertation</b>	<b>1</b>
<b>1 Introduction</b>	<b>2</b>
1.1 Nanopore as Genome Sequencer . . . . .	3
1.1.1 Detection Principle . . . . .	4
1.2 Challenges for Nanopore Sequencer: Single Nucleotide Resolution . . . . .	5
1.2.1 Spatial Resolution . . . . .	5
1.2.2 Temporal Resolution . . . . .	6
1.3 Progress towards Nanopore sequencing: . . . . .	6
1.3.1 Biological Nanopores . . . . .	6
1.3.2 Solid State Nanopores . . . . .	9
1.4 Other Applications of Nanopores . . . . .	11
1.4.1 Medical diagnosis . . . . .	11
1.4.2 Sensing proteins, peptides and nanoparticles . . . . .	12
1.4.3 Single Molecule Dynamics: DNA-Protein, Protein-Protein and Protein- Ligand interaction . . . . .	12
1.5 Conclusion . . . . .	13
<b>2 Controlled translocation of <math>\lambda</math> DNA with SSN-TFFSP apparatus</b>	<b>14</b>
2.1 Introduction . . . . .	14
2.2 Materials and Methods . . . . .	15
2.2.1 Tuning Fork as a force sensor . . . . .	15

2.2.2	Nanopore Fabrication . . . . .	20
2.2.3	Sample preparation . . . . .	23
2.2.4	Fluidic Chambers . . . . .	23
2.2.5	Nanopore - Tip alignment . . . . .	24
2.3	Results and Discussion . . . . .	27
2.3.1	Control translocation of DNA through nanopore . . . . .	27
2.3.2	Comsol Simulation . . . . .	31
2.3.3	Comparison with free translocation of $\lambda$ DNA . . . . .	33
2.4	Conclusion . . . . .	34
<b>3</b>	<b>Characterization of DNA tethered fiber tip</b>	<b>36</b>
3.1	Introduction . . . . .	36
3.2	Experimental setup and Methods . . . . .	38
3.2.1	Tip Fabrication . . . . .	38
3.2.2	Bottom Electrode . . . . .	40
3.2.3	Chamber . . . . .	41
3.2.4	Streptavidin-Biotin binding Chemistry . . . . .	41
3.2.5	DNA Preparation . . . . .	43
3.2.6	Fluorescent imaging . . . . .	44
3.2.7	DNA stretching setup . . . . .	45
3.3	Results and discussion . . . . .	47
3.3.1	Streptavidin Binding to tip . . . . .	47
3.3.2	Voltage and frequency dependence of DEP stretching . . . . .	47

3.3.3	Dependence of stretching Voltage on the distance between electrodes	49
3.4	Conclusion . . . . .	51
<b>4</b>	<b>Estimating binding efficiency of RNAP transcription factor at various positions on <math>\lambda</math> phage DNA using Solid-State Nanopores</b>	<b>53</b>
4.1	Introduction . . . . .	53
4.1.1	DNA Protein Interactions . . . . .	53
4.2	Experimental Setup . . . . .	56
4.3	Results and Discussion . . . . .	57
4.3.1	$\lambda$ DNA+RNAP <sub>complex</sub> Translocation: . . . . .	57
4.3.2	Comparison with RNAP <sub>bare</sub> and RNAP <sub>formaldehyde</sub> . . . . .	65
4.3.3	Comparison with $\lambda$ DNA <sub>bare</sub> and $\lambda$ DNA <sub>formaldehyde</sub> . . . . .	69
4.3.4	Subevent Analysis . . . . .	75
4.3.5	Relative position of RNAP on DNA . . . . .	78
4.4	Conclusion . . . . .	83
4.5	Materials and Methods . . . . .	83
4.5.1	Nanopore Fabrication . . . . .	83
4.5.2	Open pore Current and Current drop measurement . . . . .	84
4.5.3	Sample preparation . . . . .	85
<b>5</b>	<b>Sensing transcription factor binding sites on DNA with SSN-TFFSP apparatus</b>	<b>87</b>
5.1	Introduction . . . . .	87
5.2	Experimental Setup . . . . .	88

5.3	Results and Discussion . . . . .	90
5.3.1	Mapping RNAP position on $\lambda$ DNA . . . . .	90
5.3.2	Current Fluctuations while trapping . . . . .	96
5.3.3	Noise observed in Solid state nanopores . . . . .	99
5.3.4	Johnson Noise or Thermal Noise . . . . .	100
5.3.5	1/f Noise . . . . .	101
5.3.6	Comparison between current PSD . . . . .	103
5.3.7	TFFSP system Resolution to detect binding sites . . . . .	108
5.4	Conclusion . . . . .	109
<b>6</b>	<b>Summary</b>	<b>110</b>

## List of Figures

1.1	Experimental setup for a solid state nanopore detector . . . . .	7
2.1	Picture of a commercially available Quartz Tuning Fork . . . . .	15
2.2	Setup of a Tuning Fork Force Sensor Probe Tip . . . . .	16
2.3	Dependence of the output signal from tuning fork on driving frequency . . . . .	18
2.4	Schematics of the Ion Beam Sculpting nanopore fabrication procedure . . . . .	22
2.5	A schematic diagram of the top view of the fluidic chambers . . . . .	24
2.6	TEM images of the SiN <sub>x</sub> membrane window and a nanopore . . . . .	25
2.7	A drawing for the experimental setup of the SSN-TFFSP apparatus . . . . .	26
2.8	Experimental results for a controlled translocation of DNA through a SSN . . . . .	28
2.9	Experimental results for a controlled translocation of $\lambda$ DNA through a SSN of size 18 nm x 19 nm . . . . .	30
2.10	Comparison between the current recovery steps observed from the experiments and COMSOL simulations . . . . .	32
2.11	Experimental results for free translocations of the $\lambda$ DNA through a SSN . . . . .	33
3.1	Schematics show the effect of the electric field on the DNA surrounded by counter ions . . . . .	38
3.2	Optical Fiber fabrication . . . . .	39
3.3	SEM images of the gold coated tips . . . . .	40
3.4	The images of the bottom electrode and glass aquarium . . . . .	41
3.5	A 3D representation of Streptavidin-biotin complex dimer . . . . .	42
3.6	Oligomer design for $\lambda$ DNA ligation . . . . .	43

3.7	A schematic diagram of the DNA stretching setup . . . . .	46
3.8	A fluorescent image of the streptavidin absorbed tip . . . . .	48
3.9	Fluorescent images of the EtBr stained DNA attached to the tip . . . . .	49
3.10	Fluorescent images of the stretched $\lambda$ DNA between the tip and bottom electrode	50
4.1	Experimental setup for free translocations of the $\lambda$ DNA-RNAP <sub>complex</sub> mixture	58
4.2	Examples of different types of translocation events observed with $\lambda$ DNA-RNAP <sub>complex</sub> mixture . . . . .	60
4.3	$\Delta I_{max}$ versus $t_{dwell}$ scatter plot for various kind of events observed with $\lambda$ DNA-RNAP <sub>complex</sub> mixture . . . . .	61
4.4	Current and dwell time histograms of the all events observed $\lambda$ DNA-RNAP <sub>complex</sub> mixture through a nanopore of size 17 nm x 19 nm . . . . .	64
4.5	Experimental results for the $\lambda$ DNA+RNAP <sub>mixture</sub> translocations through a 23.7 nm by 20.4 nm pore at 120 mV . . . . .	66
4.6	Comparison between the tranlocation data sets obtained from RNAP <sub>bare</sub> and RNAP <sub>formaldehyde</sub> samples . . . . .	68
4.7	Comparison between the tranlocation data sets obtained from $\lambda$ DNA <sub>bare</sub> and $\lambda$ DNA <sub>formaldehyde</sub> samples . . . . .	70
4.8	Examples of the different types of translocation events observed with a peak within a $\lambda$ DNA translocation event . . . . .	74
4.9	Comparison between the current and $t_{dwell}$ histograms of the $\lambda$ DNA (which did not bind to RNAP in a $\lambda$ DNA+ RNAP <sub>mixture</sub> ), and $\lambda$ DNA+ RNAP <sub>complex</sub> events observed at 120 mV through a 23.7 nm by 20.4 nm nanopore . . . . .	76

4.10	Scheme for the selection of a subevent from an event. . . . .	77
4.11	Comparison between the relative subevent start times for $\lambda$ DNA+ RNAP <sub>complex</sub> , $\lambda$ DNA <sub>formaldehyde</sub> and $\lambda$ DNA <sub>bare</sub> events . . . . .	78
4.12	Current and $t_{dwell}$ histograms of RNAP level observed in $\lambda$ DNA + RNAP <sub>complex</sub> event . . . . .	79
4.13	Histograms of the estimated $x_{rel}$ position obtained from the various kind of $\lambda$ DNA+RNAP <sub>complex</sub> events . . . . .	80
4.14	Estimated positions of RNAP bound on $\lambda$ DNA using a solid state nanopore	82
5.1	A schematic drawing for the experimental setup of a controlled translocation of $\lambda$ DNA+RNAP <sub>complex</sub> with SSN-TFFSP apparatus. . . . .	89
5.2	Controlled translocation of a $\lambda$ DNA+RNAP <sub>complex</sub> through a 17 nm by 21 nm pore at 120 mV with 1 M KCl. . . . .	91
5.3	Controlled translocation of a $\lambda$ DNA+RNAP <sub>complex</sub> through the 17 nm by 21 nm pore at 60 mV with 1 M KCl . . . . .	93
5.4	Zoomed in view of the current signal through the 17 nm by 21 nm pore at 120 mV, and position of the tip, when tip is moving down or lifted up . . .	94
5.5	Zoomed in view of the current signal and position of the tip, when tip has brought down and lifted up several times. . . . .	95
5.6	Controlled translocation of a $\lambda$ DNA+RNAP <sub>complex</sub> through a 25 nm by 24 nm pore at 120 mV with 1 M KCl. . . . .	97
5.7	Zoomed in view of the current signals and the corresponding positions of tip, where RNAP bound to $\lambda$ DNA is trapped inside the nanopore. . . . .	98

5.8	Noise observed in the Solid State Nanopore current signal . . . . .	102
5.9	Comparison between the current power spectral densities plots obtained from the current signals observed at various situations during both the free, and controlled translocation of the molecules . . . . .	104
5.10	Comparison between the PSD signals obtained from the current signals observed at various situations during the controlled translocation of the DNA-RNAP complex. . . . .	107

## Overview of the Dissertation

This dissertation starts with a brief introduction to Nanopore based Sequencing technology. I have addressed the technical challenges before nanopore sequencing device availability and the research progress made in the past two decades by both biological nanopore and solid state nanopore to achieve a low cost (below \$1000) and fast sequencing goal. In order to improve the temporal resolution of solid state nanopore, our lab has designed an apparatus that combines solid state nanopores with a tuning fork force sensing probe system. Chapter two extensively describes the experimental setup of this apparatus. The controlled translocation of  $\lambda$  DNA through solid state nanopore is explained in detail and COMSOL simulations were performed to support our explanation of current measurement results. Chapter 3 discusses another experimental setup designed to test binding chemistry between the DNA and tip. The ac voltage dependence on the stretching of the DNA bound to the gold coated optical fiber tip is presented.

Chapter 4 and Chapter 5 are the core of this dissertation. Chapter 4 is based on free translocation of  $\lambda$  DNA+RNAP<sub>complex</sub> through native solid state nanopore set up. These translocation events were further compared with RNAP and  $\lambda$  DNA events. The binding efficiency and binding sites of RNAP on  $\lambda$  DNA were estimated.

Chapter 5 describes the translocation of  $\lambda$  DNA+RNAP<sub>complex</sub> tethered to the probe tip through solid state nanopore. This new approach to find binding sites of protein on DNA with high accuracy was demonstrated. The resolution limit to find the binding sites of RNAP for this apparatus was estimated. Finally, I conclude with a short summary of this work.

## Chapter 1

### Introduction

Deoxyribonucleic Acid (DNA), is a bio-molecule that carries hereditary information in almost all living organisms. The genetic information stored in DNA, is coded with four different chemical bases (or nucleotides) Adenine (A), Thymine (T), Cytosine (C) and Guanine (G). Nucleotides are bound to each other via covalent bonds between the sugar part of one nucleotide and phosphate group of the next one, to form a long chain. Two strands of DNA wind around each other to form a double helix structure which was revealed by Watson and Crick [1] from X ray diffraction data obtained by Roselyn E. Franklin. An accurate information of DNA base pair's sequence is essential for many research fields like biology, medical diagnosis, forensic biology, evolution biology and virology. In 1977, Sanger reported the first full genome sequence of bacteriologic  $\phi$ X174 using the chain termination approach [2]. Knowledge about human genome sequence has improved our understanding of many genetic diseases, like cancer, and has opened the doors for personalized genome medicine. In 2004, the National Human Genome Research Institute launched the "\$1000 genome project" to expand next generation sequencing (NGS) techniques, such that a human genome can be sequenced rapidly for less than \$1000. Schadt.et.al have characterized the NGS into three generations [3]. First generation sequencing based on Sanger's approach: has a read length of 400-900 bp with 99.9% accuracy at a cost of \$2400 per million bases [4]. The 2nd generation sequencing techniques are based on amplification of target DNA and large numbers of parallel chips. Even though 2nd generation sequencing is less than \$1000, DNA read length is limited to few hundred bases and it takes long time [5].

To overcome limitations of 1st or 2nd generations, new technologies are growing rapidly to develop a sequencer at the single molecule level and are known as 3rd generation sequencing techniques. Some of these techniques are Nanopore sequencing [5, 6], single molecule motion [7], molecular force spectrometry [8], sequencing by tip enhanced Raman scattering [9] etc. These techniques do not involve long sample preparation steps. Nanopore based technology has gained a lot of attention due to label free detection, no prior amplification of sample, small volume of sample, longer DNA read length and high speed of detection [5].

### 1.1 Nanopore as Genome Sequencer

Passage of ion and biomolecules (like DNA, RNA and proteins) through the cell membrane is an important biological process. Transportation of RNA through the cell membrane after its synthesis is an example of this. Inspired by translocation processes of DNA through the membrane ion channel, Deamer et. al. envisioned the potential of nanopore as a next generation Genome sequencer in 1990 [10, 11]. Six years later, Deamer and coworkers reported the first experimental results on single strand (ss) DNA detection through  $\alpha$  Hemolysin ( $\alpha$ -HL) nanopore [12].  $\alpha$ -HL is a mushroom shaped heptamer trans membrane channel and is termed as a biological nanopore as it is made up amino acid residues. It has a  $\beta$  barrel with an outer diameter of 2.6 nm on one end (shown in Fig. 1.1(a)) [13] and an inner diameter of 1.3 nm which is equivalent to the diameter of ssDNA.

In order to overcome, protein pore's stability and precise tuning of nanopore size problems, Li et. al. reported the first Silicon Nitride ( $\text{SiN}_x$ ) based solid state nanopore (SSN) with a size of 1.8 nm fabricated with an Ion Beam Sculpting (IBS) apparatus [14]. Two years after that, they demonstrated the sensing capacity of SSN to identify double strand DNA (ds-

DNA) with different configurations as it passes through the nanopore [15]. A transmission electron microscope (TEM) image of the 30 nm  $\text{SiN}_x$  nanopore with a thickness of 20 nm is shown in Fig. 1.1(b) and 1.1 (c).

### 1.1.1 Detection Principle

Nanopore sensor detection is based on the combination of ion channel [16] and resistive pulse technique, discovered by Walter Coulter to count blood cells [17]. A nanometer sized pore,  $\alpha$ -HL embedded in a biological membrane or  $\text{SiN}_x$  in silicon chip is the sole connection between cis and trans chambers containing electrolyte solution. Upon the application of external voltage across a nanopore, ions flow through and a steady open pore current,  $I_o$  (baseline current), is detected by patch clamp amplifier (PCA).  $I_o$  depends upon the pore geometry and solution conductivity,  $\sigma$ . For the simplest case, assuming a cylindrical geometry, at applied voltage,  $V$ , an expression for  $I_o$  can be obtained using Ohms law [18]:

$$I_o = \frac{V\sigma\pi r_p^2}{t_p} \quad (1.1)$$

where  $r_p$  and  $t_p$  are the radius and thickness of the nanopore, respectively. The basic set up of a SSN translocation experiment is shown in Fig. 1.1(d). If negatively charged biomolecules like DNA (-0.33e/phosphate) [19] are added to the cis side (which is grounded), an electric field across the pore length forces the biomolecules to move to the positively biased trans side. As DNA translocates through the pore,exclusions of ions from the nanopore results in a transient current drop,  $\Delta I$ .  $\Delta I$  is proportional to the ratio of the cross sectional area of linear DNA chain with respect to the nanopore cross-sectional area [15], and can be written as,

$$\Delta I = \frac{V\sigma\pi r_{DNA}^2}{t_{DNA}} \quad (1.2)$$

where  $r_{DNA}$  is the radius of DNA. This current blockage is known as a translocation event. An example of a translocation event of  $\lambda$  DNA through SSN with  $I_o = 9.7$  nA is shown in Fig. 1.1(e). When  $\lambda$  DNA passes through the pore it causes a current blockage,  $\Delta I = 200$  pA with translocation time,  $\tau_d \approx 3$  ms. For SSN, translocation time increases with an increase in the length of DNA ( $L_{DNA}$ ) and solution viscosity ( $\eta$ ) and varies inversely with applied voltage ( $V$ ) and linear charge density ( $\zeta$ ) [20–22]. An approximate expression for  $\tau_d$  for SSN can be written as,

$$\tau_d = \frac{\eta L_{DNA}^\alpha}{V\zeta} \quad (1.3)$$

where the parameter  $\alpha \approx 1.4$ , is measured empirically and it signifies the unwinding of the DNA region just before it passes through the pore [22]. Measurement of the current blockage and translocation time provides insight on the translocation dynamics of DNA molecules through a nanopore. To successfully finger-print a genome sequence, DNA should thread through a nanopore, such that from the current signature one can read off a single base at a time.

## 1.2 Challenges for Nanopore Sequencer: Single Nucleotide Resolution

### 1.2.1 Spatial Resolution

Nucleotides in the DNA chain are separated by  $\approx 0.4$  nm from each other. Each monomer has a different size and ideally a distinct blockage current from each nucleotide is expected to read the genome sequence successfully. Point to note is that the thickness of the  $\beta$  barrel

of  $\alpha$ -HL is  $\approx 5$  nm and it can accommodate  $\approx 10$  bases. The corresponding thickness for SSN is about 20 nm, which is capable of housing tens of nucleotides at a time. So, the current blockage is intrinsically an average outcome of a small portion of DNA, not from a single nucleotide. Any fine details smaller than pore thickness are effectively averaged out in current blockage signal. One solution to increase the spatial resolution of the nanopore sensor is to reduce the thickness of the nanopore.

### 1.2.2 Temporal Resolution

The sampling rate of commercially available PCA is lower than 250 kHz. At 120 mV, translocation speed of the ssDNA through the  $\alpha$ -HL nanopore is  $\approx 1$  base/ $\mu$ s [23] and through the SSN, it is about 25 bases/ $\mu$ s [15, 21]. This speed is too fast to detect a single nucleotide by PCA. Along with spatial resolution, it is critically important to slow down the translocation speed of DNA or improve the electronics for faster data collection, to achieve single nucleotide resolution (SNR).

## 1.3 Progress towards Nanopore sequencing:

### 1.3.1 Biological Nanopores

Over the past 2 decades, a tremendous amount of work has been done to improve temporal and spatial resolutions of both biological and solid state nanopores. Stoddart et.al demonstrated that the  $\alpha$ -HL channel contains three recognition sites [24]. With the help of modern molecular biological techniques, like genetic engineering, mutations were introduced in  $\alpha$ -HL to eradicate excess recognition sites and produced a single detection site inside the chan-

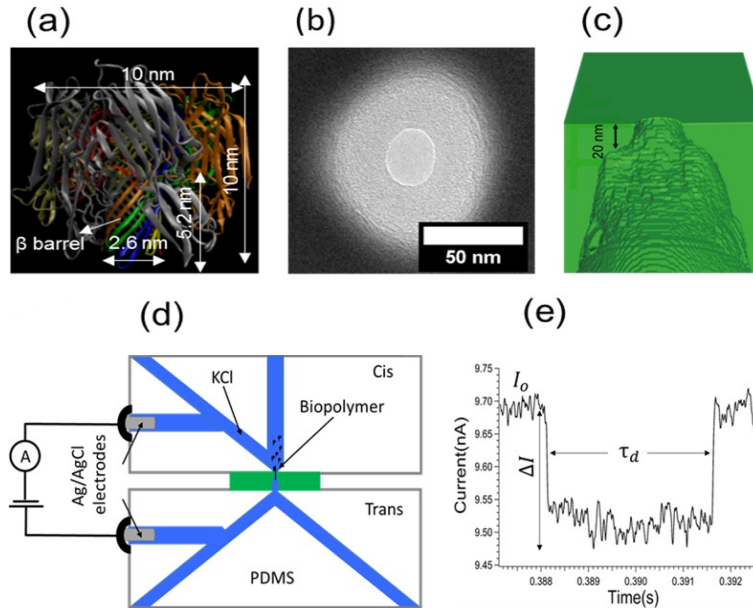


Figure 1.1: (a) A 3D representation of  $\alpha$ -HL mushroom shaped heptamer (each unit is shown in different color)(3B07.pdb) [13]. With a 10 nm by 10 nm external dimensions,  $\alpha$ -HL has a  $\beta$  barrel with an outer diameter of 2.6 nm and a length of 5.2 nm. (b) A TEM image of a SSN nanopore with a diameter of 30 nm. (c) Electron tomograph of the 30 nm pore shows the thickness of the pore is  $\approx 20$  nm. (d) A schematic view of fluidic setup of the nanopore experiment. Polydimethylsiloxane (PDMS) chambers above (Cis) and below (Trans) the silicon chip make a tight seal with pore and contain channels for the fluid flow and biopolymer insertion. (e) Current trace of a translocation event of  $\lambda$  DNA through SSN. As  $\lambda$  DNA translocates through the nanopore channel a temporary current blockage,  $\Delta I = 200$  pA with a duration of  $\tau_d \approx 3$  ms is detected.

nel [25]. Faller et. al. reported another funnel shape octamer protein pore, *Mycobacterium smegmatis* porin A (MspA) with a diameter of  $\approx 1.2$  nm, thickness 0.6 nm at the detection site [26]. MspA's single recognition site makes it a promising candidate to improve the spatial resolution of ssDNA sequencing [27, 28]. The current drop observed from MspA is reported to have a contribution from four bases in the detection site [28, 29]. To increase the capture rate and to slow down DNA, Butler et. al. muted MspA in such a way that amino acid residues at the entrance are positively charged, and at the recognition site are neutral [30]. To control the translocation speed, many groups have combined nanopore with ratchet dynamics of DNA polymerase, which was proposed by Church et. al. [11]. For example: Manrao et. al. used *Mycobacterium smegmatis* porin A (MspA), a protein pore with phi29 DNA polymerase bound to a blocking oligomer and a DNA template (whose 3' end is annealed with another primer) [29]. Once the single strand part of the complex is trapped in MspA and the blocking oligomer is removed, phi29 pull the single stranded template at a controlled rate to resolve the single nucleotide signal [29]. Nanopore based DNA sequencing has also been practically demonstrated with biological nanopores along with various modifications of the traditional translocation experiment [31, 32]. Kumar et. al. described the nanopore based DNA sequencing via synthesis strategy by using 5 phosphate nucleotides modified with different size tags [32]. During the polymerase reaction, whenever a nucleotide is added to the DNA chain, it releases its tag into the alpha-hemolysin nanopore and generates a distinct current blockage signal for each nucleotide [32]. Oxford Nanopore Technologies launched the DNA sequencing device, MinION, based on base by base ratcheting of ssDNA out of  $\alpha$  Hemolysin pore using  $\phi$ 29 polymerase. According to initial reports on MinION sequencing, it has a capacity to read more than 10 kb, which is much longer than average read length of

other sequencing techniques. However, the error rate is as high as 90% [33]. Recently, Laver *et. al* have assessed the MinION sequencing performance. They have reported the mean read length to be 2 kb and the longest single read length to be 98 kb with an estimate error of 38.5% [34].

### 1.3.2 Solid State Nanopores

On the other hand, solid state nanopores have lagged far behind to achieve SNR for DNA sequencing. Since the fabrication of  $\text{SiN}_x$  nanopores by Li [14], SSN has gained a lot of attention due to its thermal stability, mechanical robustness and selectable chemistry. Apart from this, different nano-fabrication techniques have provided freedom to have a precise control on the dimensions of nanopores. Many groups have demonstrated the fabrication of silicon oxide [35], aluminum oxide [36] and single layer membranes like graphene [37–39] and boron nitride [40] nanopores by using various techniques like focused ion beam, electron beam lithography, focused electron beam, and helium ion microscopy. Drndics group have reported silicon nitride pores as thin as 1.7 nm [41] and recent work of Garaj *et. al.* demonstrate that atomically thin graphene nanopore has a high sensitivity of  $0.65 \text{ nA}/\text{\AA}$ , which can detect the small changes on DNA [42]. The 0.335 nm thick single layer graphene [43] is an excellent alternative for artificial nanopore based DNA sequencing.

Due to weaker interactions between the DNA and SSN, dsDNA translocates at a much faster rate of 25 bases/ $\mu\text{s}$  [15, 21] through SSN compared to the protein pores. Our group has reported the first attempt to control the translocation speed of DNA through SSN by increasing solvent viscosity and a translocation speed of 3 bases/ $\mu\text{s}$  was achieved [18]. But, increasing the viscosity of buffer also reduces ionic current signal and, hence, signal to noise

ratio. After this, many experiments with separate DNA manipulation have been designed to slow down DNA motion through SSN. For example, DNA translocation was observed while tethered to a bead and the motion of the bead was controlled by using optical or magnetic tweezers [44–46]. Trepangnier et. al. showed that translocation speed could be controlled to  $0.15 \text{ bases}/\mu\text{s}$ ,  $\approx 200$  times slower than traditional DNA translocation [45]. In Optical tweezers experiments, DNA tethered to a bead was trapped in a focused laser beam but, heating by the laser resulted in an increase in the ionic current and noise of the nanopore signal [44]. To compensate for these effects, optically trapped bead need to be placed a few microns away from the nanopore. Additionally, Brownian motion of the bead limits the positional control of tweezers to 10 nm.

To achieve the goal of DNA translocation as slow as  $0.001 \text{ base}/\mu\text{s}$  for a SSN based DNA sequencer, our group has constructed an apparatus that integrates the SSN ionic current measurement with a DNA tethered Tuning fork based force sensing probe (TFFSP) tip [47](Discussed in Chapter 2). Position of the probe tip is sensed by the tuning fork force sensor and controlled by a nanopositioning system with sub-nanometer precision. The advantage of the probe tip based approach over the bead-based system is that probe tip can be brought very close to nanopore and pulled out with a sub-nanometer resolution [48, 49]. With a SSN-TFFSP setup, a translocation speed of  $0.0025 \text{ bases}/\mu\text{s}$  or  $1 \text{ nm}/\text{ms}$  can be achieved, 1000 times slower than free DNA translocation and 10 times slower than bead based optical trapped DNA in SSN. Another point to note here is that, this is not the upper limit of SSN-TFFSP system, pulling rate can be reduced further by changing the user-defined parameters for the nanopositioning system. Our system provides enough temporal resolution ( $400 \mu\text{s}/\text{base}$ ) to read a single nucleotide through a pore with commercially available PCA

at a 100 kHz (10  $\mu$ s) sampling rate.

## 1.4 Other Applications of Nanopores

Application of nanopore sensing technique is not only limited to DNA sequencing, it has been proved to be useful for a broad range of purposes. Some of its applications are listed below.

### 1.4.1 Medical diagnosis

DNA methylation can cause disordered gene expression leading to mutations and tumorigenesis so it can be used as a biomarker for cancer diagnosis. Abnormal DNA methylation has been demonstrated using SSN by measuring translocations of unmethylated, methylated and semimethylated MS3 and BRCA1 DNA fragments [50]. It was observed that minimum voltage to translate DNA varies with degree of methylation [50]. This simple technique can be used as an important tool for epigenesis diagnosis.

It has been reported that single nucleotide polymorphisms (SNP) can cause phenotypic differences among individuals and is related directly to tumor progression [51]. Zhao.et. al observed that the voltage threshold for the translocation of DNA bound to a restriction enzyme depends upon the DNA sequence and enzyme, which allowed for the detection of the SNP in the recognition site [51]. This concept can be extended to diagnose early bacterial and viral infections, and cancer. Nanopore detection technique can also be extended for pathogen classification [52].

A high speed cocaine detector was proposed by combining long tail Cocaine Binding Aptamer (CBA) with  $\alpha$ -Hemolysin nanopore [53]. When CBA is combined with cocaine, it forms

a three way junction complex and blocks current permanently, indicating the presence of cocaine [53].

#### **1.4.2 Sensing proteins, peptides and nanoparticles**

Protein [54–56] and nano-sized particle characterization [57–59] through nanopores have also been investigated with high interest. Translocation of protein through nanopore is complex due to fast passage time and interactions with surfaces [56]. Recently, lipid coated nanopores have been reported to be able distinguish several proteins by measuring five parameters; translocation time, charge, volume, shape and ligand affinity [55]. The Akesson's group has described the controlled unfolding of protein through a  $\alpha$  Hemolysin pore in combination with AAA<sup>+</sup> and unfoldase ClipX [60]. This technique has the capacity to sequence native single protein strands and could prove useful for developing nanopore based proteomics studies.

#### **1.4.3 Single Molecule Dynamics: DNA-Protein, Protein-Protein and Protein-Ligand interaction**

The capacity to scan and determine the features on an individual polymer makes nanopore sensor a suitable candidate to study the DNA- protein complexes. DNA coated with RecA proteins [61–63], and a single large protein like RNAP [64], biotin [65] and ligands [66] bound to DNA molecules have been studied with SSN. Binding of the restriction enzymes [51, 67], restriction endonucleases [68], and histones [69] to the DNA molecules have been investigated with Nanopore Force Spectroscopy experiments using voltage driven removal of protein.

Apart from the above mentioned applications: nanopores are described to study the mechanism of viral DNA packing [70, 71] and can be used to understand essential biological

processes like stimulation of ion transport in organisms with bio-mimetic nanochannel devices.

## 1.5 Conclusion

Nanopore based biosensor has been used for identification and quantification of a wide range of analytes. Research efforts in the past two decades, biological nanopores have led to the successful application of biological nanopores, which can sequence DNA with a long read length quickly. The MinION sequencer launched by the Oxford nanopore is in clinical trial. Early assessment of MinION sequencing data suggests long read lengths of DNA but a high error rate. On the other hand, artificial nanopore based sequencing technologies although are, progressing at a fast pace but have yet to reach single nucleotide resolution. With the present progressing rate, we can anticipate fast and inexpensive clinical sequencing to be available in the near future. Apart from sequencing, many types of DNA-Protein, Protein-Protein interaction mechanisms, and the possibility of other medical diagnosis applications have been explored using single molecule nanopore detectors.

## Chapter 2

### Controlled translocation of $\lambda$ DNA with SSN-TFFSP apparatus

#### 2.1 Introduction

As explained in Chapter 1, reducing the translocation speed of the DNA molecule through SSN is an important research problem within the nanopore scientific community. Several methods have been adopted to control the motion of DNA through SSN for single nucleotide resolution. These methods involve combination of optical or magnetic tweezers or scanning probe microscopy with SSN current measurement. Scanning probe microscopy (SPM) is an important research technique, which uses a probe tip to scan the surface morphology of a sample with high resolution [72, 73]. The interaction between the probe tip and sample depends on the distance between the tip and sample and is used as a feedback back to control the gap between the tip and sample surface. SPM has been demonstrated to provide a high resolution in liquid environments for example, by imaging the dynamics of DNA transition between H and B forms in aqueous solutions [74]. SPM had been integrated with an electrolyte immersed SSN to study the tip-nanopore interaction [49], the lipid bilayer on a nanopore [75, 76] and access resistance of nanopore [48]. Our lab has developed a new technique that combines solid state nanopore with a tuning fork force sensing probe (SSN-TFFSP). The SSN-TFFSP set up utilizes the force sensing mechanism of SPM by tethering dsDNA on to a gold coated tip attached to a tuning fork, to control DNA translocation through the nanopore. This chapter discusses the experimental set up of the SSN-TFFSP apparatus and the controlled translocation of  $\lambda$  DNA through the nanopore at a speed of  $1000 \mu\text{s}/\text{bp}$  or less. With a controlled speed passage, new insights from DNA capture and

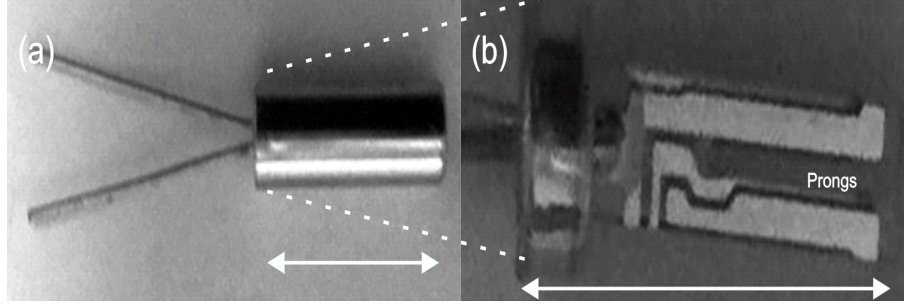


Figure 2.1: (a) Metal encapsulated commercially available Quartz Tuning Fork. (b) Enlarged photograph of the Quartz Tuning Fork removed from the metal capsule. Scale bar: width of the arrowhead line is 7 mm (for both (a) and (b)).

release mechanisms through SSN are also explained.

## 2.2 Materials and Methods

### 2.2.1 Tuning Fork as a force sensor

The micro fabricated quartz tuning forks were designed as frequency resonator for crystal watches. A commercially available quartz tuning fork operating at 32768 Hz is encapsulated in the metal capsule, to provide protection against environmental humidity and other possible deposits. Fig. 2.1(a) is the picture of a Tuning fork purchased from Fox electronics, NC38LF-327. Fig. 2.1(b) shows the image of the Tuning fork taken out from its packing. Like a traditional tuning fork, Quartz tuning fork consists of two micro machined quartz element prongs (Right side of Fig. 2.1(b)) supported by epoxy mounting at the base (Left side of Fig. 2.1(b)). The Quartz Tuning fork with a tip attached to one of it's prongs, can be used as force sensor [77–80]. Quartz is a piezoelectric material, mechanical vibration of its prongs induces electric signal and vice-versa. An external electrical circuit can be used to measure the output electric current or voltage signal. We make use of the Piezo actuator

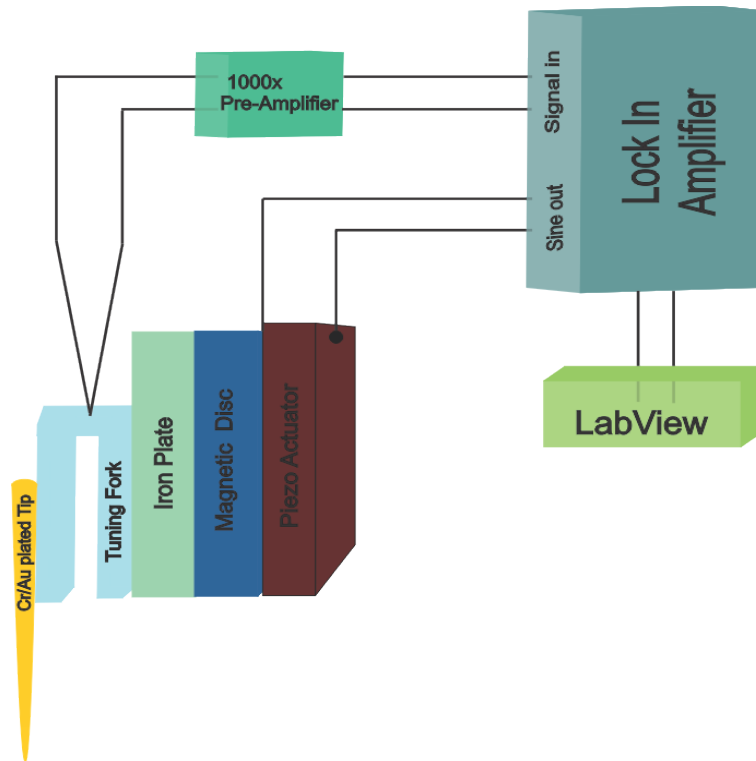


Figure 2.2: Set-up of Tuning Fork Force Sensor: The piezo actuator is driven by the sine output from a lock-in Amplifier, which oscillates the tuning fork. The output signal from the tuning fork sensor is first amplified 1000x and measured by the Lock in Amplifier.

(PI, PQYY 0427) to mechanically excite the tuning fork at a resonance frequency. The schematic diagram of the tuning fork force sensor set-up is shown in Fig. 2.2. The piezo actuator is driven by sine output from a Lock-in amplifier (Standford Research Systems, SR850). The amplitude of driving sine signal was used between 20 mV-60 mV. A magnetic disc was attached to the piezo actuator. A gold plated tip was glued to one of the tuning fork prongs, which was glued to the iron plate. The magnetic disc and iron plate were used for the convenience of attaching and detaching the tuning fork from the piezo-actuator. Once the piezo excites the tuning fork, it oscillates at resonance frequency. Output signal from the tuning fork was 1000 times pre-amplified and finally detected by the lock-in amplifier. In the metallic capsule, the tuning fork vibrated at resonant frequency of 32768 Hz with a Quality

factor ( $Q$ ) of  $10^5$ . Once the tuning fork was out of metal capsule packing and was glued to the iron plate, the resonance vibrational amplitude and quality factor was decreased with a shift in the resonance frequency. To find the resonance peak of the tuning fork output signal, the LabVIEW program was used to scan the tuning fork over a wide range of driving frequency. An output signal from the tuning fork sensor is shown in Fig. 2.3(a) when no tip was attached to tuning fork. A 20 mV piezo driving signal was used to excite the tuning fork, a vibrational amplitude of 0.622 V at a resonant frequency 32760 Hz with a  $Q$  factor of 2520 was observed as output. When the tip was glued on one of the tuning fork's prongs, the amplitude of the vibration and  $Q$  factor were reduced further due to extra mass on one of the prongs along with a large shift in the resonance frequency. Fabrication process for optical fiber tips is discussed in the next chapter. An example of vibrational amplitude of the tuning fork with probe tip as a function of driving frequency is shown in Fig. 2.3(b). Note that the tuning fork is the same for both Fig. 2.3(a) and 2.3(b). With a probe tip attached, the amplitude of the vibration dropped from 0.622 V to 0.366 V. The resonance frequency shifted to 29200 Hz from 32760 with a reduced  $Q$  factor of 495.

It is known that when a probe tip vibrates parallel to the sample surface, and as the tip nears the sample surface, its vibrational amplitude and quality factor decreases and resonance frequency shifts. The nature of the shear forces near the sample surface is still under debate. The tuning fork based shear force feedback system is used as a distance control mechanism in scanning microscopes like Near field Scanning Optical Microscope (NSOM), and Atomic Force Microscopy (AFM). The motion of a prong of the tuning fork can be modeled as an

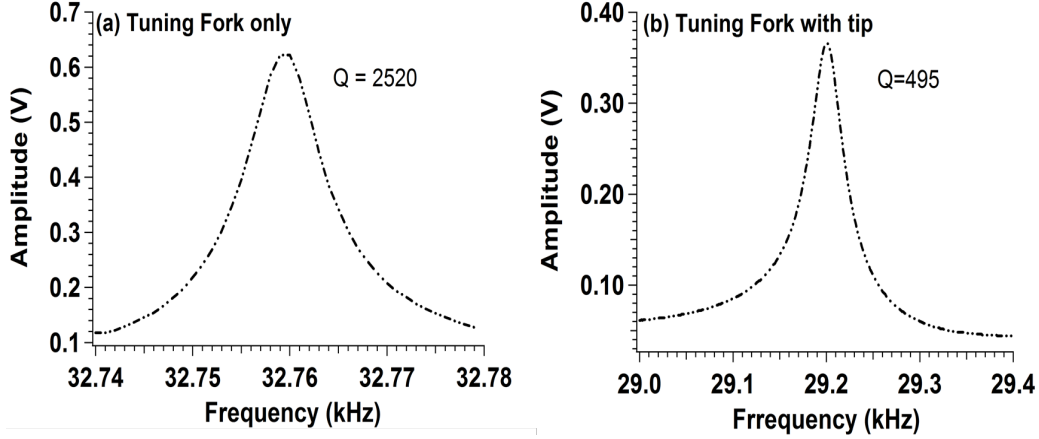


Figure 2.3: Amplitude of the piezo electric signal from a Tuning fork as a function of driving frequency (a) Without a tip and (b) With a tip attached to one of tuning fork's prongs. Piezo driving signal for both the cases is 20 mV. The same tuning fork was used for both measurements.

effective harmonic oscillator given by

$$m_e \ddot{x}(d, t) + F_D + m_e \omega_0^2 x = F e^{-i\omega t} \quad (2.1)$$

where  $m_e$  is the effective mass of the prong,  $F$  is the amplitude of the driving force,  $\omega_0$  is the resonance frequency and  $F_D = m_e \gamma(d) \dot{x}(d, t)$  is the sum of all the drag forces with  $\gamma(d)$  as damping constant. The parameter  $d$  indicates the distance between the probe and surface.

For small drag, steady state solution of Eq. 2.1 is given by

$$x(t) = \frac{F e^{-i\omega t}}{m_e (\omega_0^2 - \omega^2 - i\gamma\omega)} \quad (2.2)$$

Oscillation amplitude  $x(t)$  has a Lorentz dependence on  $\omega$ , and is in good agreement with the  $\omega$  dependent measurement of  $x(t)$  shown in Fig. 2.3. At a distance  $d$ , drag force can be written as the sum of two factors [81] (1)  $\gamma_{stat}$ , contribution due to the physical properties of the tuning fork like dimensions and material, and (2)  $\gamma_{int}$ , due to the probe-sample interaction, which

depends upon the distance between sample and probe tip.

$$\gamma(d) = \gamma_{stat} + \gamma_{int}(d) = \frac{F}{m_e \omega_0(d) x_0(d)} \quad (2.3)$$

where  $x_0(d)$ , is the oscillation amplitude at resonance frequency  $\omega_0(d)$  at distance  $d$  from the sample. As  $d \rightarrow \infty$ , the contribution to drag force due to probe/sample interaction is almost negligible ( $\gamma_{int}(\infty) = 0$ ) which implies that

$$\gamma_{int}(d) = \gamma_{stat} \left[ \frac{\omega_0(\infty) x_0(\infty)}{\omega_0(d) x_0(d)} - 1 \right] \quad (2.4)$$

where  $x_0(\infty)$  is the oscillation amplitude at a resonance frequency  $\omega_0(\infty)$  at distance far away from the sample. Using Eq. 2.2, frictional drag force (Probe is vibrating parallel to the surface) due to the interaction between the sample and probe at a distance  $d$  from the sample surface can be written as

$$F_{int}^{frictional}(d) = m_e \gamma_{int}(d) \omega_0(d) x_0(d) = F \left[ 1 - \frac{\omega_0(d) x_0(d)}{\omega_0(\infty) x_0(\infty)} \right] \quad (2.5)$$

Using Eq. 2.2 to calculate oscillation amplitude at resonance frequency, definition of quality factor as  $Q = \omega_0 / \gamma \sqrt{3}$  [81] and  $m_e = k / \omega_0^2$  (where  $k$ , is the effective spring constant of the tuning fork) one can write the exact expression for  $F_{int}^{frictional}$

$$F_{int}^{frictional}(d) = \left[ 1 - \frac{\omega_0(d) x_0(d)}{\omega_0(\infty) x_0(\infty)} \right] \frac{k x_0(\infty)}{\sqrt{3} Q(\infty)} \quad (2.6)$$

The change in resonance frequency is much smaller than the change in oscillation amplitude, hence one can omit the dependence of resonance frequency from Eq. 2.6. Then one finds that the oscillation amplitude of the tuning fork is directly proportional to the piezoelectric

output voltage signal and is given by [82, 83],

$$\frac{\text{output voltage}}{\text{amplitude}} = 2\pi f R \left[ 24d_{21}kL_e \left( \frac{L_e}{2} - L \right) \frac{1}{T^2} \right] \quad (2.7)$$

where  $R = 35 \text{ k}\Omega$ ,  $d_{21} = 2.31 \times 10^{-12} \text{ CN}^{-1}$  for quartz,  $L_e = 3.5 \text{ mm}$ ,  $k = \frac{EWT^3}{4L^3} = 21000 \text{ Nm}^{-1}$  (using Youngs modulus for quartz,  $E = 7.87 \times 10^{10} \text{ Nm}^{-2}$ , forks width  $W = 0.6 \text{ mm}$ , thickness  $T = 0.32 \text{ mm}$  and length  $L = 4 \text{ mm}$ ). So one can write the above equation as,

$$F_{int}^{frictional}(d) = \left[ 1 - \frac{V(d)}{V(\infty)} \right] \frac{kx_0(\infty)}{\sqrt{3}Q(\infty)} \quad (2.8)$$

where  $V(d)$  and  $V(\infty)$  are the piezoelectric output voltage signals from the tuning fork at distance  $d$  and at a distance far away where frictional drag force does not exist. This shear force acting on the vibrating tip is used as a feedback to control the distance between a probe tip and pore membrane. From Eq. 2.8, we calculated the output voltage/displacement to be  $0.18 \text{ mV/nm}$ . An output voltage signal of amplitude  $0.366 \text{ V}$  (after 1000 times amplification) corresponds to an oscillation amplitude of  $2.8 \text{ nm}$ .

### 2.2.2 Nanopore Fabrication

Solid state nanopores used in this work were fabricated by using ion beam sculpting procedure introduced by Li et. al. [14]. Solid state nanopores are sculpted from a sub-micron hole in free standing Silicon nitride ( $\text{SiN}_x$ ) membrane with a high energy noble gas ion beam. The details of free standing  $\text{SiN}_x$  membrane preparation are discussed here [84]. Briefly, a  $380 \mu\text{m}$  thick silicon wafer with  $275 \text{ nm}$  low pressure chemical vapor deposition (LPCVD) of  $\text{SiN}_x$  (low tensile, silicon rich and amorphous) on both sides, was used to fabricate a free  $\text{SiN}_x$  membrane. Photoresist was coated on both sides of the wafer, a photo mask with features

of 579  $\mu\text{m}$  open window aligned on top layer of the wafer and exposed to UV radiation. Next, Reactive Ion Etch (RIE) technique was used to remove the  $\text{SiN}_x$  layer from the open window. Finally, the exposed Silicon (Si) layer was etched along the  $\langle 111 \rangle$  plane of Si by using 30% w/v KOH at  $90^\circ\text{C}$  to give a pyramid shaped hollow region with  $\approx 30 \mu\text{m}$  by  $30 \mu\text{m}$  free standing membrane  $\text{SiN}_x$  membrane of thickness 275 nm (is shown in Fig 2.4(a)-(d)(not to scale)). Once the membrane is ready, a high energy (50 keV) focused ion beam (FIB) was used to drill around a 100 nm hole in the free standing membrane prepared above. A transmission electron microscope (TEM) image of the FIB drilled hole (FIB pore) is shown in Fig. 2.4 (g). Then a single chip of size 3 mm x 3 mm having a FIB pore loaded into the Ion Beam Sculpting apparatus (IBSA). The complete description of the IBSA is discussed elsewhere [84]. In short, a 3 keV noble gas ion beam bombarded normally on the FIB drilled hole in the  $\text{SiN}_x$  membrane with a flux density of about  $1 \text{ ion}/\text{nm}^2\text{sec}$ . Electrostatic lens systems are used to focus the ions that pass through the FIB hole on the Channeltron style single ion detector. When ion beam strikes above the FIB hole surface, it brings out the lateral mass flow that eventually shrinks the top of the hole. As the hole size gets smaller, the number of ions passing through it also decreases. With the known initial area of FIB (measured with TEM) and assuming that the nanopore area is proportional to the number of the ions passing through the hole, beam was deflected away using LabVIEW controlled feedback system when the desired size of a nanopore is achieved. Finally, nanopores were annealed at  $800^\circ\text{C}$  for 1 hour in dry  $\text{N}_2$  in a tube furnace. To measure the final size after closing procedure, pores are imaged under TEM.

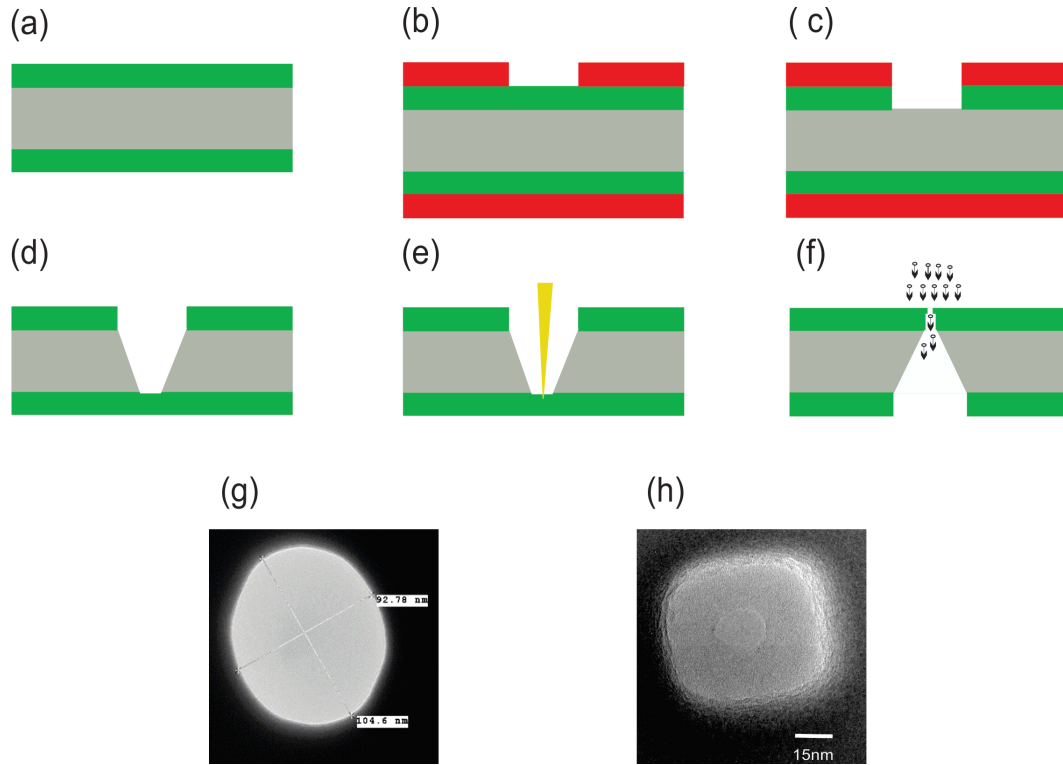


Figure 2.4: Schematics of the Ion Beam Sculpting nanopore fabrication procedure: (a) both sides of the  $380 \mu\text{m}$  thick silicon wafer are coated with  $275 \text{ nm}$  thin layer of LPCVD low tensile, silicon nitride. (b) Photo lithographically designed polymer etch mask covers the bottom surface completely and  $579 \mu\text{m}$  Silicon nitride region is open for etching. (c) RIE etch of the uncovered  $\text{SiN}_x$  region on top surface. (d) KOH wet etch of silicon, gives a  $30 \mu\text{m}$  free standing  $\text{SiN}_x$  membrane. (e)  $50 \text{ keV}$  highly focused  $\text{Ga}^+$  ion beam is used to create a  $100 \text{ nm}$  hole (FIB hole) (f)  $3 \text{ keV}$  energy, broad parallel beam of noble gas ions is bombarded on the free standing silicon nitride membrane with FIB hole, resulting in a motion of mass from the surface to the hole. Ions passing through the resulting hole are counted by a Channeltron, a single ion counter as a feedback system to control the size of the pore precisely. (g) A TEM image of the FIB hole of size  $104.40 \text{ nm} \times 92.78 \text{ nm}$ . (h) a TEM image of the  $17 \text{ nm}$  by  $21 \text{ nm}$  size nanopore made by the ion beam sculpting procedure.

### 2.2.3 Sample preparation

A complete description of the DNA sample preparation used for these experiments is explained in next chapter. Briefly,  $\lambda$  DNA's one end was ligated with biotin labeled DNA oligomer and unligated oligomers were removed from mixture by using the QIAEX II gel extraction kit.

### 2.2.4 Fluidic Chambers

Two fluidic chambers Cis and Trans were designed to hold a nanopore. PDMS solution was used to make fluidic chambers. Top view of both Cis and Trans fluidic chambers is shown in Fig.2.5(a) and (b) respectively. Cis chamber has a 1 mm opening at the center to bring the tip above the nanopore surface. Two channels were designed inside the cis chamber, as an inlet for the KCl solution and for a Ag/AgCl electrode. Another channel was made at 45°C on a side in cis chamber to have a view for preliminary alignment of the tip above the membrane. This channel was further sealed with a transparent cylindrical piece. Trans chamber is 2 cm x 2 cm x 1 mm and has a 1 mm hole at the center, two channels to flow the electrolyte in and out, and a third channel for a Ag/AgCl electrode to apply voltage across the chambers. As shown in Fig. 2.5(c), a transparent plastic cover slip was placed under trans chamber and was sealed with PDMS to prevent any solution leakage. A nanopore chip was inserted between cis and trans chambers and 1 M KCl solution with 10 mM TRIS and 1 mM EDTA at  $pH = 8$  is used as an electrolyte solution. To measure the ionic current across the nanopore channel, the Ag/AgCl electrodes in each chamber were connected to a current amplifier (Molecular device, Axon 200B). The whole system was enclosed in a

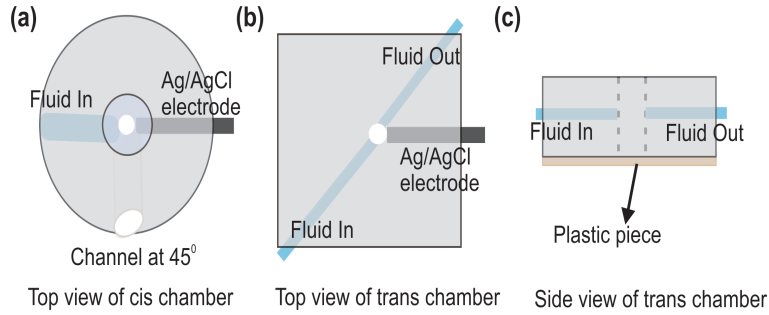


Figure 2.5: A schematic diagram of the top view of the fluidic chambers. (a) Top view of the cis chamber. Center of the cis chamber has a 3 mm on the top side, which is decreased to 1 mm at the bottom. Two channels in the opposite directions are for the fluid flow and Ag/AgCl electrode. Third channel on the side is at angle  $45^\circ$  was designed to have a primary alignment of the tip above the nanopore membrane. (b) Top view of the trans chamber shows two silicone tubes for fluid in and out and one channel for electrode. Trans chamber contains a 1 mm hole at the center for the bottom view of a nanopore for alignment purposes. (c) It shows the side view of a trans chamber, to prevent the solution leak a transparent plastic piece is glued at the bottom with PDMS.

home-made Faraday cage to reduce current noises due to electromagnetic radiation.

### 2.2.5 Nanopore - Tip alignment

As explained in the nanopore fabrication section, KOH etching step results in a pyramid-shaped pit with a  $30\ \mu\text{m} - 60\ \mu\text{m}$  free standing  $\text{SiN}_x$  membrane at the bottom on a  $3\ \text{mm} \times 3\ \text{mm}$  chip and is shown schematically in Fig. 2.4(e)(not to the scale). A low magnification TEM image of  $60\ \mu\text{m} \times 60\ \mu\text{m}$   $\text{SiN}_x$  membrane after pore fabrication is shown in Fig. 2.6(a). The bright spot at the center of image in Fig. 2.6(a) is a  $100\ \text{nm}$  size FIB hole. A high magnification TEM image, Fig. 2.6(b), displays a zoomed in view of FIB area containing  $17\ \text{nm} \times 17\ \text{nm}$  size nanopore. To align the probe tip above the nanopore, an objective lens and a CCD camera are aligned below the fluidic chambers as shown in Fig. 2.7. A long working distance ( $13\ \text{mm}$ ) objective lens (Mitutoyo, x50 Plan Apo Infinity-Corrected) is used to obtain an optical image of a nanopore through  $2\ \text{mm}$  thick trans chamber. Objective lens,

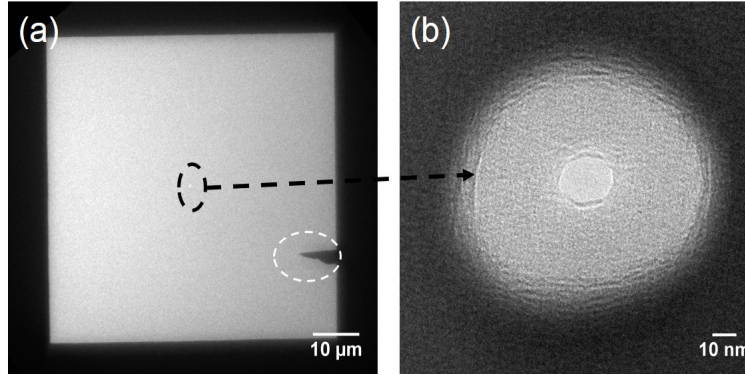


Figure 2.6: (a) A low magnification TEM image of  $60 \mu\text{m} \times 60 \mu\text{m}$   $275 \text{ nm}$  thick  $\text{SiN}_x$  membrane window. The bright point at the center shows a  $100 \text{ nm}$  FIB milled region, and black mark on the lower right side is a micron size dust particle. (b) A  $150 \text{ kX}$  magnification TEM image of shows a nanopore inside the FIB region. The black region is  $275 \text{ nm}$  thick silicon nitride membrane, gray part is a FIB-milled region, and the brightest area at the center is a nanopore of diameter  $17 \text{ nm}$ .

mirrors and CCD camera were aligned with a  $488 \text{ nm}$  laser. First, an optical image of the tip from CCD was obtained to find the  $x,y,z$  position on the micro-manipulator, then the tip was lifted up. All the steps, to bind streptavidin on a gold coated tip are explained in Chapter 3, and were performed on a glass slide. After this, the nanopore chip assembled between two fluidic chambers (Cis and Trans) was mounted on a micro-manipulator so that it can be moved in the XYZ directions. The membrane window was positioned at the center of screen by observing the optical image from the CCD. The DNA attachment steps were performed at about  $1 \text{ cm}$  away from the top hole of the cis chamber. After that, the DNA tethered tip is brought above the nanopore surface by viewing through  $45^\circ$  side channel present in the cis chamber. The optical image of  $\text{SiN}_x$  membrane from CCD does not show FIB region as in the low magnification TEM image Fig. 2.6(a), but a micrometer size dust, in dotted circle as shown in Fig. 2.6(a) can be spotted very easily and was used as the alignment marks when the tip was brought down. As  $16.5 \mu\text{m}$  long  $\lambda$  DNA molecule has a radius of gyration about

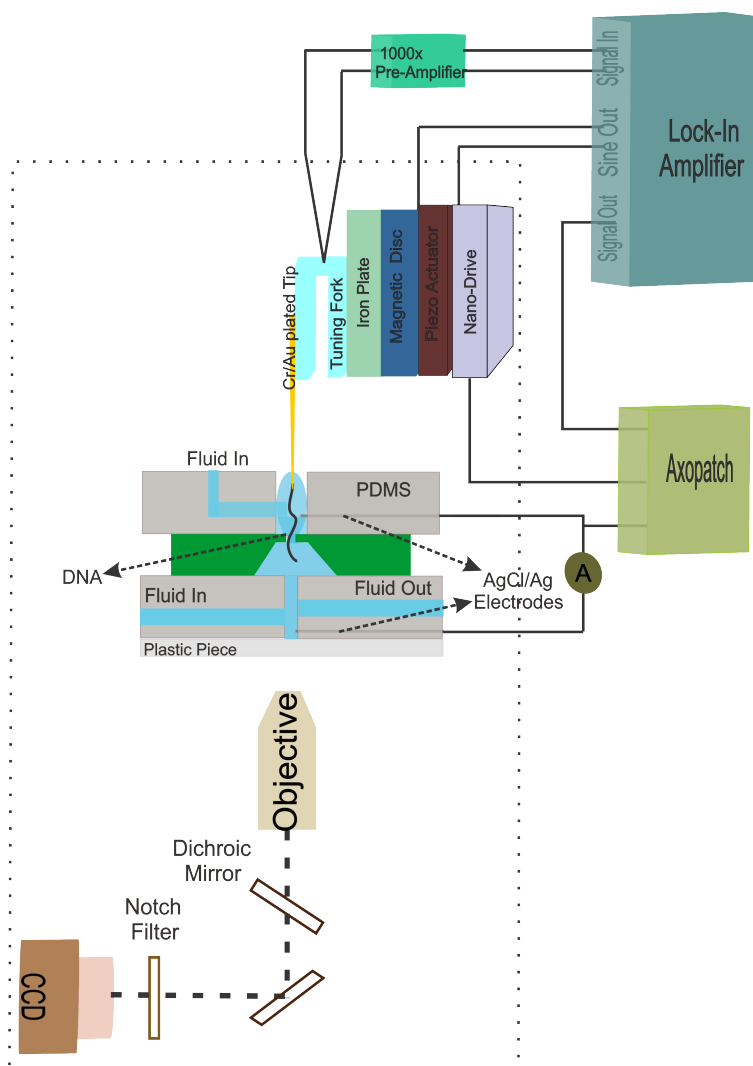


Figure 2.7: A drawing for the experimental setup of the SSN-TFFSP apparatus. A silicon chip with a nanopore is aligned between the fluidic chambers, and DNA-tethered tip is inside the cis chamber. The DNA-tethered tip is attached to a tuning fork sensor, which is connected to a piezo actuator, and a nano-positioner. The piezo actuator is excited by a Lock-in amplifier and a pre-amplifier (1000x) is used to amplify the output signal from the tuning fork. The output signal of the tuning fork after amplification is observed with the /lock-in amplifier. Objective lens and CCD camera are located under the fluidic chambers for the tip nanopore alignment.

0.5  $\mu\text{m}$ , once the tip is close to the nanopore, an electric field across the nanopore length will trap such a large molecule easily.

## 2.3 Results and Discussion

### 2.3.1 Control translocation of DNA through nanopore

SSN-TFFSP apparatus (Fig. 2.7) measures simultaneously three signals: the ionic current through the nanopore, the position of the DNA tethered probe tip and the vibrational signal of the tuning fork force sensor versus time. Figure 2.8(a) represents the ionic current measured through a 20 nm nanopore, at 60 mV with 1 M KCl salt solution the open pore current,  $I_o=15.95$  nA. Figure 2.8 (b) and (c) show the vertical position of the tip from nanopore surface and the vibration signal from the tuning fork force sensing probe respectively. Initially, tip is 34  $\mu\text{m}$  away from the nanopore surface with  $I_o=15.95$  nA and vibration signal from the tip is almost constant. As the tip approaches the nanopore surface, the vibrational signal from the tuning fork decreases. When tip is 1.4  $\mu\text{m}$  away (ii) the electric field across the nanopore captures DNA, first a drop of 34 pA in the nanopore current is observed. As the tip gets closer to the nanopore, current drop increases to 67 pA. The vibration signal from the tip is minimum near the surface because tip-surface interactions affect vibrational amplitude of the tip and is used as a feedback to stop the further movement of the tip towards the nanopore membrane. In Fig. 2.8, from (ii) to (iii) tip is not moving, the current drop is stable and the vibrational signal is minimum. When the tip is being lifted up ( At point (iii) of Fig. 2.8), the current drop of 67 pA remains constant up to 15.5  $\mu\text{m}$ . Further upward motion of the tip, reduces the current drop value to initial current drop step. At 17.8  $\mu\text{m}$ ,

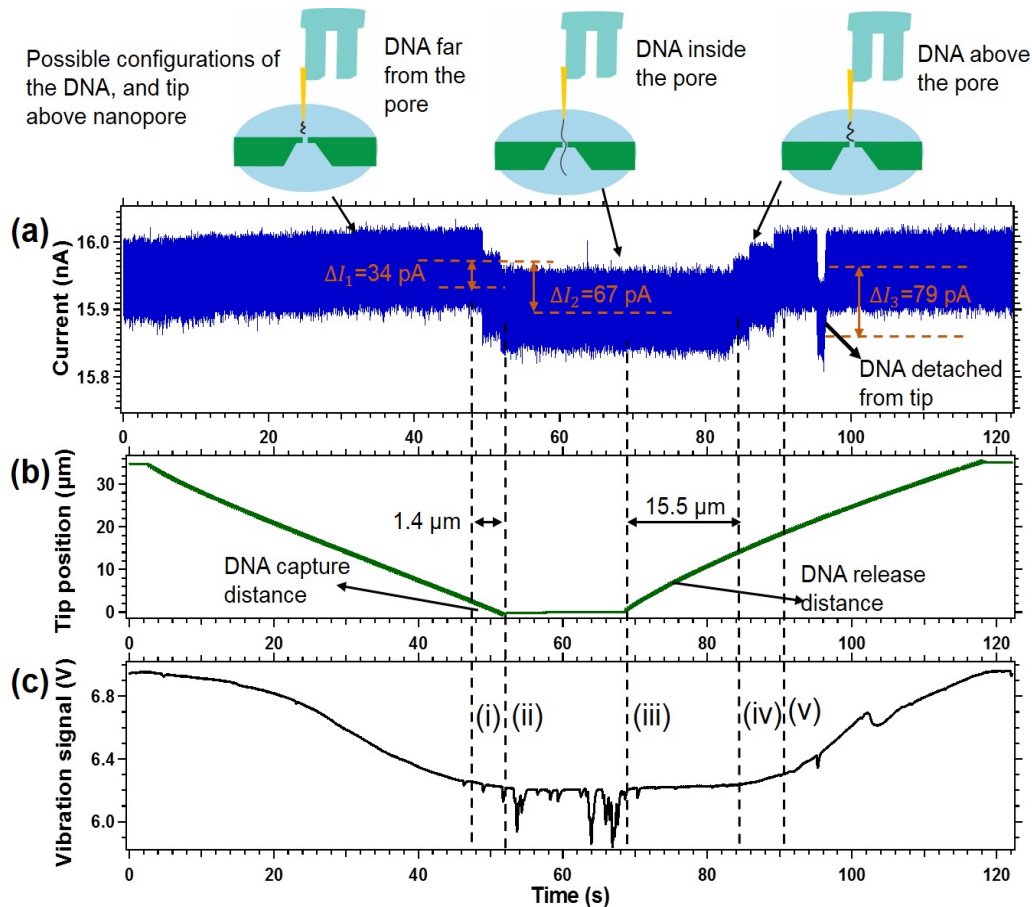


Figure 2.8: (a) Current measured from 20 nm at 60 mV with 1 M KCl, (b) Vertical position of the tip and (c) Vibration signal from the tuning fork versus time measured simultaneously by an Axopatch, when the tip is approaching down or is being lifted up from the nanopore surface. When the tip is close to the nanopore surface, the vibration signal from the tuning fork decreases, and DNA is trapped in the nanopore as a result current drops. Whenever DNA is captured (when tip is 1.4  $\mu\text{m}$  away while approaching the nanopore) or released (when tip is lifted up to 15.5  $\mu\text{m}$ ) from the nanopore, current drop steps are observed. Current reverts back to its original value when the DNA molecule is lifted away from the nanopore electric field range. Another current drop observed at 22.2  $\mu\text{m}$  while lifting up the tip is due to the passage of a DNA detached from the tip.

the current signal reverts back to its original value. In this experiment, we have also observed a current drop of 79 pA when tip is 22.2  $\mu\text{m}$  away from nanopore. It is interesting to note that the DNA capture distance (1.4  $\mu\text{m}$ ) outside the nanopore and the release distance (15.5  $\mu\text{m}$ ) of DNA are comparable to the radius of gyration and the contour length of  $\lambda$  DNA respectively. From the diffusion of DNA through nanochannel, radius of gyration of  $\lambda$  DNA is measured as  $\approx 0.5 \mu\text{m}$  [85] and contour length of  $\lambda$  DNA is 16.5  $\mu\text{m}$ . From one experiment, same trace was obtained 5-6 times with tip moving in and out. At voltage greater than 500 mV none of the translocations were observed, possibly due to rapture of streptavidin and biotin binding. Also when the tip is lifted fast from the nanopore surface DNA ruptures from the tip. Another example of an experimental data from a nanopore of size with 18 nm x 19 nm is shown in Fig. 2.9. At 60 mV  $I_o = 10.95 \text{ nA}$  is observed through the nanopore. In this experiment, first step of current drop was observed when tip was 4  $\mu\text{m}$  away from the nanopore. When the tip is lifted up to 12  $\mu\text{m}$  above with a step size of 400 nm, DNA is not released completely out of the nanopore. As a result current measured from the nanopore did not return to its initial value.

We argue that the current drop steps observed when DNA enters or exits the pore, are possibly due to presence of DNA above the nanopore. Such that DNA blocks the passage of some ions through nanopore. When DNA is completely inside the nanopore for about 15  $\mu\text{m}$ . It displaces large volume of ions fromt the nanopore, leading to a large current drop. The possible configurations of the tip, DNA and the nanopore corresponding to different current drop levels are shown in Fig. 2.8. To support this argument, we estimate the current drops when DNA is outside or inside the nanopore using finite element Comosol simulations. Figure 2.10 is obtained with the permission from the publisher [47].

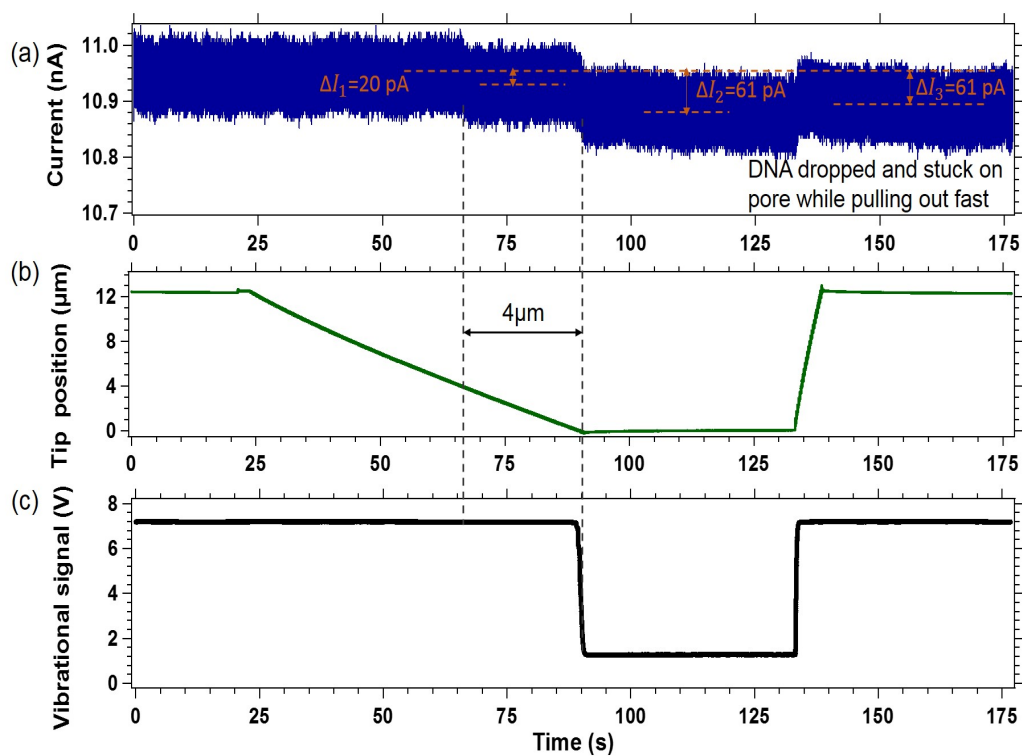


Figure 2.9: (a) Current measured from  $18 \text{ nm} \times 19 \text{ nm}$  at  $60 \text{ mV}$  with  $1 \text{ M KCl}$ , (b) Vertical position of the tip and (c) Vibration signal from tuning fork measured simultaneously with an Axopatch. In this case, DNA capture distance is  $4 \mu\text{m}$  and tip is being lifted up with a step size of  $400 \text{ nm}$  to  $12 \mu\text{m}$ . Current has not recovered its initial value.

### 2.3.2 Comsol Simulation

Nernst-Planck and Poisson equations were used to simulate the current at different distances when DNA is approaching the nanopore. Nernst-Planck equation describes the flux of the charged ions in a fluid under the effect of concentration gradient and electric field and is given by,

$$J_i = -D_i \nabla c_i - \frac{Z_i F}{RT} D_i c_i \nabla \phi + c_i u \quad (2.9)$$

where  $J_i$ ,  $D_i$ ,  $c_i$  and  $Z_i$  are current flux, diffusion coefficient, concentration and charge on the  $i^{th}$  ion respectively.  $F$  is the Faraday constant,  $R$  is the gas constant,  $T$  is the absolute temperature,  $\phi$  is the local electric potential and  $u$  is the fluid velocity (which is zero in our case). The electric field and electric potential generated by the ions is given by the Poisson equation,

$$\nabla^2 \phi = -\frac{F}{\varepsilon} \sum Z_i c_i \quad (2.10)$$

where  $\varepsilon$  is the dielectric constant of the fluid. These equations are solved with user defined nanopore geometry and DNA at different positions, for current flux of  $K^+$  and  $Cl^-$  ions. The current passing through the nanopore is obtained by integrating current flux of both  $J_{K^+}$  and  $J_{Cl^-}$  ions over the nanopore area for both situations with and without DNA.

$$I = \int (J_{K^+} + J_{Cl^-}) dA \quad (2.11)$$

A 25 nm size pore with a geometry as shown in Fig. 1.1(c) and a double strand DNA (dsDNA) molecule as an insulated solid rod with diameter 2.2 nm were used for simulations.

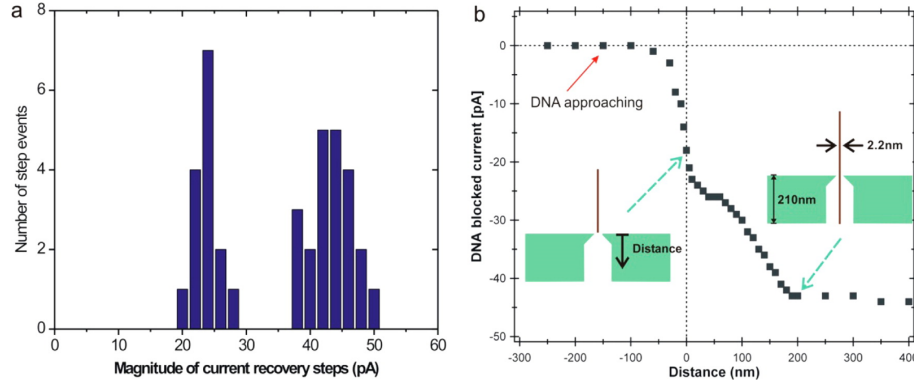


Figure 2.10: (a) Histogram of the current steps while pulling out the DNA from nanopore from different experiments. (b) Current drop values versus the distance of the DNA from the nanopore simulated from the finite element simulations. A nanopore of 26 nm diameter is used and the simulations gives an open pore current value,  $I_o = 14.6$  nA through nanopore. The dsDNA is considered as an insulated cylindrical rod with a diameter of 2.2 nm. Inset figures show the DNA above and inside the nanopore. The current drops correspond to each configuration is pointed out with the arrows [47]. This figure is “Reprinted with permission from (C. Hyun, H. Kaur, R. Rollings, M. Xiao, and J. Li, *Acs Nano* 7, 5892 (2013)). Copyright(2013), American Chemical Society”.

Figure 2.10(b) represents simulated current drops with DNA at different distances from the nanopore membrane. Figure. 2.10(a) shows the histogram of current blockage observed experimentally from various experiments. Two kind of current drop steps at  $\approx 25$  pA and at  $\approx 45$  pA are observed more frequently. Simulations in Fig. 2.10(b) show that current drops occurs when DNA is 50 nm above the nanopore. At nanopore surface the drop is 20 pA and as DNA has traveled to other the end of the FIB region of the nanopore( $\approx 200$  nm), the current drop has a maximum value of 45 pA. The possible configurations for both the situations are shown in teh insets of Fig. 2.10(b). The right peak of recovery steps, Fig. 2.10(a), is justified with the values obtained from simulation. The peak at lower current could be due to DNA sticky events. Another point to note here is that the simulations only assume the volume exclusion of ions in the nanopore is the sole criteria for current blockage. There could be other factors like binding of cations to DNA inside the nanopore [86] and charge on the

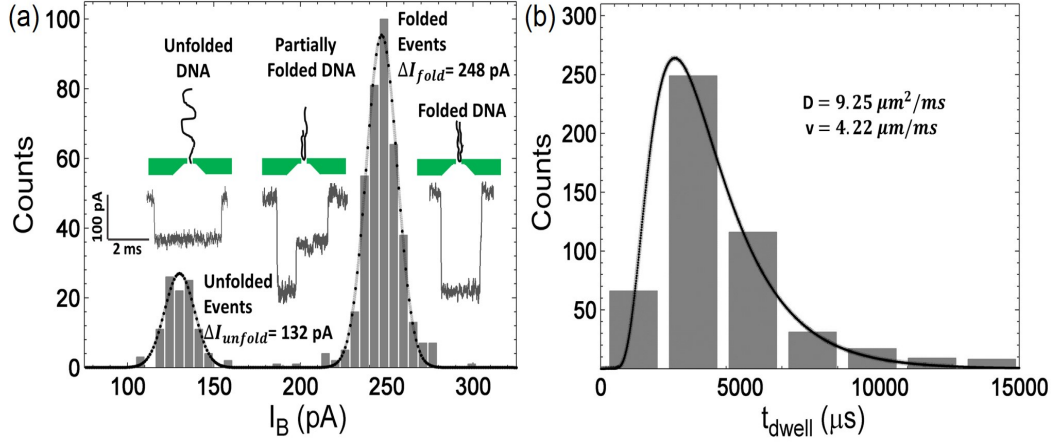


Figure 2.11: (a) Current histogram of  $\lambda$  DNA free translocation events through a nanopore of size 18 nm x 19 nm at 120 mV.  $I_o$  measured with 1M KCl is 11 nA. It shows two peaks that correspond to the unfolded and folded  $\lambda$  DNA events and are fitted with Gaussian distribution (dotted line). The possible configurations for different kinds of events are shown in the inset. (b) Dwell time histogram of the  $\lambda$  DNA at 120 mV. Time distribution has a peak at 2.5 ms. Solid line is a PDF(Eq. 4.3) fit with fitting parameters:  $D= 9.25 \mu\text{m}^2/\text{ms}$ , and  $v= 4.2 \mu\text{m}/\text{ms}$ .

nanopore surface [87] that can contribute to current blockage. However, the results obtained from these simple simulations support the current drop observed during the DNA entrance and recovery steps observed while DNA is exiting the nanopore.

### 2.3.3 Comparison with free translocation of $\lambda$ DNA

At 60 mV current drop due to the DNA is 67 pA and total time for translocation from (ii) to (v) in Fig. 2.8 is  $\approx 44$  s. To compare it with the native translocation experiments, we performed free translocation experiment of  $\lambda$  DNA molecules through a 19 nm size pore. The translocation experiments were performed at 120 mV with 1 M KCl, 10 mM Tris and 1 mM EDTA solution. Different kinds of translocation events: such as unfolded (DNA enters at its end), partially folded (DNA is captured little away from its end) and completely folded (DNA is captured at its center) were observed. Fig. 2.11(a) represents the histogram of

blockage current with two Gaussian peaks centered at 132 pA (unfolded events) and 250 pA (folded configuration). An example of each kind of event is shown in the inset of Fig. 2.11(a) with possible configurations of DNA entrance to the nanopore. According to Eq. 1.2, at 60 mV the current blockage due to unfolded DNA molecule is 61 pA. This current drop matches well with observed current drop when DNA is inside the nanopore from the SSN-TFFSP system. The dwell time,  $t_{dwell}$ , histogram for free  $\lambda$  DNA translocation is shown in Fig. 2.11(b). We used the probability density function from one dimensional diffusion model proposed by Li [88, 89](explained in chapter 4) to fit the dwell time histogram. From this fit, we obtained  $D = 9.25 \mu\text{m}^2/\text{ms}$  and  $v = 4.2 \mu\text{m}/\text{ms}$ . At 120 mV, the time distribution has a peak at 2.5 ms. According to Eq. 1.3, one would expect the translocation time to be  $\approx 5$  ms at 60 mV. This implies that 100 base pairs are translocating in  $1 \mu\text{s}$  through the nanopore. This is much lower than the temporal resolution of an Axopatch. On the other hand, the SSN-TFFSP has increased the dwell time to 31 s or less, and hence a translocation speed of  $> 100 \mu\text{s}$  per base pair. This translocation speed is  $\approx 1000$  times slower than free translocation speed obtained from the native nanopore experimental set up.

## 2.4 Conclusion

In this chapter, I have discussed the SSN-TFFSP capacity to control the trans location speed of DNA tethered to a probe tip through a voltage biased nanopore. The position of the tip above the nanopore, is sensed and controlled by the tuning fork force sensor and a nanoposition system. DNA tethered probe tip can be brought down and pulled out from the nanopore at a sub nanometer precision. The process of DNA capture and release from the nanopore can be used to explain the DNA-nanopore interactions. DNA capture and release

distances are equivalent to the radius of gyration and contour length of  $\lambda$  DNA (48502 bps). A translocation speed  $> 100 \mu s$  per base pair is achieved, and which is 1000 times slower than the tethered free translocation of DNA. The SSN-TTFSP system has enough temporal resolution to sequence the DNA molecule. This apparatus of high temporal resolution has a potential to study small features like hybridization sites on DNA, DNA- protein and RNA-protein interactions.

## Chapter 3

### Characterization of DNA tethered fiber tip

#### 3.1 Introduction

To slow down DNA translocation speed through the nanopore using a probe tip, the first challenge was to attach the DNA on the probe tip end. Further then, characterize the binding strength between DNA and the tip, and estimate the number of DNA molecules attached to the tip. In the literature, several methods are available to stretch DNA, for example: when liquid is flowing across and DNA is immobilized on a channel surface, It will stretch DNA due to dynamic shear force [90], optical tweezers [91] and magnetic tweezers [92]. Electric fields have also been used to study the electro kinetic stretching of DNA molecules between two electrodes [93–95]. We designed a DNA stretching experiment by using dielectrophoresis (DEP) force to study the DNA binding strength to tip. In an alternating electric field, permanent charged particle oscillates around a stable position [96, 97]. On the other hand, a dielectric particle in a non-uniform ac electric field gets polarized, this induced dipole interacts with the external electric field and experiences a force. A non uniform field creates unbalanced forces on the dielectric particle as a result, it has a net motion. DEP is different from the electrophoresis where a net charged particle will move due to Coulombic force experienced in an external uniform electric field. If a dielectric particle is more polarizable than the surrounding medium, dipole aligns with the external field and experiences a net force towards the regions of highest electric field strength. This phenomenon is known as positive DEP. If the particle is less polarizable than the medium, the dipole aligns in a direction opposite to the external field. It is repelled from the region of high field strength,

which is known as negative DEP [98]. The dielectrophoretic force,  $F_{DEP}$  acting on a spherical object is given by [97],

$$F_{DEP} = 2\pi r^3 \epsilon_m \text{Re}[K(\omega)] \Delta E^2 \quad (3.1)$$

where  $r$  is radius of the object,  $\epsilon_m$  is the permittivity of the medium,  $E$  is the rms electric field and  $\text{Re}[K(\omega)]$  is real part of the Clausius-Mossotti factor and is given by [97],

$$K(\omega) = \frac{(\epsilon_p^* - \epsilon_m^*)}{(\epsilon_p^* + 2\epsilon_m^*)} \quad (3.2)$$

where  $\epsilon_p^*$  and  $\epsilon_m^*$  are the relative complex permittivities of the particle and medium respectively.  $\epsilon^* = \epsilon - i\frac{\sigma}{\omega}$ , with permittivity,  $\epsilon$ , the conductivity of the medium  $\sigma$ , and angular frequency of the applied electric field,  $\omega$ . The sign of  $\text{Re}[K(\omega)]$ , decides if the molecules will be attracted or repelled from a strongest electric field gradient region. DEP force depends upon the frequency of applied ac electric field, electric field gradient between the electrodes and is independent of the direction of the applied field. DNA is a negatively charged biomolecule due to presence of the unit electron charge on the phosphate group of DNA backbone. In an electrolyte solution, charged polymer like DNA at pH = 7 attracts free positive ions (known as counter ions cloud) around it, hence polymer is neutral in the absence of an external electric field shown in Fig 3.1(a). When an electric field is applied, ions present in the fluid move to shear away the counter ions at Zeta potential surface, as a result, a net charge density is developed along the length of the polymer as shown in Fig 3.1(b). This polarized charged distribution of counter ions cloud along the DNA gives a net dipole moment. Dielectric constant (relative permittivity,  $(\epsilon_r^*)$ ) is a function of the

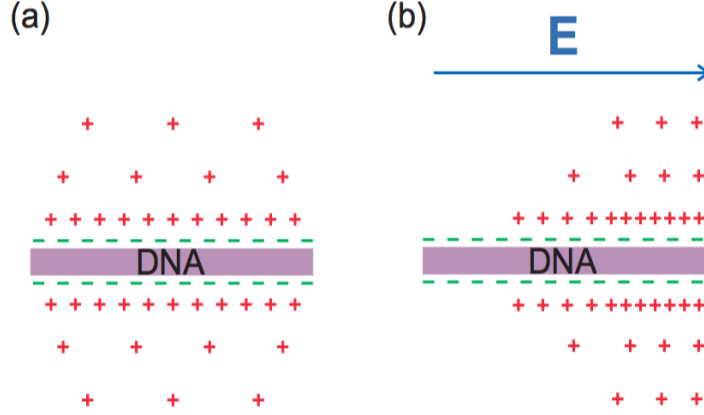


Figure 3.1: (a) Schematic of a negatively charged DNA molecule surrounded by counter ions (cations in solution). This counter ion cloud create an electrostatic screen to neutralize the charge on the DNA molecule. (b) Effect of the electric field on the charge distribution of the counter ions along the length of a DNA molecule.

frequency of the applied field. At low frequency, dielectric constant of a DNA molecule is greater than water, but for  $\approx 100$  kHz frequency  $\epsilon_{DNA}^* \leq \epsilon_{water}^*$  [99]. It is found that at low frequency ( $< 2$  kHz), DNA exhibits positive dielectrophoretic behavior [100] and experiences a negative DEP for frequency 1 MHz in a non-uniform ac electric field [93, 101]. In our experiment, DNA molecules are attached to gold coated tip, dielectrophoresis is driven by applying alternating electric across two electrodes (a gold coated tip placed above a bottom electrode) as shown in Fig. 3.1. The experimental set up of DNA binding and stretching is explained in the next section.

## 3.2 Experimental setup and Methods

### 3.2.1 Tip Fabrication

We fabricated the tip from a single mode optical fiber (Corning, SMF-28(TM)) by using a micropipette puller (Sutter Instrument, P-2000). Optical fiber is made up of quartz material,

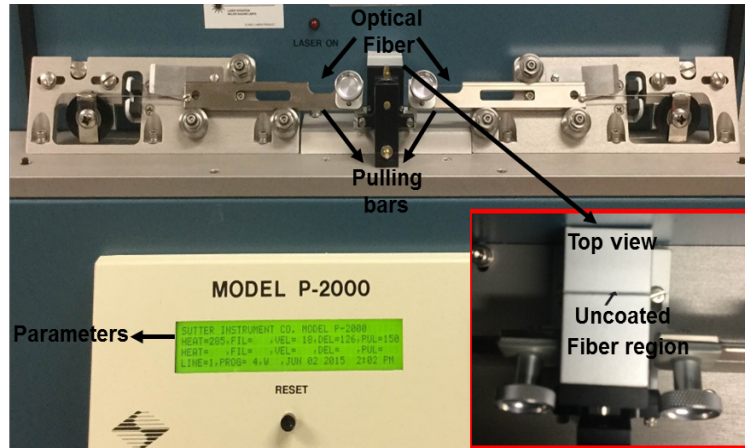


Figure 3.2: Picture of the P-2000 micropipette puller with an optical fiber aligned in the puller bars. Inset shows top view of the instrument, where uncoated part of the fiber is exposed to the laser for heating.

with the clad diameter  $125 \mu\text{m}$  and is coated with a plastic sheath for protection. The final diameter of the fiber after coating is  $245 \mu\text{m}$ . From the center of a 15 cm long piece of optical fiber, a 2 cm long plastic coating is stripped off. Then this fiber is aligned in the pulling bar (Fig. 3.2) of the tip puller such that an uncoated quartz part rests inside the heating area as shown in the inset of Fig. 3.2. This puller first melts the quartz optical fiber core with a  $\text{CO}_2$  laser as a source of heat, then it pulls the fiber. Before pulling, the melted fiber region gets elongated due to the motion of the pulling bar where the tip is aligned. Finally, the hard pull gets activated to pull the bars and produce two tips on both sides. The typical parameters for pulling the optical fiber were set as: Heat = 285 ( $\approx 2$  Watts, specifies the output power of the laser), Velocity = 18 ( $\approx 0.45$  mm/sec is velocity at which puller bar is moved before hard pull), Delay = 126 (This parameter controls timing of the start of hard pull and deactivation of laser. For the delay value less than 128 ms hard pull is activated and heat turns off after 128 ms) and Pull = 150 ( $\approx 9$  N force of the hard pull). The pulled fiber tips were first cleaned in Piranha solution (sulfuric acid: hydrogen peroxide=

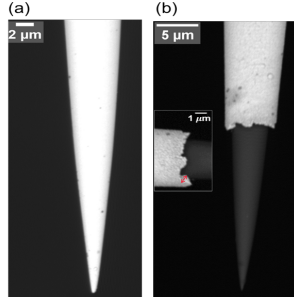


Figure 3.3: (a) A SEM image of the Cr/Au coated optical fiber tip fabricated from the micropipette puller (b) SEM image of the fiber tip without Cr/Au coating at the end. Inset shows the high resolution SEM image of coated/uncoated region of the tip. A red arrowhead line shows the thickness of the Au/Cr coating to be  $\approx 300$  nm.

3 : 1) for 10 minutes, and after that these tips were soaked in DI water for 30 minutes. After the cleaning steps, tips were dried for an hour. Once tips were dried, first a sacrificial layer of chromium was coated for 20 seconds in 0.07 mbar with 20 mA current by using a Cressington, Auto 108 sputter coater. On the top of Chromium coating, a thick layer of gold metal was deposited for 9 minutes under similar conditions of pressure and current. A scanning electron microscope (SEM) image of a Cr/Au coated tip made from puller is shown in Fig. 3.3(a). The thickness of the gold coating is about 300 nm and was measured from the SEM image of the tip (Fig. 3.3(b)), whose end part was not coated with gold.

### 3.2.2 Bottom Electrode

The bottom electrode is made from a 1 mm diameter brass rod. A 2 mm by 2 mm piece of the cover glass was glued to one end of the brass rod with silver epoxy. Then it was coated with Cr and Au under the same conditions as used for coating the tips (explained in the previous section). An image of the bottom electrode is shown in Fig. 3.4(a).

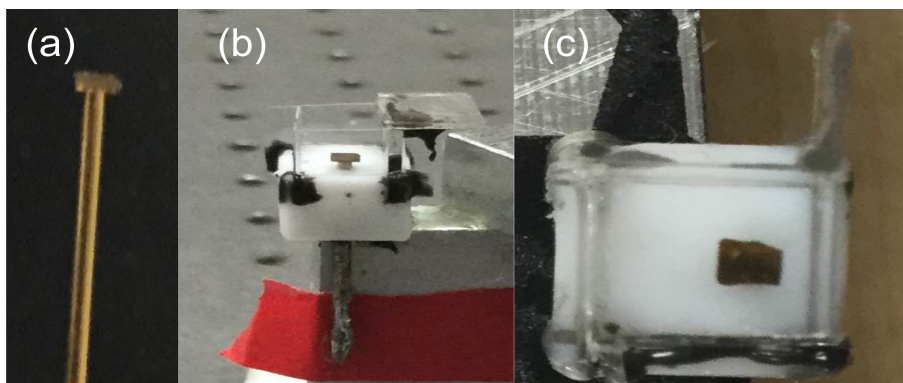


Figure 3.4: (a) An image of the gold-coated bottom electrode. (b) An image of the glass aquarium build on the Teflon support. Cover glass pieces are glued inside the slots drilled on Teflon support, and are finally sealed with PDMS. Bottom electrode is placed inside the hole drilled through the Teflon base. (c) Top view of the bottom electrode and glass chamber on the Teflon support.

### 3.2.3 Chamber

To hold the cover glass pieces, the 2 mm deep, and 1 mm wide slots were drilled on all sides of a 1.5 cm<sup>3</sup> Teflon support. The Teflon support was further drilled through to have a 1 mm hole for the bottom electrode as shown in Fig. 3.4(b). The glass pieces were glued in Teflon slots with an epoxy and were finally sealed with Polydimethylsioxane (PDMS)(Fig. 3.4(b)). This glass aquarium above the Teflon support has a capacity of roughly 1 cm<sup>3</sup>, and accommodates the tip and bottom electrode in an electrolyte solution for DNA stretching. Figure 3.4(c) shows the top view of the glass aquarium and bottom electrode.

### 3.2.4 Streptavidin-Biotin binding Chemistry

Streptavidin, a 58 kDa protein, has a high affinity to bind biotin (Vitamin-B7)[102]. The interaction between streptavidin and biotin is one of the strongest non-covalent bindings known in nature [102]. In a folded state, a streptavidin monomer has antiparallel  $\beta$  barrel structure and one binding site for biotin is located at the end of each  $\beta$  barrel [103] as shown

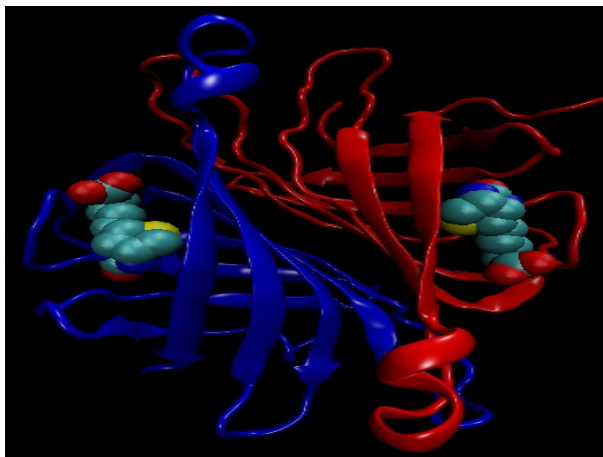


Figure 3.5: A 3D representation of Streptavidin-biotin complex dimer (3RY2.pdb) [103]. Streptavidin dimer consists of blue and red barrels. Each binding pocket (one per barrel) holds a biotin molecule at the end.

in Fig. 3.5. Few the amino acid residues inside the barrel and an additional amino acid (TRP 120) of neighboring monomer contribute to the biotin binding pocket. Streptavidin's extraordinary affinity to biotin has been attributed to many factors including: (1) Structural compatibility between biotin and the binding pocket in streptavidin [104](2) the huge hydrogen bond network between biotin and the amino acids residue of binding pocket [105] (3) the hydrophobicity of the binding pocket [105]. The schematic of a streptavidin dimer holding two biotin molecules in the binding pocket is drawn (Fig. 3.5) with Visual Molecular Dynamics by using 3RY2.pdb [103]. In our experiment, we make use of the strong streptavidin biotin binding chemistry to attach the DNA molecules to the gold plated tip. We attached streptavidin on the gold coated tip and modified  $\lambda$  DNA molecules with a biotin on it's one end. The preparation of DNA molecules is explained in next section.



is then incubated at 65°C for 20 minutes. The mixture was left to cool down slowly for a few hours to allow the hybridization of the biotin oligomer to the  $\lambda$  DNA end. The ligation reaction was performed with the T4 DNA ligase enzyme. 4  $\mu$ l of T4 DNA ligase enzyme was mixed in the prepared reaction mixture, and was incubated at 12°C overnight.

### **Removing unligated Biotin oligomers**

The unbound oligomers were separated from the mixture with a QIAEX II gel extraction kit. We skipped the first step of gel electrophoresis from the protocol and followed the rest of the protocol to remove the unligated oligomers. The 150  $\mu$ l solution was divided into three tubes. The 50  $\mu$ l solution in each tube was filtered with DNA gel-extraction kit. After the purification steps, the concentration of purified biotinlated  $\lambda$  DNA was measured by spectrophotometer. Purified biotin labeled  $\lambda$  DNA (2 – 3 nM) is about 8 times more diluted than original  $\lambda$  DNA. Finally, biotinlated  $\lambda$  DNA was stained with Ethidium bromide (EtBr) (Sigma Aldrich, E1510 – 10 ML) dye. First, the EtBr is diluted 100 times to get a final concentration of 250  $\mu$ M, then 8  $\mu$ l of this is added to 50  $\mu$ l of the purified biotinlated  $\lambda$  DNA. The final solution of DNA will have 1200 EtBr molecules per  $\lambda$  DNA.

### **3.2.6 Fluorescent imaging**

Etbr has two strong absorption peaks in UV region and one weak absorption peak around 480 nm, and It emits a light of wavelength 608 nm. A 488 nm wavelength laser was used to excite EtBr stained  $\lambda$  DNA. To get an optimal fluorescent image, power of the laser (Coherent, HighLight laser) was adjusted from 1 mW to 10 mW. A 100x Mitutoyo objective lens with a long working distance (6 mm) was used to capture the fluorescent image of DNA

. To minimize background light during capture, a notch filter (Kaiser, HNPF-488 – 1.0) for the 488 nm laser and an optical band pass filter (Edmundoptics, 550 nm CWL, 80 nm Bandwidth, NT65 – 744) were placed between the object lens and a cooled CCD (Sony ICX285AL Monochrome Sensor). To reduce background light further, a piece of aluminum tube was machined to place the objective lens, notch filter, optical band pass filter, and CCD camera together. ImageJ software was used to enhance the contrast of the captured fluorescent images.

### **3.2.7 DNA stretching setup**

The schematic of the DNA stretching setup is shown in Fig. 3.7. In order to control the position and alignment of the electrodes within few a microns, the tip electrode and glass chamber containing the bottom electrode were mounted on two manual XYZ micromanipulators. DNA was tethered to the tip via streptavidin-biotin binding. An optic fiber tip was coated with gold to serve two purposes: (1) to make it conductive (2) Streptavidin sticks well to the gold surface. A 10 – 20  $\mu\text{m}$  long end of the tip was held in a 10 mg/ml streptavidin (Invitrogen, 434301) solution for 10 minutes. The tip was then washed several times with DI water to get rid of weakly absorbed streptavidin. This streptavidin coated tip was dipped into the biotin-labeled  $\lambda$  DNA solution for 10 minutes. All the streptavidin and DNA attachment steps were performed on the glass piece outside the glass chamber, which is shown in Fig. 3.4(b). After soaking the tip in  $\lambda$  DNA solution, the tip was washed several times with diluted TAE buffer with a conductivity of 0.2 S/m. Hereafter, the tip's end with DNA was kept in solution all the time to avoid DNA detachment. The tip was then moved by a micromanipulator into the glass chamber containing the diluted TAE buffer.

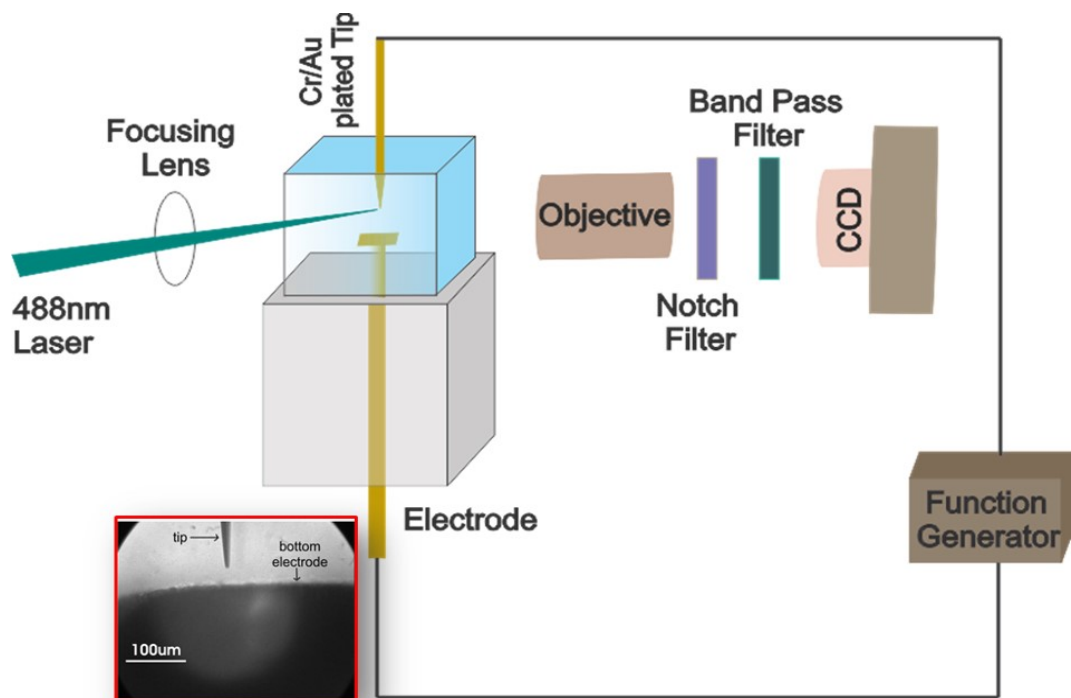


Figure 3.7: A schematic diagram of the DNA stretching setup. The gold coated tip and bottom electrode are housed inside a glass aquarium. A 488 nm laser is focused on the tip to excite the EtBr stained  $\lambda$  DNA. Optics for the fluorescence imaging: Object lens, notch filter, optical band pass filter, and CCD camera are aligned and placed inside a piece of machined cylinder. Inset shows an image of the tip aligned above the bottom electrode.

Both the electrodes were aligned on each other as shown in inset of Fig. 3.7. A function generator (Agilent Technologies, 33250A) and power amplifier (HP, 467A Instrumentation Power Amplifier) were used to apply an AC voltage signal between the two electrodes. The AC output voltage obtained from this power amplifier can be as high as 60 V<sub>pp</sub> with a maximum frequency of 2 MHz.

### **3.3 Results and discussion**

#### **3.3.1 Streptavidin Binding to tip**

To ensure the nonspecific binding of Streptavidin to the gold plated tip, a control experiment was performed by using the streptavidin, which is conjugated with FITC dye (Invitrogen). FITC dye has an excitation peak around 495 nm. To attach the streptavidin FITC conjugate on the gold coated tip end, the same steps were repeated as explained in the previous section. A fluorescent image was taken after washing with DI water, as shown in Fig. 3.8. The fluorescent image confirms that streptavidin is absorbed on the tip surface.

#### **3.3.2 Voltage and frequency dependence of DEP stretching**

The fluorescent image of the Etbr stained  $\lambda$  DNA, attached to the gold tip, which is at 20  $\mu$ m away from the bottom electrode, is shown in Fig. 3.9. The bright spots on bottom electrode are due to loose DNA diffusing in electrolyte solution and eventually has settled on the bottom electrode. An AC voltage signal was applied from 10 V<sub>pp</sub> to 50 V<sub>pp</sub> at 1 MHz frequency. Figure 3.9(a) shows that the DNA has not stretched for voltage up to 30 V<sub>pp</sub>. The electric field is not strong enough to stretch the DNA from its coiled state. For

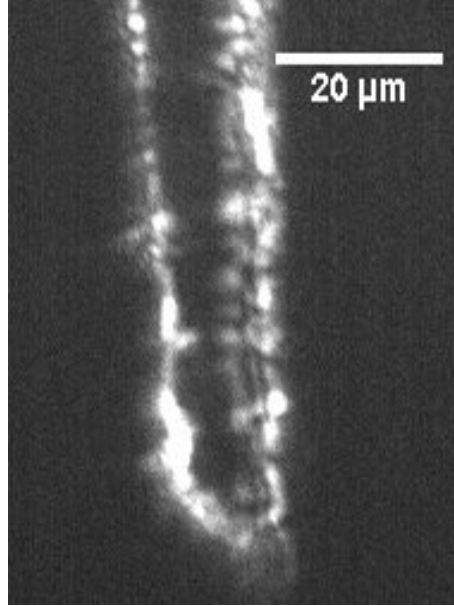


Figure 3.8: A fluorescent image of the streptavidin absorbed tip. End of the tip was broken intentionally.

a  $20\ \mu\text{m}$  gap between the electrodes, maximum stretching of DNA was observed at  $36\ \text{V}_{\text{pp}}$  (Fig. 3.9(b)). As suggested by Eq. 3.1, an increase in electric field gradient results in an increase in the DEP force to unfold the DNA from its native state. Apart from the applied voltage amplitude, the effect of the frequency on the stretching was also studied, as DEP force depends upon the frequency of applied AC signal. The frequency of applied AC voltage signal was varied from  $1\ \text{MHz}$  to  $50\ \text{kHz}$ . The best stretching signal was observed at  $1\ \text{MHz}$ . In a low frequency regime ( $< 100\ \text{kHz}$ ), air bubble formation near the bottom electrode has been observed. The bubble generation problem also arises, when a high voltage was applied across the electrodes for a long time. The air bubble formation at high voltage can be attributed to the Joule Heating effect. When an electric voltage ( $V$ ) is applied across a resistor ( $R$ ), the power dissipation of the resistance medium is  $V^2/R$ . As a result, temperature of the electrolyte increases near the electrode due to this power dissipation. The temperature

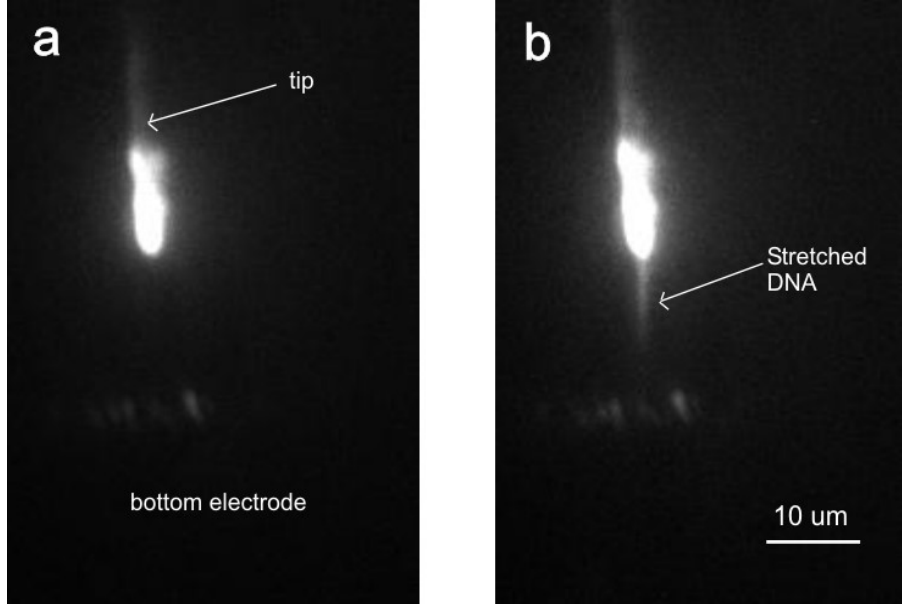


Figure 3.9: (a) A fluorescent image of the DNA attached to the tip in 2x diluted TAE buffer, when a  $30 V_{pp}$  at 1 MHz signal is applied across the electrodes. (b) A fluorescent image of the stretched DNA at a applied voltage of  $37 V_{pp}$ . This figure is reused with permission from the publisher.<sup>1</sup>

difference ( $\Delta T$ ) due to the Joule heating can be estimated as  $\Delta T \approx \sigma V_{rms}^2/k$ , where  $\sigma$  is the electric conductivity of the electrolyte,  $V_{rms}$  is the root mean square of applied signal, and  $k$  is the thermal conductivity of the electrolyte. From our experimental parameters  $\sigma = 0.2 \text{ S/m}$ ,  $V_{rms} = 14.1 \text{ V}$ , and  $k_{water} = 0.6 \text{ Jm}^{-1}\text{s}^{-1}\text{K}^{-1}$ , the temperature difference can be estimated as  $\Delta T = 66^\circ\text{C}$ . The small gap of  $\approx 15 \mu\text{m}$  between the two electrodes limits temperature change measurement in our setup.

### 3.3.3 Dependence of stretching Voltage on the distance between electrodes

Next, the effect of the distance between both electrodes on the applied AC voltage was studied to obtain the maximum stretching of  $\lambda$  DNA. It was observed that as the gap

<sup>1</sup>C. Hyun, H. Kaur, D. S. McNabb, and J. Li, Nanotechnology 26, 125501 (2015) doi:10.1088/0957-4484/26/12/125501 “© IOP Publishing. Reproduced with permission. All Rights reserved” [107].

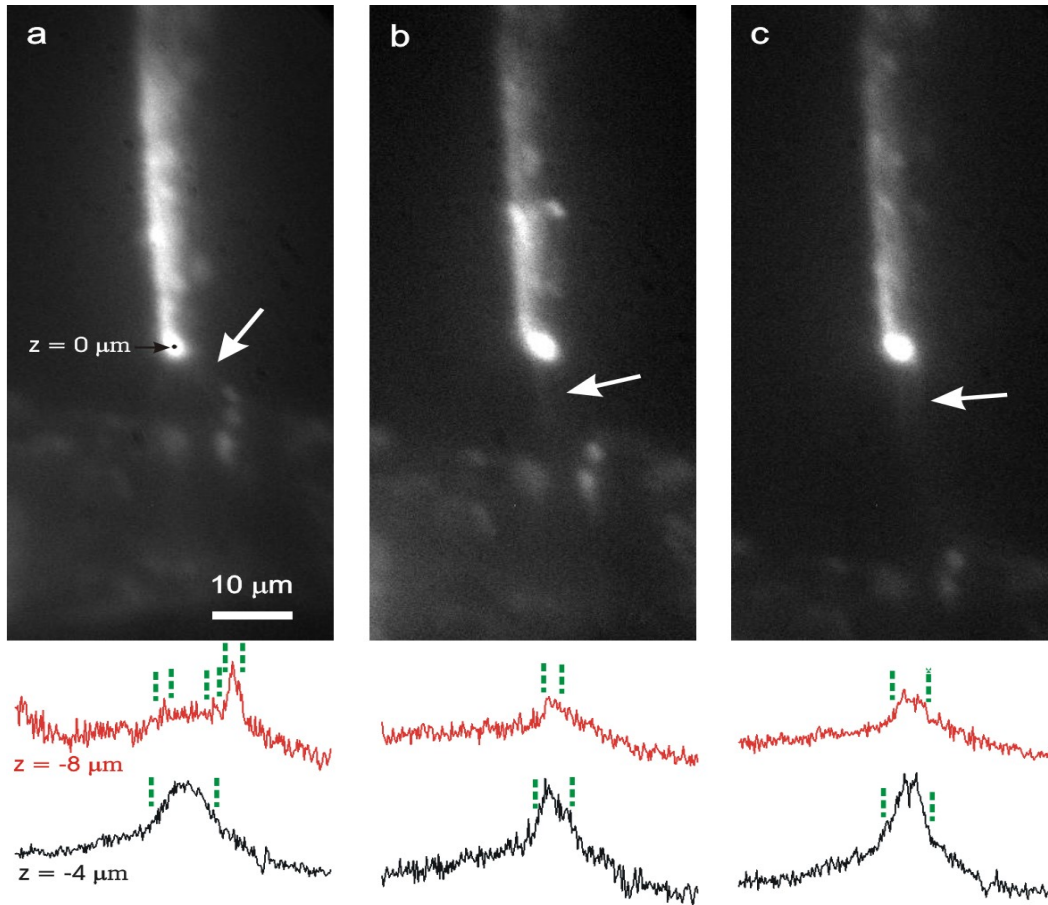


Figure 3.10: Fluorescent images of the stretched  $\lambda$  DNA between the tip and bottom electrode for the gap distances: (a)  $9\ \mu\text{m}$  (b)  $15\ \mu\text{m}$ , and (c)  $30\ \mu\text{m}$  in 2X diluted TAE buffer. The cross-sectional plots of fluorescence intensity at  $z = -4\ \mu\text{m}$  and  $-8\ \mu\text{m}$ . White arrows indicate the stretched DNA. The applied AC voltage is (a)  $23.4\ V_{pp}$ , (b)  $33.3\ V_{pp}$  and (c)  $41.1\ V_{pp}$  for the gap distances of  $9\ \mu\text{m}$ ,  $15\ \mu\text{m}$ , and  $30\ \mu\text{m}$ , respectively. This figure is reprinted with permission from the publisher<sup>2</sup>

between the tip and bottom electrode increases, to stretch DNA applied voltage strength also increases. Figure. 3.10 shows fluorescent images of stretched DNA molecules for various gap distances between the tip and bottom electrode. At about  $9\ \mu\text{m}$  above the bottom electrode,  $23.4\ V_{PP}$  is needed to stretch DNA bound to the tip, as shown in Fig. 3.10 [107]. But applied voltage value has increased to  $33.3\ V_{PP}$  and  $41.1\ V_{PP}$  for the gap distances of

<sup>2</sup>C. Hyun, H. Kaur, D. S. McNabb, and J. Li, Nanotechnology 26, 125501 (2015) doi:10.1088/0957-4484/26/12/125501 “© IOP Publishing. Reproduced with permission. All Rights reserved” [107].

15  $\mu\text{m}$  and 30  $\mu\text{m}$  respectively, as shown in Fig. 3.10(b) and (c). DNA molecules attached to the tip have stretched in different configurations depending upon the separation between the electrodes. At a gap distance of 9  $\mu\text{m}$ , Fig. 3.10 angle configuration but for the separation of 15  $\mu\text{m}$  and 30  $\mu\text{m}$  the DNA are stretched in straight fashion(Fig. 3.10(b)and (c)). To represent this more clearly, cross sectional plots of the fluorescence intensity are drawn at the distances of 4  $\mu\text{m}$  and 8  $\mu\text{m}$  from the tip, which are shown below the respective fluorescent images of stretched DNA with various gap distances between electrodes. The intensity plot for Fig 3.10(a) has a broad peak at 4  $\mu\text{m}$  and two peaks at 8  $\mu\text{m}$  below the tip. On the other hand, for Fig. 3.10 (b) and (c) single peaks are observed in fluorescence intensity plots. This signifies that DNA are stretched straight between the electrodes when the gap between the electrodes is more than 15  $\mu\text{m}$  or equivalent/greater than the contour length of  $\lambda$  DNA molecule.

### 3.4 Conclusion

In this chapter, I have demonstrated that  $\lambda$  DNA immobilized on a gold coated fiber tip can be stretched using DEP force. Experimental results show that at a gap distance of 15  $\mu\text{m}$  between the tip and bottom electrode, DNA is stretched to the maximum with an external AC voltage of  $\approx 33 V_{PP}$ . A highly conductive solution causes Joule heating at low frequency and at high AC voltage. Hence temperature of solution rises, which results in a bubble formation near the bottom electrode. The DNA stretching experiments described in this chapter, give a confirmation that attachment of DNA on the tip via streptavidin-biotin, is strong enough to perform a nanopore experiment with a tuning fork force sensing probe tip. More experiments on DFP force calculation were also performed using a Tuning

fork force sensor and detailed work can be found in reference [107]. It was found that DFP force used to stretched DNA molecules is about 13 nN [107].  $\lambda$  DNA stretching has been performed with magnetic/optical tweezers experiments, and observed that about 10 pN force is required to stretch a single  $\lambda$  DNA molecule [91, 92]. However COMSOL Multiphysics simulations for our experimental setup and electrolyte solution predicts  $\approx 10$  pN DEP force for a single molecule [107]. Our experimental observation of higher DEP force suggests that a large number of molecules are tethered to the tip.

## Chapter 4

### Estimating binding efficiency of RNAP transcription factor at various positions on $\lambda$ phage DNA using Solid-State Nanopores

#### 4.1 Introduction

##### 4.1.1 DNA Protein Interactions

DNA, RNA, and Proteins are essential biomolecules of life. DNA/RNA are polymers constituted of nucleic acids, proteins are molecular chains made up of amino acid residues. These biomolecules interact with each other from time to time to carry out various cellular functions, like polymerase enzyme carry out the DNA replication prior to cell division, RecA protein helps in DNA repair, histones play an important role in chromosome maintenance. Transcription factor (TF) is a DNA binding protein, which initiates the transcription gene regulation process. TF binds to specific bases of DNA to transcribe the information from DNA to messenger RNA (mRNA). Small segments of mRNA are used as blue prints to produce new proteins via translation process. Interaction between TF and DNA is being studied with high interest due to its importance in growth processes and in response to environmental stresses. Any malfunction of TF can result in a progression of various diseases in humans [108]. In order to understand the cellular functions many techniques in biology (Footprinting assay, Electrophoretic mobility shift assay, yeast one-hybrid assay and Chromatin immunoprecipitation (ChIP) based various techniques) and computer simulations (To predict the TF based gene regulation) have been developed to unravel interactions between the DNA and proteins [109]. Various single molecule biophysical techniques have a great potential to explore an individual DNA protein complex [110, 111]. For example Optical

tweezers [112], Atomic force microscopy [113], molecular combing [114] and Nano fluidic devices together with DNA stretching and fluorescence single molecule imaging [115] techniques have been reported to map binding sites of protein on DNA. With an advancement in the nano-fabrication techniques in combination with single molecule fluorescence imaging DNA-protein binding identification mechanism [116–118] and binding kinetics [119] have also been investigated.

In the past two decades, Biological [12] and Solid state nanopores (SSN) have been well established as a biosensor to analyze the charged biopolymers like DNA, RNA and proteins [15, 21, 54]. A tremendous amount of work is done to commercialize the nanopore sensor as a next generation genome sequencer [5, 6]. However, application of the nanopore sensor is not limited to only DNA sequencing; protein unfolding through biological nanopores [60], electrical characterization of proteins through SSN [56], fast translocation dynamics for a wide range of proteins through SSN [120], controlled translocation of proteins through lipid coated silicon nitride pores [55] have also been investigated with high interest. The capacity to scan and determine the features on an individual polymer makes the nanopore sensor a suitable candidate to study the DNA- protein complexes. DNA coated with RecA proteins [61], DNA with discrete patches of RecA [62], a single large protein like RNAP [64, 121] bound to the DNA template, histone-DNA interaction in single nucleosome [69], protein-protein interactions [122] and stability of the restriction endonuclease EcoRI- DNA [68] complex have been studied with solid state nanopores. Binding of the restriction enzymes [51, 67], restriction endonucleases [68], and histones [69] to the DNA molecules have been investigated with Nanopore Force Spectroscopy experiments by voltage driven removal of proteins. Nanopore experiments combined with optical tweezers set up have been used to explore

the electrophoretic force on RecA protein assembly along the DNA length [63], translocation dynamics of the EcoRI-DNA complex [65], single RecA-DNA complex [65] and ligands bound to DNA [66]. Translocations of the RNAP-DNA transcription complexes (RNAP bound to 820 bp DNA template) through a solid state nanopore, has reported earlier [64]. They studied only one RNAP bound to two kind of DNA templates which were designed to have RNAP binding sites at different locations [64]. The basic principle of the nanopore sensor is very simple: When an electric field is applied across the nanopore membrane an ionic current is measured across the pore, which is known as open pore current,  $I_o$ . Figure 4.1 (a) shows the schematics of the experimental setup. When the charged biomolecules are added to the grounded side of the membrane, temporary current blockages, ( $\Delta I_B$ ) are observed, which are known as translocation events. An example of a current trace with various translocation events is shown in Fig. 4.1(b). We study the interactions between  $\lambda$  DNA and RNAP at different positions through SSN. *E. coli* RNA polymerase (RNAP) enzyme, binds specifically to the DNA, and starts the transcription process to synthesize the messenger RNA from the template DNA. The RNAP core enzyme is 400 kDa protein with dimensions 11 nm $\times$ 16 nm $\times$ 16 nm, has five subunits (two  $\alpha$ ,  $\beta, \beta'$  and  $\omega$ ), and  $-69e$  net molecular charge [64]. The RNAP core enzyme cannot start the transcription process because it does not have the capacity to bind DNA specifically. A subunit  $\sigma^{70}$  (70 kDa) from the family of sigma transcription initiation factors is required to transcribe the DNA to mRNA. The transcription factor  $\sigma^{70}$  binds to a 6 base pairs long specific promoter regions at  $-10$ (TATAAT) and  $-35$ (TTGACA) present in DNA (Promoter Sequence is 10 and 35 base pairs away from the transcript initial site) . The core enzyme with  $\sigma$  initiation factor is known as holoenzyme (RNAP-DNA complex with five subunits is shown in Fig. 4.1(c)).

Holoenzyme has a 470 kDa molecular weight with an overall size of 12 nm×15 nm×18 nm and  $-77e$  net charge [64]. Holoenzyme can bind specifically to the promoter site and form a closed RNAP-DNA complex with a length of approximately 50 base pairs. It has been reported earlier that RNAP has two binding sites at 3.6  $\mu\text{m}$  (38003 bp) and 4.4  $\mu\text{m}$  (35602 bp) on a 16.5  $\mu\text{m}$  (485003 bp) long  $\lambda$  DNA [115]. Apart from these, three weaker binding sites between 7–9  $\mu\text{m}$  (at about 27649 bp, 25620 bp and 23619 bp) have also been observed [115]. A schematic of five RNAP bound at different positions on  $\lambda$  DNA is shown in Fig. 4.1(d). A predicted translocation event from a  $\lambda$  DNA and RNAP complex with five units of RNAP is drawn in Fig. 4.1(d). Ideally, one should expect five subevents within an event which correspond to different positions where RNAP binds on  $\lambda$  DNA.

The translocations of formaldehyde cross-linked  $\lambda$  DNA and RNAP complexes have shown here. Many control experiments like bare RNAP, formaldehyde cross-linked RNAP, bare  $\lambda$  DNA, and formaldehyde treated  $\lambda$  DNA translocation were also performed. The subevent analysis for  $\lambda\text{DNA} + \text{RNAP}_{\text{complex}}$ ,  $\lambda$  DNA, and  $\lambda$  DNA with formaldehyde data sets were performed to extract the subevent start time. Finally, RNAP binding sites on  $\lambda$  DNA were estimated based on start time of subevent.

## 4.2 Experimental Setup

Solid state nanopores used in our work were fabricated using the Ion Beam Sculpting procedure. SiN nanopore is aligned between cis and trans chambers (prepared from PDMS) and the chambers are filled with an electrolyte, which consists of 1 M KCl and 10 mM Tris, 1 mM EDTA buffer at pH=8.0. Upon the application of electric field across the nanopore membrane an ionic current measured through a 17 nm by 21 nm size pore was  $I_o = 10.28$  pA.

Effective thickness of the nanopore can be calculated by using simple model of Ohm's law,

$$H_{eff} = \frac{\sigma A_p V}{I_o} \quad (4.1)$$

where  $\sigma=11.2$  S/m the conductivity of 1 M KCl salt solution,  $A_p$  is the area of the nanopore,  $V$  is the applied voltage and  $I_o$  is the open pore current. For  $I_o = 10.28$  pA,  $H_{eff}$  can be estimated as  $\approx 36.7$  nm for the nanopore of size 17 nm by 21 nm. To investigate the capacity of nanopore sensors to find binding sites of RNAP transcription factor at different positions on  $\lambda$  DNA,  $\lambda$  DNA-RNAP cross-linked complexes [115] are used for translocation. A cartoon sketch of a  $\lambda$  DNA+RNAP<sub>complex</sub> passing through a nanopore is shown in Fig. 4.1(d). When negatively charged biomolecules are added to cis side of the membrane, various types of translocation events are observed as shown in Fig. 4.1(b)(a current trace with various translocation events).

### 4.3 Results and Discussion

#### 4.3.1 $\lambda$ DNA+RNAP<sub>complex</sub> Translocation:

Figure 4.1 (b) represents the translocation events observed due to RNAP and  $\lambda$  DNA complexes at 120 mV. Examples of different types of events are shown in Fig. 4.2. Depending upon features (peaks observed) within an event, current blockage and dwell time of an event, these events are categorized into seven types. In Fig. 4.2 each dotted line represents a current level of 200 pA. Examples of bare  $\lambda$  DNA molecules with possible folded or unfolded configurations are shown in Fig. 4.2(a). Bare RNAP molecules translocation corresponds to the sharp and deeper blockages. Two examples of RNAP events are shown in Fig. 4.2(a).

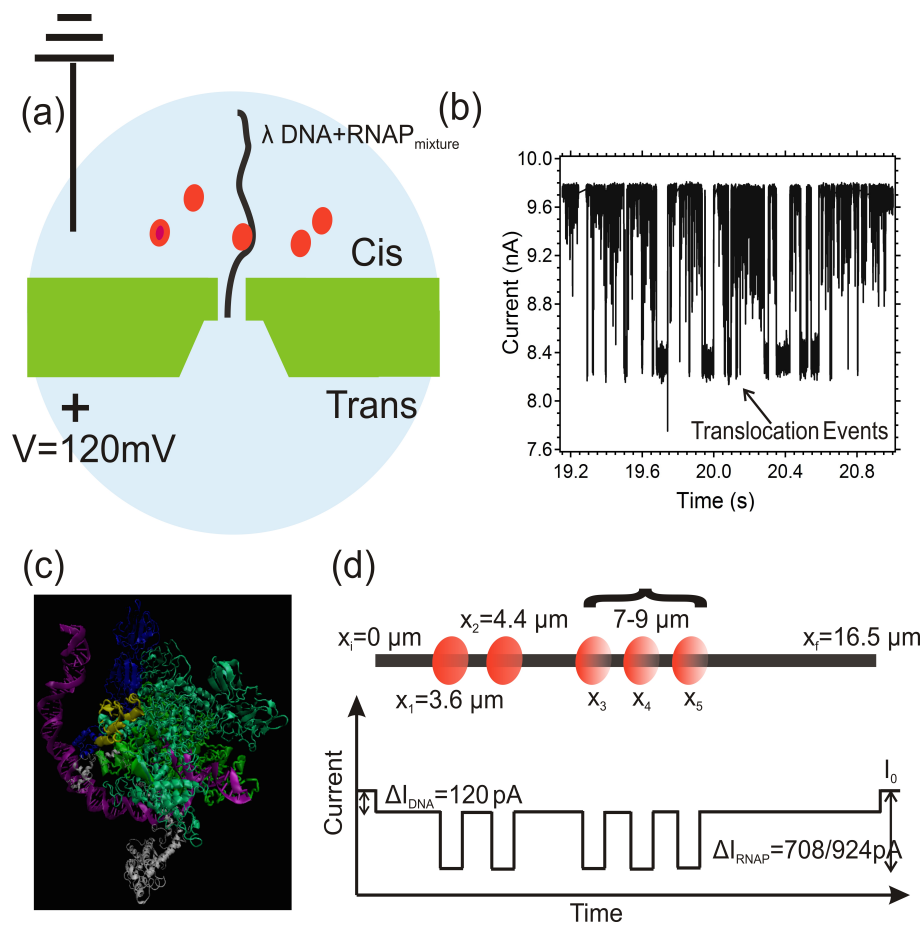


Figure 4.1: (a) A schematic drawing of a silicon nitride nanopore immersed in 1 M KCl salt solution with a mixture of  $\lambda$  DNA with RNAP. (b) Current trace of  $\lambda$  DNA and RNAP complexes passing through the nanopore of a size 17 nm by 21 nm. (c) A 3D representation of *E. Coli* RNAP-DNA<sub>complex</sub> (3IYD pdb file) [123]. Two  $\alpha$  subunits are shown in blue, subunits  $\beta$  and  $\beta'$  are in dark green and light green respectively,  $\omega$  is in yellow and  $\sigma^{70}$  factor is shown in white and purple reflects a DNA strand. (d) A schematic drawing of the RNAP bound at five possible positions on a  $16.5 \mu\text{m}$  (48,502 bp) long  $\lambda$  DNA, measured by fluorescence microscopy ([64]) and below that an ideal translocation event of  $\lambda$  DNA + RNAP<sub>complex</sub> is drawn. The multiple subevents present in an event are due to the presence of the RNAP on  $\lambda$  DNA. Current blockage levels for DNA and RNAP are estimated by ionic volume exclusion caused by DNA, and RNAP respectively while passing through a nanopore of given dimensions.

Figure 4.2(b) shows the three different examples of events with a peak in an event. Peak current level corresponds to the RNAP level and front and back level corresponds to either folded or unfolded configuration of DNA. Similarly Fig. 4.2(c), (d), (e), (f) depict the events with two, three, four, and five peaks in an event respectively. Along with these unique events huge and longer blockages are observed as shown in Fig. 4.2(g).

To characterize all these events, we defined  $\Delta I_{max}$ , maximum current drop in an event. Figure 4.3 represents  $\Delta I_{max}$  versus  $t_{dwell}$  scatter plot of all events observed at 120 mV through a nanopore of size 17 nm by 21 nm. Inset of Fig. 4.3 shows an example of a translocation event labeled with maximum current blockage  $\Delta I_{max}$ , and dwell time for a translocation,  $t_{dwell}$ . In Fig. 4.3(b) scatter plot between  $\Delta I_{max}$  and  $t_{dwell}$  for the events with no distinct peak, is superimposed on top of the scatter plot of all observed events.  $\Delta I_{max}$  versus  $t_{dwell}$  scatter plot of events having a single peak in an event is shown in Fig. 4.3(c). Similarly, Fig. 4.3 (c), (d), (e), (f) and (g) show  $\Delta I_{max}$  versus  $t_{dwell}$  scatter plots of the events containing two, three, four, and five peaks respectively. Figure 4.3(h) represents scatter plot of large and long blockages. An example of each kind of event is shown in the corresponding scatter plot.

Current histogram for all events (N=1664) is shown in Fig. 4.4(a), and is fitted with four Gaussian peaks. First peak is centered at 267.2 pA along with second, third and fourth peaks centered at 533.9 pA, 800.0 pA and 1383.0 pA respectively. It has been reported earlier that at 50 mV, core RNAP shows two conductance drops at 5.5 nS (275.0 pA) with  $t_{dwell} \approx 60 \mu s$  and 8.7 ns (475.0 pA) with  $t_{dwell} \approx 200 \mu s$  [64]. These two current drops were attributed due to different dipole orientations of the RNAP while passing through the nanopore [64]. For DNA-RNAP complex current drop  $\approx 10.5$  nS has been reported [64].

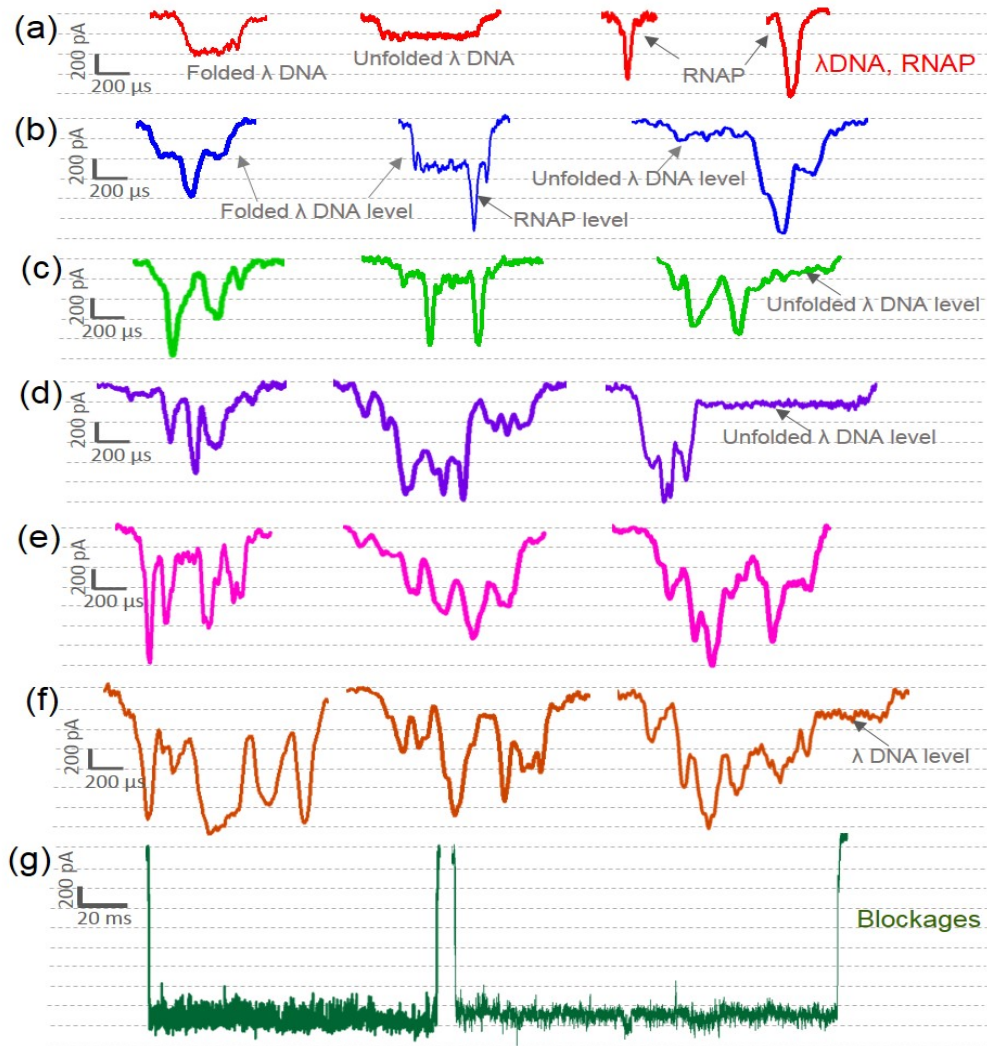


Figure 4.2: Examples of different types of translocation events observed with no peak to multiple peaks within an event from a 17 nm  $\times$  21 nm pore are shown. (a) Bare  $\lambda$  DNA (folded and unfolded) and bare RNAP events. (b) represents the three events with a single peak (current level RNAP). (c) shows the events with two peaks. (d) exhibits events with three peaks. (e) shows the events with four peaks. (f) displays the events with five peaks (g) displays the long and deep current blockages.

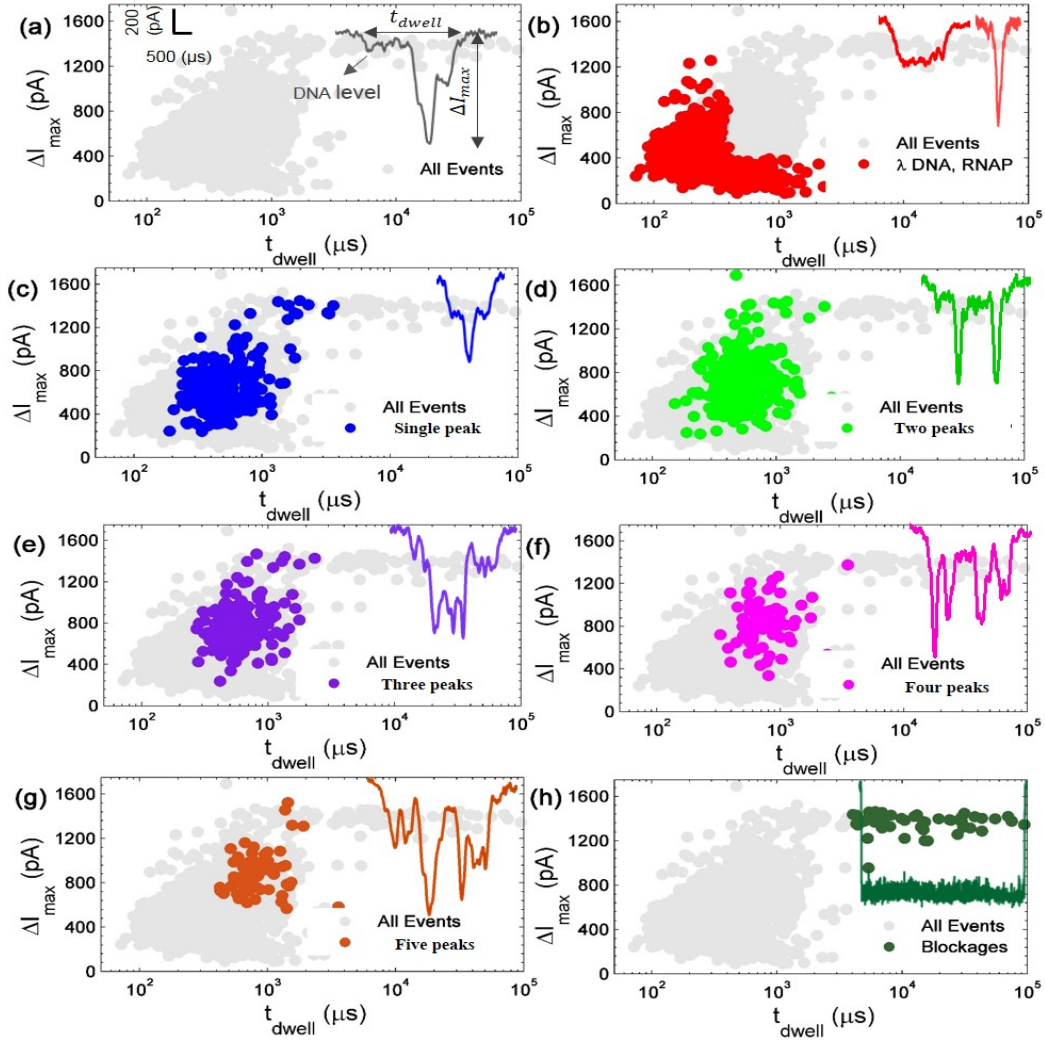


Figure 4.3:  $\Delta I_{max}$  versus  $t_{dwell}$  scatter plot of events observed at 120 mV through a nanopore of size 17 nm by 21 nm. Inset of the plot shows the translocation event with maximum current blockage,  $\Delta I_{max}$ , and dwell time,  $t_{dwell}$ . (b) Scatter plot of the bare  $\lambda$  DNA and RNAP events is plotted above the scatter plot of all observed events. (c) Scatter plot between  $\Delta I_{max}$  and  $t_{dwell}$  of events having a single peak within an event is shown above the scatter plot of all observed events. Similarly  $\Delta I_{max}$  versus  $t_{dwell}$  scatter plots of the events containing (d) two, (e) three, (f) four, and (g) five peaks within an event, and are shown above the scatter plot of all events. (h) shows the scatter plot of large and long blockages. An example for each kind of event is shown in the corresponding scatter plot.

As reported earlier, we also estimated the current drop due to RNAP as electrolyte volume excluded by the molecules while passing through the nanopore. The current drop,  $\Delta I$  can be predicted by using following equation [64, 122, 124],

$$\Delta I = \frac{\gamma \sigma V_{excluded} V_a}{H_{eff}^2} f \left( \frac{d_p}{d_m} \right) \quad (4.2)$$

where  $\gamma$  is a shape factor,  $\sigma$  is the solution conductivity,  $V_{excluded}$  is the volume excluded by translocating molecule,  $V_a$  is applied voltage,  $H_{eff}$  is the effective thickness of the nanopore and  $f$  is the correction factor that depends upon the diameter of pore,  $d_p$  and diameter of the molecule,  $d_m$ . The  $\lambda$  DNA and RNAP complex mixture added on the cis side has  $\approx 2.5\%$  glycerol content as a result conductance of the pore will be reduced and hence current drop due to translocation. A change in the baseline (open pore current) from 10.275 nA to 9.72 nA was observed. For a pore of size 17 nm by 21 nm with  $H_{eff} = 36.7$  nm,  $\sigma = 9.6$  S/m (with 2.5% glycerol in 1 M KCl), and core enzyme volume  $V_{excluded} = 518$  nm<sup>3</sup> [64], one should expect two peaks around 5.4 ns (650 pA) and 7.0 ns (847 pA) for two different shape factors, 1.38 and 1.80 respectively. Also for DNA-RNAP complex region  $V_{excluded} = 737$  nm<sup>3</sup> (volume of holoenzyme + volume DNA length inside pore assuming it is linear) an estimated current drop (when complex region is passing through the nanopore) is 924 nA or 1205 nA depending upon the orientation of RNAP. These predicted values suggest the second and third peaks could be due to the RNAP events. Fourth peak observed in Fig. 4.4(a) may be due to DNA+RNAP complexes. First peak can be attributed to bare DNA and subunits of RNAP. Next, The dwell time histogram is plotted for all events in Fig. 4.3.  $t_{dwell}$  histogram for all events shows two peaks, first peak centered at 241  $\mu$ s and second peak centered at 430  $\mu$ s is due to bare DNA and various DNA and RNAP complexes. Second peak in Fig.4.3(a) is

fitted with probability density function (PDF) of 1D diffusion model proposed earlier [88, 89]

$$P(t) = \frac{NLe^{-\frac{(L-vt)^2}{4tD}}}{t\sqrt{4\pi tD}} \quad (4.3)$$

where  $N$  normalized coefficient,  $L = L_{DNA} + H_{eff}$  and  $L_{DNA} \approx 16.5 \mu\text{m}$  for  $\lambda$  DNA molecule,  $v$  is the mean translocation velocity and  $D$  is the diffusion constant. The fitting parameters obtained from least square fitting of the second peak in Fig. 4.4 are  $v = 29.45 \mu\text{m/ms}$  and  $D = 47.92 \mu\text{m}^2/\text{ms}$ . The mean translocation velocity is very high as compared to only  $\lambda$  molecules (shown in Fig. 3.9(b)). Time histogram does not suggest presence of a large number of  $\lambda$  DNA molecules. Also, the peaks observed with in an event (observed in different events as shown in Fig. 4.2) either due to presence of RNAP in the nanopore or due to interaction between the RNAP and nanopore walls, such that the molecule is just dangling inside the nanopore volume. It is difficult to infer the binding of RNAP from these type of events. To overcome this problem, a nanopore of a little larger dimension was used along with 5% glycerol in 1 M KCl with 10 mM Tris, and 1 mM EDTA buffer at pH=8.0.

Next, a pore of 23.7 nm by 20.4 nm was opened with 1 M KCl and 10 mM Tris, 1 mM EDTA buffer with 5% glycerol at pH=8.0. When electric field is applied across the nanopore membrane a stable open pore current,  $I_o = 9.1 \text{ nA}$  and  $I_{rms}$  less than 20 pA was obtained. RNAP and  $\lambda$  DNA complex were cross-linked with formaldehyde at 4°C for 30 minutes and were added to the cis side. Similar to current trace Fig. 4.1(b), a broad range of events were observed. Figure 4.5(a) shows an example of each kind of event and a scatter plot between average current drop,  $\Delta I_B$  and  $t_{dwell}$  for the translocation events of  $\lambda$  DNA+RNAP<sub>mixture</sub> is shown in Fig. 4.5(b). By introducing 5% glycerol in salt solution our pore has become stable for a longer time and events observed with  $\lambda$  DNA+RNAP<sub>mixture</sub> (Fig. 4.5) are more

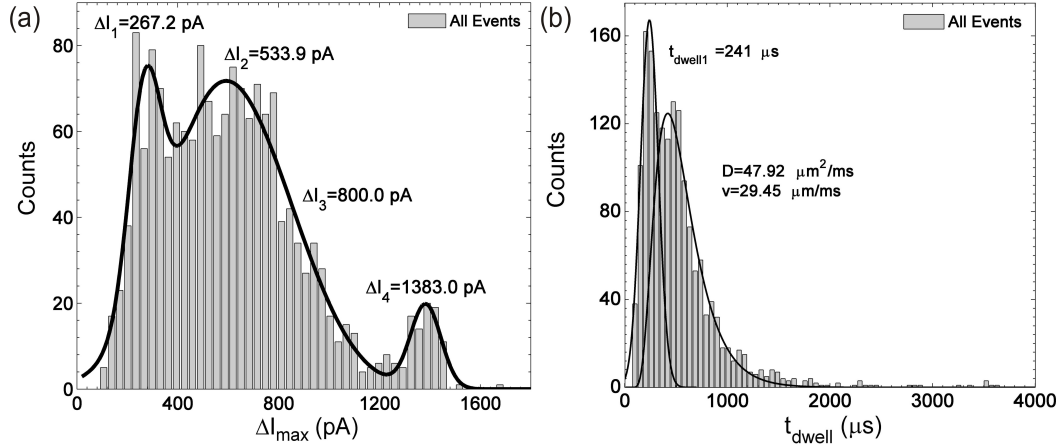


Figure 4.4: (a) Current histogram of all the events observed at 120 mV. Four peaks correspond to bare  $\lambda$  DNA, RNAP subunits, bare RNAP, and various  $\lambda$  DNA and RNAP complexes. (b) Dwell time histogram of all events observed at 120 mV, which distributes the events in two peaks. First peak centered at 241  $\mu\text{s}$  corresponds to bare RNAP, and second displays all events that consists bare  $\lambda$  DNA, and various  $\lambda$  DNA and RNAP complexes.

smoother than events observed with smaller pore Fig. 4.2. We hypothesize that glycerol had coated the nanopore wall in such a way that these large fluctuations in events have disappeared. Even though the current blockages values have been greatly reduced by using larger pores, we could distinguish between the events due to bare DNA and or due to RNAP bound on DNA in a better way. Hereafter, all the control experiments were performed under similar conditions.

Figure 4.5(b) shows four different kinds of populations observed with  $\lambda$  DNA+RNAP<sub>mixture</sub>. Three populations (RNAP<sub>I</sub>, RNAP<sub>II</sub>, and RNAP<sub>III</sub>) are attributed due to translocations of RNAP enzyme and its subunits at 120 mV and a fourth one is assigned to only  $\lambda$  DNA and  $\lambda$  DNA+RNAP<sub>complex</sub>. Figure 4.5(b) shows  $\Delta I_B$  and  $t_{dwell}$  histograms for all populations and counts are normalized to one for comparison. Events labeled under RNAP<sub>I</sub> are centered at 69 pA with 65  $\mu\text{s}$  and another weak peak at 82 pA. RNAP<sub>II</sub> has two peaks at 106 pA and 118 pA and the corresponding time distribution is very broad with a peak at 65  $\mu\text{s}$ , however

these events are distributed from 50  $\mu\text{s}$  to 10000  $\mu\text{s}$ . RNAP<sub>III</sub> has wide current blockage and dwell time distributions with peak values at 141 pA and 104  $\mu\text{s}$  respectively. Fourth population due to  $\lambda$  DNA and  $\lambda$  DNA+RNAP<sub>complex</sub> has maximum peak at 156 pA along with small peak at about 170 pA and distributed up to 260 pA. This population has the  $t_{dwell}$  distribution peak at 2.5 ms, typical of  $\lambda$  DNA events. To support the assumption about events division in four categories, the control experiments of bare RNAP (RNAP<sub>bare</sub>), formaldehyde cross-linked RNAP (RNAP<sub>formaldehyde</sub>), bare  $\lambda$  DNA ( $\lambda$  DNA<sub>bare</sub>) and formaldehyde cross-linked  $\lambda$  DNA ( $\lambda$  DNA<sub>formaldehyde</sub>) molecules are compared next.

#### 4.3.2 Comparison with RNAP<sub>bare</sub> and RNAP<sub>formaldehyde</sub>

The translocations of bare RNAP (RNAP<sub>bare</sub>) and formaldehyde cross-linked RNAP (RNAP<sub>formaldehyde</sub>) molecules were performed through the same pore. Before adding any new sample of molecules to the cis side, the nanopore was rinsed with plenty of 1 M KCl (5% glycerol) solution such that no more events were detected. Figure 4.6(b) shows a scatter plot of RNAP<sub>bare</sub> and RNAP<sub>formaldehyde</sub> translocations through a 23.7 nm by 20.4 nm nanopore at 120 mV. Events observed with RNAP<sub>bare</sub> are very sharp with mean translocation time of 54  $\mu\text{s}$  and current blockage is centered at 89 pA and with another small population at 110.0 pA at 74  $\mu\text{s}$  ( $\Delta I_B$  and  $t_{dwell}$  histograms of RNAP<sub>bare</sub> events are shown in Fig. 4.6(b)). Few examples of RNAP<sub>bare</sub> events are shown in Fig 4.6(a). We performed translocation experiment of RNAP cross-linked with formaldehyde at 4°C for 30 minutes. The scatter plot of RNAP<sub>formaldehyde</sub> translocation events is shown in Fig. 4.6(b) along with RNAP<sub>bare</sub> events. Interestingly, we observed that RNAP<sub>formaldehyde</sub> shows three distinct populations of events as shown in Fig. 4.6(a).  $\Delta I_B$  histogram of RNAP<sub>formaldehyde</sub> events shows three peaks at

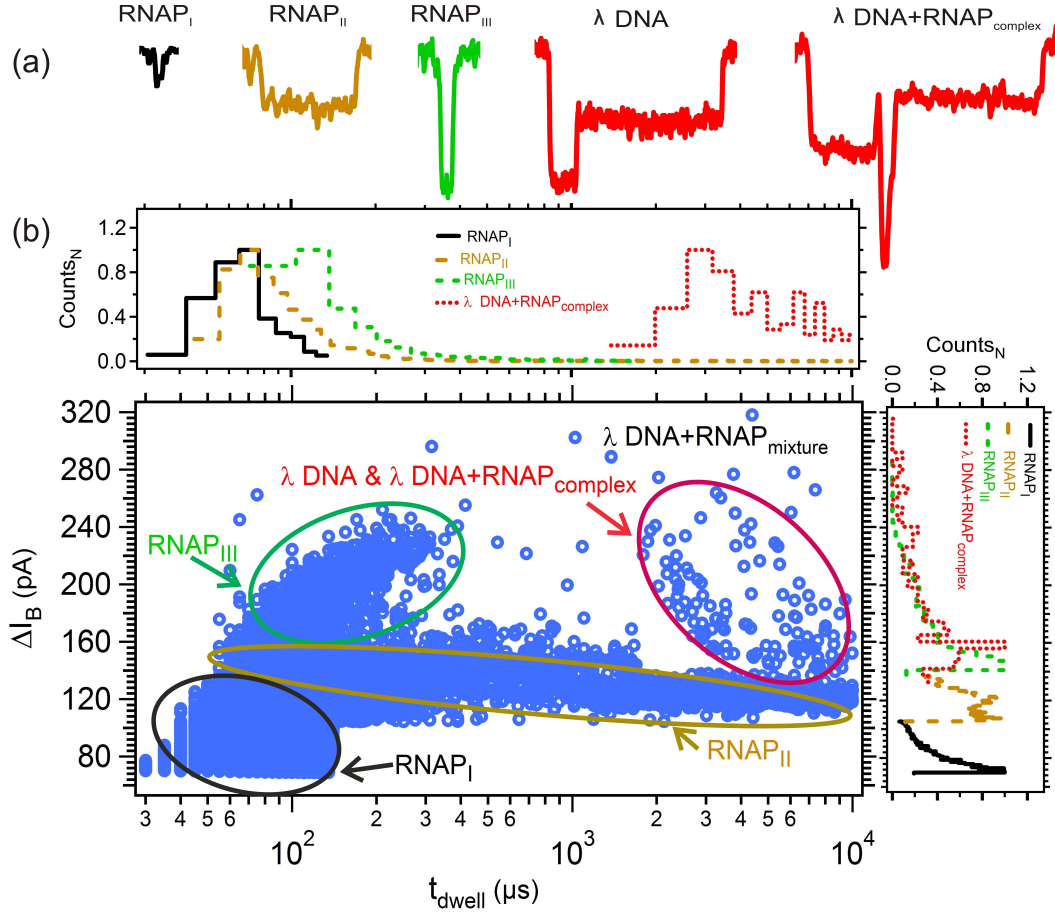


Figure 4.5: (a) Various kinds of events observed with  $\lambda$  DNA+RNAP<sub>mixture</sub> through a 23.7 nm by 20.4 nm pore at 120 mV. (b) Scatter plot between  $\Delta I_B$  and  $t_{dwell}$  for  $\lambda$  DNA+RNAP<sub>mixture</sub> at 120 mV. Four different kinds of events are observed with  $\lambda$  DNA+RNAP<sub>mixture</sub> and are circled as RNAP<sub>I</sub>, RNAP<sub>II</sub>, RNAP<sub>III</sub>, and  $\lambda$  DNA &  $\lambda$  DNA+RNAP<sub>complex</sub>. RNAP<sub>I</sub>, RNAP<sub>II</sub>, and RNAP<sub>III</sub> events are due to core RNAP and RNAP subunits and forth population is a mixture of  $\lambda$  DNA, and  $\lambda$  DNA bound to RNAP ( $\lambda$  DNA+RNAP<sub>complex</sub>). The current blockage histograms (left side) and dwell time histograms (above) are plotted for each population, and are normalized to one for comparison. RNAP<sub>I</sub> events are centered at 69 pA with small population at 82 pA and dwell time distribution centered at 55  $\mu$ s. RNAP<sub>II</sub> has a broad time distribution and current blockage has two peaks 106 pA and 118 pA. RNAP<sub>III</sub> has a broad  $\Delta I_B$  distribution with a peak at 141 pA with a small population that extends to 250 pA. The mean translocation time for RNAP<sub>III</sub> is 104  $\mu$ s. The fourth population is typical of  $\lambda$  DNA translocations events, has a average current drop peak at 156 pA with a mean translocation time of 2.5 ms.

107.6 pA, 125.8 pA and 147.5 pA respectively and  $t_{dwell}$  histogram RNAP<sub>formaldehyde</sub> events shows exponential behavior with a peak value of 63.6  $\mu$ s. We labeled these populations as RNAP<sub>I</sub>, RNAP<sub>II</sub>, and RNAP<sub>III</sub> are circled as shown in Fig. 4.6(b). For further comparison, we plotted normalized  $\Delta I_B$  and  $t_{dwell}$  histograms for these populations and are shown in Fig. 4.6(c). The RNAP<sub>I</sub> population is centered at 104 pA and events are very sharp with mean translocation time of 53  $\mu$ s and this type of events overlap RNAP<sub>bare</sub> events. RNAP<sub>III</sub> population (499 events) is mainly centered at 175 pA with another population centered at 195 pA as shown in  $\Delta I_B$  histogram of RNAP<sub>III</sub> events in Fig. 4.6(d). Figure 4.6(e) shows  $t_{dwell}$  histogram RNAP<sub>III</sub> events have a mean translocation time of 110  $\mu$ s. Again events under RNAP<sub>II</sub> (4920 events) population have two peaks 127 pA and 146 pA as shown in Fig. 4.6(d). It is evident from the scatter plot of RNAP<sub>formaldehyde</sub> (Fig. 4.6(a)) that RNAP<sub>II</sub> events with smaller current blockage has a broad translocation time distribution from 50  $\mu$ s to 10000  $\mu$ s. We also observed translocation events of RNAP<sub>bare</sub> and RNAP<sub>formaldehyde</sub> at 60 mV. Interestingly, at 60 mV scatter plot of  $\Delta I_B$  versus  $t_{dwell}$  for RNAP<sub>bare</sub> imbricates the scatter plot of RNAP<sub>formaldehyde</sub> events(as shown in Fig. 4.6(c)), contrary to the case of 120 mV, where RNAP<sub>bare</sub> events cover only RNAP<sub>I</sub> population (Fig. 4.6(b) and (c)). This implies RNAP<sub>I</sub> population observed at 120 mV for RNAP<sub>formaldehyde</sub> is not observed in case of RNAP<sub>bare</sub> and RNAP<sub>formaldehyde</sub> translocations at 60 mV. It has been reported earlier that at 50 mV, core RNAP shows two conductance drops at 5.5 nS (275.0 pA) with  $t_{dwell} \approx 60 \mu$ s and 8.7 nS (475.0 pA) with  $t_{dwell} \approx 200 \mu$ s [64]. These two current drops were attributed to the two different dipole orientations of the RNAP while passing through the nanopore [64]. RNAP<sub>bare</sub> and RNAP<sub>formaldehyde</sub> translocations are observed with  $\approx 2.5\%$  glycerol content due to CLB buffer. For a nanopore of size 23.7 nm by 20.4 nm with  $H_{eff} = 50$  nm,  $\sigma$

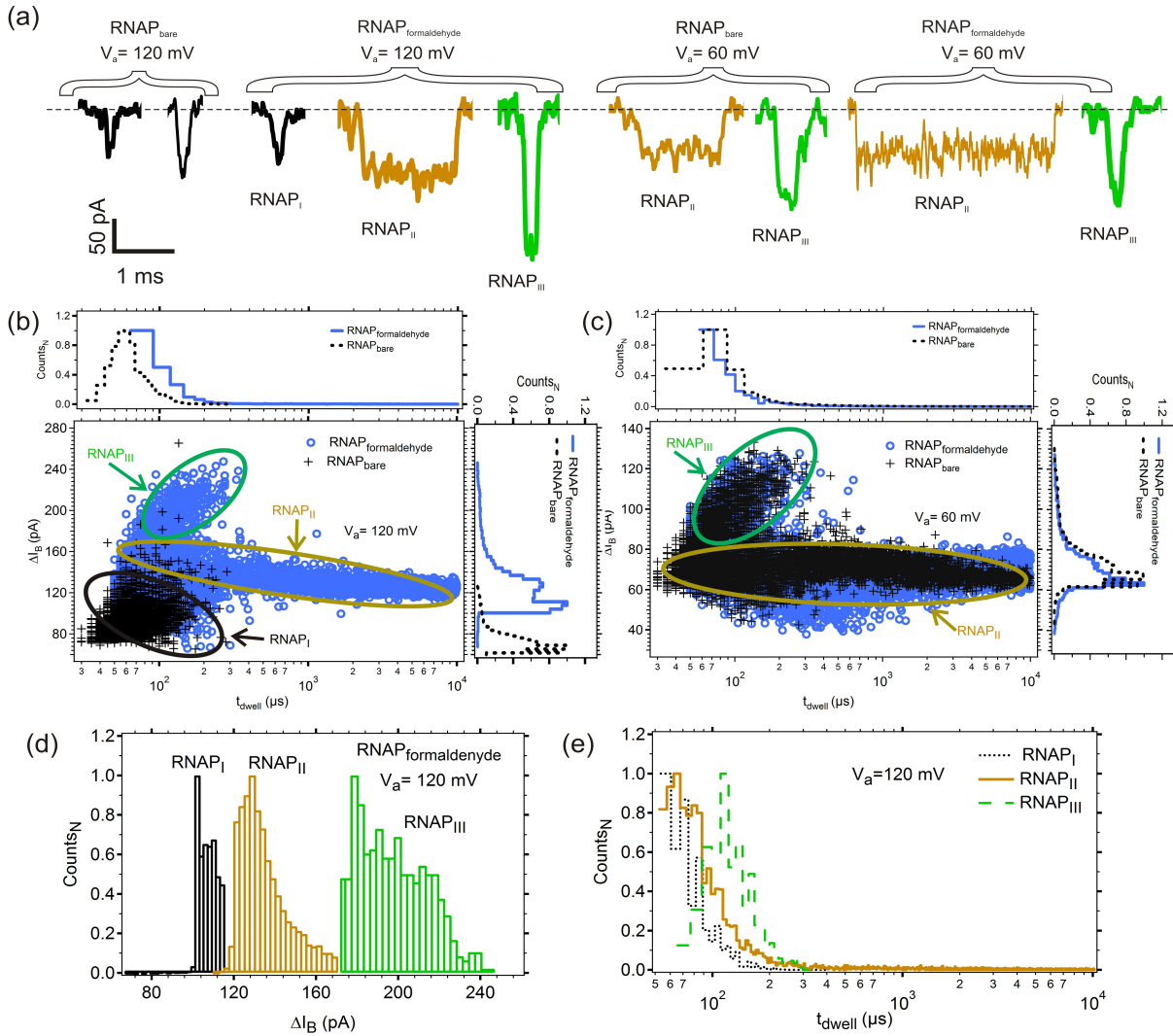


Figure 4.6: (a) Some examples of the translocation events observed with bare RNAP (RNAP<sub>bare</sub>) and formaldehyde cross-linked RNAP (RNAP<sub>formaldehyde</sub>) at 120 mV and 60 mV are shown respectively (b) Scatter plots between  $\Delta I_B$  and  $t_{dwell}$  for RNAP<sub>bare</sub>, and RNAP<sub>formaldehyde</sub> translocations through 23.7 nm by 20.4 nm nanopore at 120 mV.  $\Delta I_B$  histograms and  $t_{dwell}$  histograms for RNAP<sub>bare</sub> and RNAP<sub>formaldehyde</sub> are plotted to the left side, and on the top of scatter plot respectively. As compared to bare RNAP molecules two more populations are observed with RNAP<sub>formaldehyde</sub> at 120 mV. (c) Scatter plot between  $\Delta I_B$  and  $t_{dwell}$  for the RNAP<sub>bare</sub>, and RNAP<sub>formaldehyde</sub> translocations through the same nanopore at 60 mV.  $\Delta I_B$  histograms and  $t_{dwell}$  histograms for the RNAP<sub>bare</sub>, and RNAP<sub>formaldehyde</sub> are plotted to the left side, and on the top of the scatter plot respectively. At 60 mV, the RNAP<sub>bare</sub>, and RNAP<sub>formaldehyde</sub> show mainly two populations. RNAP<sub>I</sub> like events observed at 120 mV, are not observed at 60 mV. (d)  $\Delta I_B$  histograms of three individual populations RNAP<sub>I</sub>, RNAP<sub>II</sub>, and RNAP<sub>III</sub> (events under different circles in Fig. 4.6(b)) are plotted for a better comparison for 120 mV. (e) Dwell time distributions of the RNAP<sub>I</sub>, and RNAP<sub>II</sub> decay exponentially, on the other hand, RNAP<sub>III</sub> has a peak around 110  $\mu$ s. RNAP<sub>II</sub> population has a broad time distribution.

$=10.6 \text{ S/m}$  (with 2.5% glycerol in 1 M KCl),  $V_{excluded} = 518 \text{ nm}^3$  for RNAP core enzyme [64], at 120 mV, one should expect two peaks around 350 pA and 446 pA for two different shape factors 1.39 and 1.77 respectively. Raillon et. al. reported that at high voltage 200 mV, along with DNA-RNAP complex various translocation events due to subunits  $\beta$ ,  $\beta'$ , and  $\beta'\sigma$  (in two orientations) were observed. We also estimated the current blockages due to these subunits with our nanopore dimensions using Eq. 4.2 at 120 mV. We should see a peak of 118 pA due to  $\beta$ ,  $\beta'$  and for  $\beta'\sigma$  complex predicted current drops are 214 pA and 292 pA for shape factors 1.37 and 1.87 respectively. We hypothesize that at 120 mV the observed events are due to  $\beta$  and  $\beta'$  subunits with RNAP<sub>bare</sub> sample. For RNAP<sub>formaldehyde</sub> sample two peaks of current drop are observed from both RNAP<sub>III</sub> (175 pA and 195 pA), and RNAP<sub>II</sub> (127 pA and 146 pA), which represents two different orientations of core RNAP and  $\beta'\sigma$  complex respectively. We propose that the current drop for RNAP<sub>I</sub> population around 104 pA is due to  $\beta$ , and  $\beta'$  subunits. The observed current blockage values are much smaller than predicted current drops for all the subunits and complexes. This discrepancy between the observed and estimated current blockages could be due to many factors like actual pore dimensions, estimated hydrodynamic volume of molecules, ionic fluctuations and use of glycerol (CLB). Also, 60 mV data for both RNAP<sub>bare</sub> and RNAP<sub>formaldehyde</sub> do not show the RNAP<sub>I</sub> population, which is similar to Raillon et. al. observation at 50 mV where  $\beta$ ,  $\beta'$  events with DNA-RNAP complex were not observed [64].

### 4.3.3 Comparison with $\lambda \text{ DNA}_{bare}$ and $\lambda \text{ DNA}_{formaldehyde}$

To compare the fourth population observed in Fig. 4.5(b), the control experiments with the  $\lambda \text{ DNA}_{bare}$  and  $\lambda \text{ DNA}_{formaldehyde}$  were performed through a nanopore of size 19.5 nm

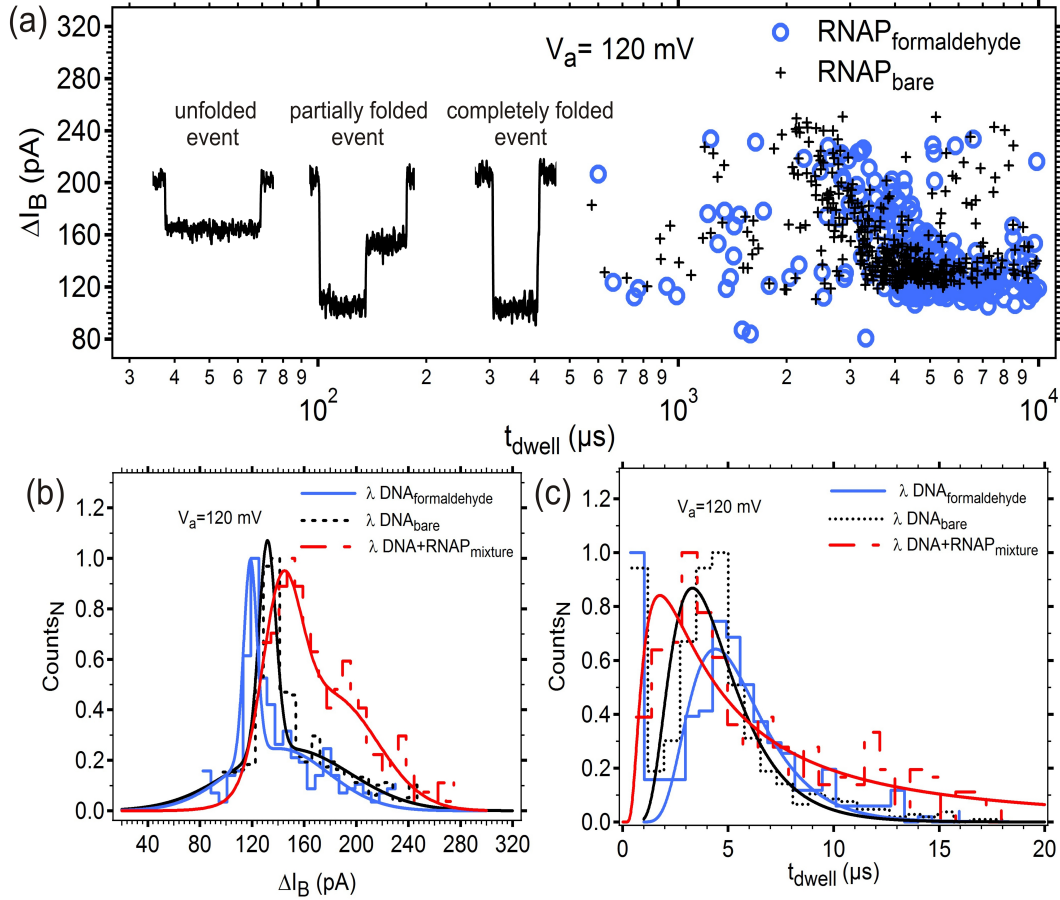


Figure 4.7: (a)  $\Delta I_B$  versus  $t_{dwell}$  scatter plots for bare  $\lambda$  DNA ( $\lambda$  DNA<sub>bare</sub>), and formaldehyde treated  $\lambda$  DNA ( $\lambda$  DNA<sub>formaldehyde</sub>) translocation events through a 19.5 nm by 15.6 nm nanopore at 120 mV. Three kinds of events (unfolded, partially folded and completely folded) are observed with both ( $\lambda$  DNA<sub>bare</sub> and  $\lambda$  DNA<sub>formaldehyde</sub>) and an example of each kind of event is shown in the inset. (b) Comparison between  $\Delta I_B$  histograms of the fourth population observed with  $\lambda$  DNA+ RNAP<sub>mixture</sub> through 23.7 nm by 20.4 nm nanopore, and  $\lambda$  DNA<sub>bare</sub>, and  $\lambda$  DNA<sub>formaldehyde</sub> (5% glycerol) through a nanopore of size 19.5 nm by 15.6 nm at 120 mV. (c)  $t_{dwell}$  histograms of  $\lambda$  DNA+ RNAP<sub>mixture</sub>,  $\lambda$  DNA<sub>bare</sub>, and  $\lambda$  DNA<sub>formaldehyde</sub> at 120 mV.

by 15.6 nm with  $I_o = 9.1$  nA at 120 mV. The scatter plots between  $\Delta I_B$  and  $t_{dwell}$  for  $\lambda$  DNA<sub>bare</sub> and  $\lambda$  DNA<sub>formaldehyde</sub> are shown in Fig. 4.7(a) (Each translocation experiment was performed with 1 M KCL and 5% glycerol, and nanopore was rinsed thoroughly before adding any new sample). The fourth population appearing in Fig. 4.5 resembles the scatter plots of Fig. 4.7(a). We further compared current blockage histograms of the fourth population observed with  $\lambda$  DNA+RNAP<sub>mixture</sub> (271 events),  $\lambda$  DNA<sub>bare</sub> (610 events), and  $\lambda$  DNA<sub>formaldehyde</sub> (305 events) as shown in Fig. 4.7(b). All the histograms,  $\lambda$  DNA+RNAP<sub>mixture</sub> (142.6 pA, and 180.6 pA),  $\lambda$  DNA<sub>bare</sub> (131.8 pA, and 148.6 pA) and  $\lambda$  DNA<sub>formaldehyde</sub> (118.7 pA and 140.5 pA) show two peaks of current blockage. It is evident from Fig. 4.7(b) that formaldehyde cross linked  $\lambda$  DNA has a smaller current drop than  $\lambda$  DNA<sub>bare</sub> and the  $\lambda$  DNA+RNAP<sub>mixture</sub> has the highest current drop among all.  $\lambda$  DNA<sub>bare</sub>, and  $\lambda$  DNA<sub>formaldehyde</sub> trans-locations were performed with 1 M KCl and 5% glycerol, on the other hand  $\lambda$  DNA+RNAP<sub>mixture</sub> translocation were performed with 2.5% glycerol. It has been shown earlier that presence of glycerol in salt solution increases translocation time, but decreases the current drop value [18]. So an increase in the current drop level of  $\lambda$  DNA+RNAP<sub>mixture</sub> could be due to the low concentration of glycerol.

Another point to note here is that second current drop peak amplitude is about 20% of first peak for both  $\lambda$  DNA<sub>bare</sub>, and  $\lambda$  DNA<sub>formaldehyde</sub>, but the amplitude of second peak is increased to 50% in the case of  $\lambda$  DNA+RNAP<sub>mixture</sub>. As reported previously, we also observed three different kinds of events due to unfolded, partially folded and completely folded configurations of  $\lambda$  DNA as it passed through the nanopore [125], which are shown in Fig. 4.7(a). First peak is attributed to unfolded events and second is due to the average of current drop folded and unfolded level of DNA within an event. We also compared

first passage time distribution of  $\lambda$  DNA +RNAP<sub>mixture</sub>,  $\lambda$  DNA<sub>bare</sub>, and  $\lambda$  DNA<sub>formaldehyde</sub>, which is shown in Fig. 4.7(c). All  $t_{dwell}$  histograms are fitted with a probability density function (PDF) given by Eq. 4.3 with  $H_{eff} = 30$  nm for 19 nm x 15 nm pore used for  $\lambda$  DNA<sub>bare</sub> and  $\lambda$  DNA<sub>formaldehyde</sub> translocations. The fitting parameters obtained from least square fitting for  $\lambda$  DNA +RNAP<sub>mixture</sub> are  $v = 2.4$   $\mu\text{m}/\text{ms}$ , and  $D = 18.9$   $\mu\text{m}^2/\text{ms}$ . On the other hand, least square fits of  $\lambda$  DNA<sub>bare</sub> and  $\lambda$  DNA<sub>formaldehyde</sub> produced  $v = 3.6$   $\mu\text{m}/\text{ms}$ ,  $D = 6.4$   $\mu\text{m}^2/\text{ms}$  and  $v = 2.9$   $\mu\text{m}/\text{ms}$ ,  $D = 3.8$   $\mu\text{m}^2/\text{ms}$ , respectively. Translocation of  $\lambda$  DNA<sub>formaldehyde</sub> has smaller diffusion coefficient and slow mean translocation velocity as compared to  $\lambda$  DNA<sub>bare</sub>. Even though the glycerol condition (5%) was same for both  $\lambda$  DNA<sub>bare</sub> and  $\lambda$  DNA<sub>formaldehyde</sub>, the translocation velocity has reduced with the formaldehyde addition to  $\lambda$  DNA. While  $\lambda$  DNA +RNAP<sub>mixture</sub> has relatively small velocity, it has a larger diffusion coefficient and  $t_{dwell}$  distribution is much broader than  $\lambda$  DNA<sub>bare</sub> and  $\lambda$  DNA<sub>formaldehyde</sub>.

The fourth population of Fig. 4.5, is a combination of only  $\lambda$  DNA events (can be folded, unfolded and partially folded as shown in Fig. 4.7(a)) and  $\lambda$  DNA +RNAP<sub>complex</sub> events (that contains subevents with in an event). Figure 4.5 (a) shows an example of both of these events. Typically, three types of events are observed with  $\lambda$  DNA+RNAP<sub>complex</sub> translocation through the nanopore and are shown in Fig. 4.8, along with the possible configurations of  $\lambda$  DNA +RNAP<sub>complex</sub> with respect to the nanopore. Events with multiple subevents are attributed to the  $\lambda$  DNA +RNAP<sub>complex</sub> molecules. Depending upon the different configurations of events, these events were divided into three different types. First type occurred, when a  $\lambda$  DNA with single RNAP enters the nanopore in unfolded configuration as shown in Fig. 4.8(a), and stays unfolded during its passage. These events have two possible config-

urations; either  $\lambda$  DNA +RNAP<sub>complex</sub> enters with the RNAP side first or with the RNAP side at the end. Examples of these two events are shown in Fig. 4.8(a). The second type of events are when DNA is captured at a different location than its end such that the first part of the event shows a folded level and the RNAP current drop level follows after that. Two examples of such events are shown in Fig. 4.8(b). The first event of Fig. 4.8(b) shows that RNAP level came right after the folded level and the other event depicts the RNAP level close to its exit. Figure 4.8(c) represents the third kind of events,  $\lambda$  DNA+RNAP<sub>complex</sub> is captured in such a way that the RNAP current blockage level lies within the folded part of an event. Again, two examples of such events are shown in Fig. 4.8(c), where RNAP level occurs in the beginning or at the end of the folded level within an event. Next, we separate out  $\lambda$  DNA and  $\lambda$  DNA+RNAP<sub>complex</sub> events from the  $\lambda$  DNA+RNAP<sub>mixture</sub> translocation. Out of 271 events, 137 events are due to only  $\lambda$  DNA and 101 events are due to  $\lambda$  DNA +RNAP<sub>complex</sub>, and the rest of the events are complicated. These complicated events were ignored for further analysis. This implies that 42.4%  $\lambda$  DNA binds with RNAP molecule to form open complexes. We then compared the  $\Delta I_B$  and  $t_{dwell}$  histograms for both  $\lambda$  DNA, and  $\lambda$  DNA +RNAP<sub>complex</sub> events separated from the fourth population of Fig. 4.5(b). For these events, we took  $\Delta I_B$  as the average current blockages of all the levels within an event. For  $\lambda$  DNA events, current histogram depicts two peaks at 137 pA and 204 pA, and  $\lambda$  DNA +RNAP<sub>complex</sub> events has two peaks at 285 pA and 335 pA. That is why the  $\Delta I_B$  histogram of  $\lambda$  DNA events from  $\lambda$  DNA+RNAP<sub>mixture</sub> is different than the one observed for  $\lambda$  DNA<sub>bare</sub> which is shown in Fig. 4.9(a). We further compared dwell time distribution for  $\lambda$  DNA events and  $\lambda$  DNA+RNAP<sub>complex</sub> events from  $\lambda$  DNA+RNAP<sub>mixture</sub> events. The  $t_{dwell}$  histogram of only  $\lambda$  DNA is typical of  $\lambda$  DNA translocation events. The  $t_{dwell}$  histogram was fitted with

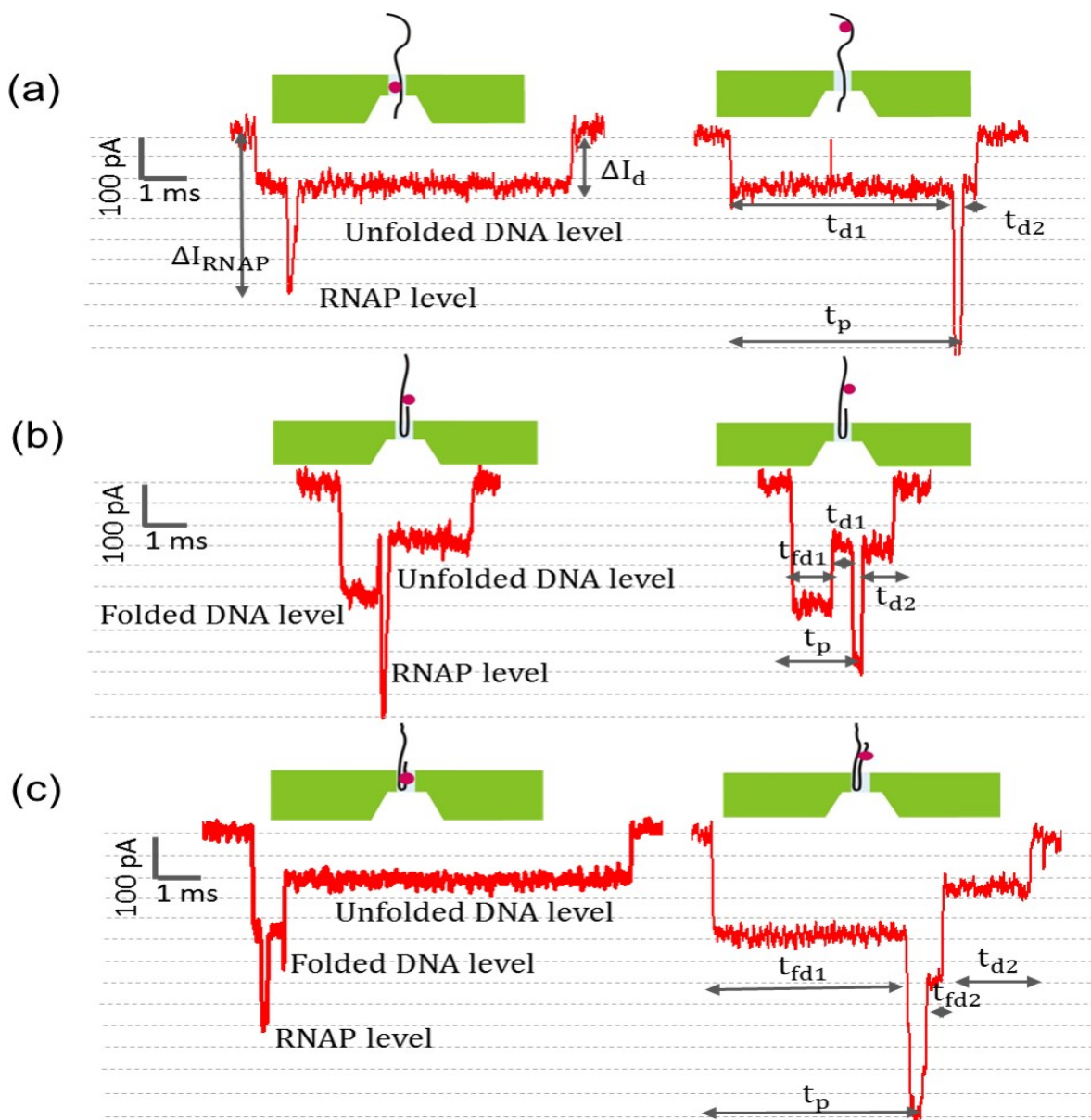


Figure 4.8: Examples of the different types of translocation events observed with a peak within a  $\lambda$  DNA translocation event are shown. (a) Two examples of  $\lambda$  DNA+RNAP<sub>complex</sub> events with a single RNAP peak in the unfolded DNA level. (b) Second kind of events with a single peak (current level corresponds to the RNAP) and DNA folded part. RNAP bound to  $\lambda$  DNA comes after the folded region of the DNA has passed through. (c) Third type of  $\lambda$  DNA+RNAP<sub>complex</sub> events, where a RNAP peak occurs within the folded part of DNA during initial capture.

PDF from Eq. 4.3 with fitting parameters  $v = 3.6 \mu\text{m}/\text{ms}$  and  $D = 9.7 \mu\text{m}^2/\text{ms}$ .  $\lambda$  DNA events separated from the fourth population of  $\lambda$  DNA+RNAP<sub>mixture</sub> have the same velocity as  $\lambda$  DNA<sub>bare</sub> and higher velocity compared to  $\lambda$  DNA<sub>formaldehyde</sub>. One would expect mean translocation velocity for only  $\lambda$  DNA events (separated from  $\lambda$  DNA+RNAP<sub>mixture</sub>) to be closer to the mean velocity as both the samples were treated with formaldehyde at 4°C for 30 minutes. But the  $\lambda$  DNA<sub>formaldehyde</sub> translocations were performed with 5% glycerol and the  $\lambda$  DNA +RNAP<sub>mixture</sub> sample has 2.5% glycerol when it was transferred to the cis chamber. So an increase in mean translocation velocity of only  $\lambda$  DNA events (separated from  $\lambda$  DNA+RNAP<sub>mixture</sub>) is attributed to low glycerol content. On the other hand, the  $\lambda$  DNA +RNAP<sub>complex</sub> events histogram shows two peaks that are fitted with Gaussian distribution with the mean translocation times of 2.3 ms and 6.3 ms. This implies that when RNAP binds to  $\lambda$  DNA, most of the translocations happens faster than only  $\lambda$  DNA events and some of them are slowed down. Both  $\Delta I_B$  and  $t_{\text{dwell}}$  histograms for  $\lambda$  DNA+RNAP<sub>complex</sub> indicate two configurations in which RNAP can bind to  $\lambda$  DNA.

#### 4.3.4 Subevent Analysis

To confirm that these subevents are due to RNAP bound to  $\lambda$  DNA, we compared  $\lambda$  DNA +RNAP<sub>mixture</sub> events with  $\lambda$  DNA<sub>bare</sub> events by finding subevent start time within an event. First, two trigger levels below the base line current were chosen to separate out an event from the raw data file. We choose the third trigger of 780 pA to separate out the subevent populations within an event as shown in Fig. 4.10. A histogram of the subevent start time, ( $t_{\text{rel}}$ ), in an event is plotted next. Fig. 4.11 shows three peaks: Two sharp peaks at  $t_{\text{rel}} = 0$  and at  $t_{\text{rel}} = 0.98$  and a very broad peak centered at  $t_{\text{rel}}=0.3$  for  $\lambda$  DNA +RNAP<sub>mixture</sub>

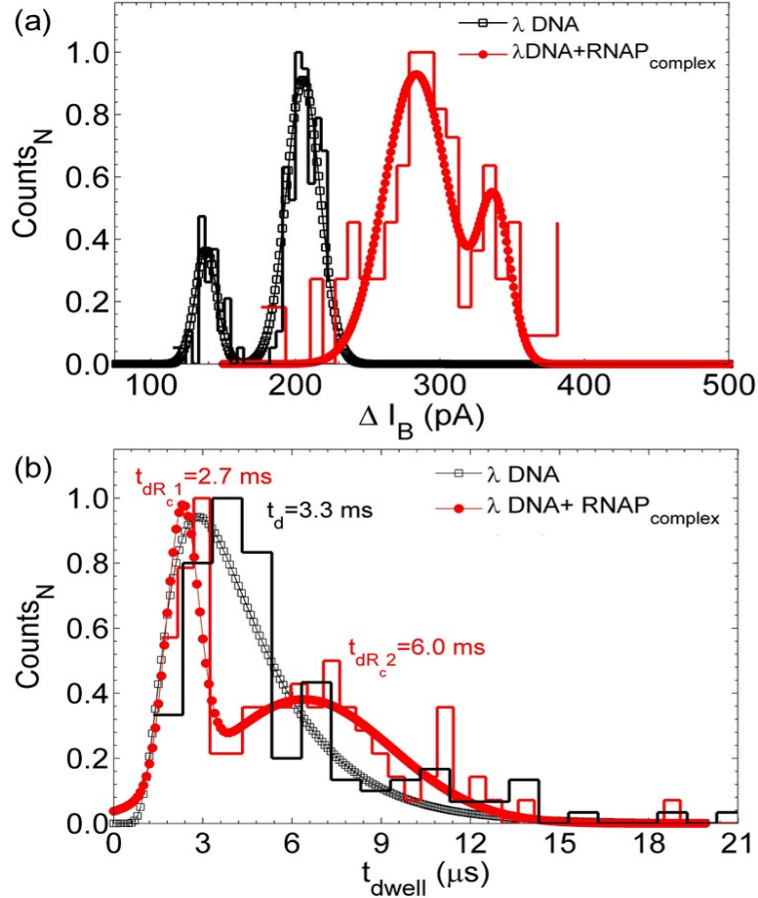


Figure 4.9: (a) Comparison between the current histograms of average current blockage for  $\lambda$  DNA (which did not bind to RNAP in a  $\lambda$  DNA+ RNAP<sub>mixture</sub>), and  $\lambda$  DNA+ RNAP<sub>complex</sub> events observed at 120 mV through a 23.7 nm by 20.4 nm nanopore . Two peaks for  $\lambda$  DNA correspond to unfolded and partially folded translocations of  $\lambda$  DNA. Histogram of  $\lambda$  DNA+RNAP<sub>complex</sub> displays two current drop peaks (b)  $t_{dwell}$  histograms of the events without a peak, and with a peak in an event are plotted together for comparison. The  $t_{dwell}$  histogram for  $\lambda$  DNA is fitted with Eq. 4.3, and is centered at 3.3 ms. On the other hand,  $t_{dwell}$  histogram of  $\lambda$  DNA+ RNAP<sub>complex</sub> depicts two peaks centered at 2.7 ms and 6.0 ms.

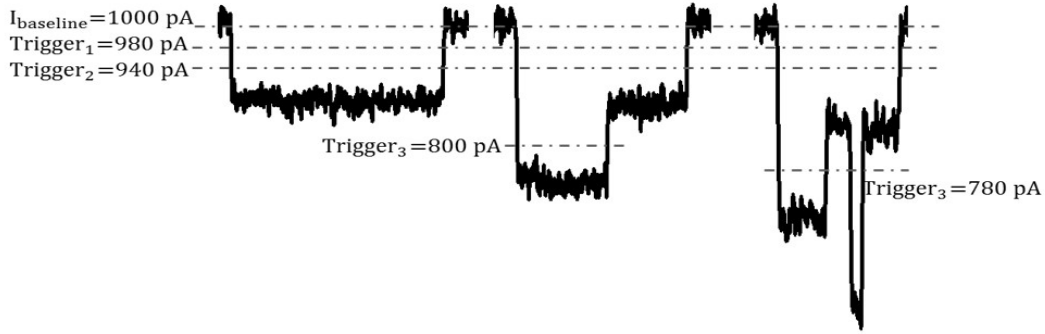


Figure 4.10: Scheme for the selection of a subevent from an event.

sample. A very small population distributed from  $t_{rel} = 0.6$  to  $0.8$  is also observed. The first peak is attributed to the folding of  $\lambda$  DNA during initial capture of the molecule by a nanopore and corresponds to the partially folded events (similar to the second event of Fig. 4.7). The other peaks are due to the presence of a protein on the  $\lambda$  DNA. To support this argument, similar analysis of subevent detection were performed with a trigger at 800 pA for bare  $\lambda$  DNA data as shown in Fig. 4.10. Trigger level of 800 pA was chosen instead of 780 pA as current blockage is smaller in case of  $\lambda$  DNA<sub>bare</sub> as compared to  $\lambda$  DNA +RNAP<sub>mixture</sub> events (as shown in Fig 4.7(b)). In contrast to  $\lambda$  DNA +RNAP<sub>mixture</sub>,  $\lambda$  DNA<sub>bare</sub> shows only a single peak at  $t_{rel} = 0$  due to folding of the DNA molecule while entering the nanopore as shown in Fig. 4.11. Counts are normalized to one for comparison in a single graph. One can argue that formaldehyde could also induce some structural changes like loops inside  $\lambda$  DNA, resulting in observations of subevents within an event. As We had observed a decrease in the current drop and an increase in dwell time of  $\lambda$  DNA<sub>formaldehyde</sub> translocation compared to  $\lambda$  DNA<sub>bare</sub> (Fig. 4.7(b) and (c)). We then, performed a subevent analysis with trigger at 800 pA on  $\lambda$  DNA<sub>formaldehyde</sub> translocation data, and Fig. 4.11 shows a single sharp peak at  $t_{rel} = 0$  and a very small population with subevent at other positions for the subevent

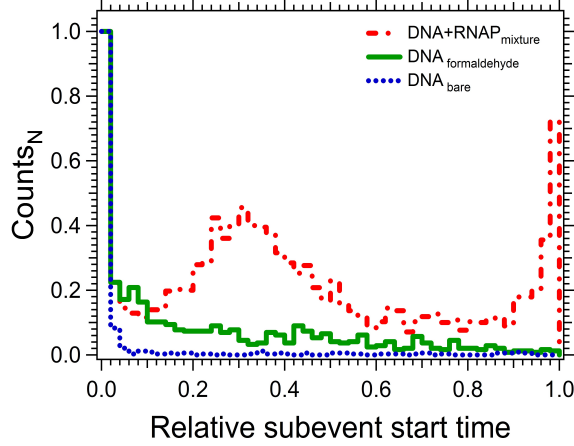


Figure 4.11: Relative subevent start time for  $\lambda$  DNA+ RNAP<sub>complex</sub>,  $\lambda$  DNA<sub>formaldehyde</sub> and  $\lambda$  DNA<sub>bare</sub> is compared. Relative subevent start time histogram for  $\lambda$  DNA+ RNAP<sub>complex</sub> shows three peaks at  $t_{rel} = 0$ ,  $t_{rel} = 0.3$  and  $t_{rel} = 0.9$ . However, relative subevent start time histogram for  $\lambda$  DNA<sub>formaldehyde</sub> and  $\lambda$  DNA<sub>bare</sub> centered at  $t_{rel} = 0$ .  $\lambda$  DNA<sub>formaldehyde</sub> has a little population at other  $t_{rel}$  values but for  $\lambda$  DNA<sub>bare</sub>, it is almost negligible.

start time histogram. All these control experiments with bare  $\lambda$  DNA and  $\lambda$  DNA<sub>formaldehyde</sub> supplement our argument that subevent population is due to the binding of the RNAP at different positions on  $\lambda$  DNA. Next, we have plotted a  $\Delta I_B$  histogram (Fig. 4.12(a)) of a RNAP current drop level within  $\lambda$  DNA+RNAP<sub>complex</sub> event and have found that RNAP level mainly centered at 432 pA or 605 pA. Two different types of current blockage levels imply that RNAP can bind in two different orientations to the DNA molecule. Next, we have shown a dwell time histogram (Fig. 4.12(b)) for RNAP subevents in  $\lambda$  DNA+RNAP<sub>complex</sub>. Dwell time for RNAP subevents is mostly around 143  $\mu$ s with a smaller population around 500  $\mu$ s.

#### 4.3.5 Relative position of RNAP on DNA

Now, we estimate the relative position,  $x_{rel}$  of RNAP on  $\lambda$  DNA. As explained earlier,  $\lambda$  DNA+RNAP<sub>complex</sub> events are mainly of three kinds (Fig. 4.8). For first type events

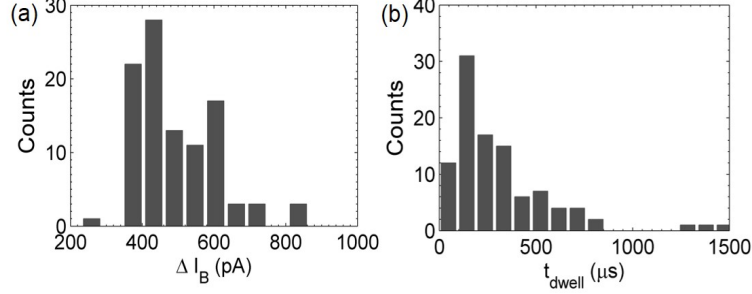


Figure 4.12: (a) Current histogram of RNAP level observed in  $\lambda$  DNA + RNAP<sub>complex</sub> event. (b)  $t_{dwell}$  histogram of RNAP subevent observed in  $\lambda$  DNA + RNAP<sub>complex</sub> event.

(Fig. 4.8(a)), we followed the same scheme as used by [126] to calculate  $x_{rel} = t_p / (t_{d1} + t_{d2})$ . Here  $t_p$ , is time from beginning of an event to the center of the RNAP subevent,  $t_{d1}$  and  $t_{d2}$  (Fig. 4.8(a)) are the time taken by unfolded DNA level before and after the RNAP subevent, respectively. Out of 101  $\lambda$  DNA+RNAP<sub>complex</sub> events, 24 events are of first kind. Figure. 4.13(a) is a  $x_{rel}$  histogram of the first kind  $\lambda$  DNA+RNAP<sub>complex</sub> events, which shows two peaks at  $x_{rel} = 0.22$  and  $0.85$ . These positions correspond to  $3.56 \mu\text{m}$  and  $14.03 \mu\text{m}$  on a  $16.5 \mu\text{m}$  long  $\lambda$  DNA molecule. To find the relative position of RNAP in the folded events like Fig. 4.8(b) and(c), we assumed that translocation speed of  $\lambda$  DNA+RNAP<sub>complex</sub> is constant through out its passage through the nanopore, so that we can double dwell time of the DNA folded level ( $t_{fd}$ ). We estimated  $x_{rel} = t_p / (2t_{fd1} + t_{d1} + t_{d2})$  and  $x_{rel} = t_p / (2(t_{fd1} + t_{d1}) + t_{d2})$  for second (Fig. 4.8(b)), and third (Fig. 4.8(c)) events respectively. The  $x_{rel}$  histograms for the second and third kind of  $\lambda$  DNA+RNAP<sub>complex</sub> events are shown in Fig. 4.13(b) and 4.13(c), respectively. The  $x_{rel}$  histogram for the second kind of events shows three peaks at  $0.25$ ,  $0.53$  and  $0.93$ , which imply the possible RNAP binding positions around  $4.07 \mu\text{m}$ ,  $8.74 \mu\text{m}$ , and  $15.40 \mu\text{m}$ . Figure 4.13(c) also depicts two binding sites for RNAP at  $1.13 \mu\text{m}$  and  $3.76 \mu\text{m}$  from the third kind of events. Recently, it has been reported with nanofluidics

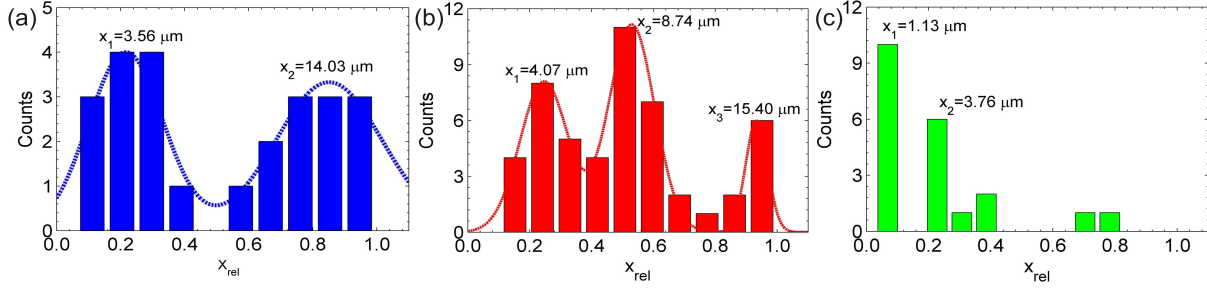


Figure 4.13: (a) Histogram of the estimated  $x_{rel}$  position from the first kind  $\lambda$  DNA+RNAP<sub>complex</sub> events. It shows two peaks around  $3.56 \mu\text{m}$  and  $14.03 \mu\text{m}$ . (b) Histogram of the estimated  $x_{rel}$  position from the second kind of events. It depicts the relative position of RNAP on  $\lambda$  DNA at  $4.07 \mu\text{m}$ ,  $8.75 \mu\text{m}$  and  $15.40 \mu\text{m}$ . (c) Estimated positions of RNAP from third type of  $\lambda$  DNA+RNAP<sub>complex</sub> events are about  $1.13 \mu\text{m}$  and  $3.76 \mu\text{m}$ .

and single molecule fluorescence experiments that along with two promoter sites of RNAP at  $3.3 \mu\text{m}$  and  $4.4 \mu\text{m}$ ,  $\lambda$  DNA has three more pseudo promoter sites between  $7 - 9 \mu\text{m}$  [115]. The first peak from Fig. 4.13(a), 4.13(b) and second peak in Fig. 4.13(b) correspond to the promoter binding sites at  $3.3 \mu\text{m}$  and  $4.4 \mu\text{m}$ . The second peak of Fig. 4.13(b) around  $8.76 \mu\text{m}$  corresponds to pseudo promoter sites. Finally, the second peak of Fig. 4.13(a), and third of Fig. 4.13(b) are attributed to the capture of  $\lambda$  DNA+RNAP<sub>complex</sub> in opposite orientation, hence RNAP level shows up at the end of an event. Or we can say that the second peak of Fig. 4.13(a), and third of Fig. 4.13(b) are equivalent to the position  $2.47 \mu\text{m}$  and  $1.1 \mu\text{m}$  respectively. These values are far away from promoter and pseudo-promoter sites. It has been observed that velocity of DNA increases towards the end of its translocation consistent with the fact that less drag forces are proposed by the DNA towards the end of an event [127]. This huge change in position is observed when DNA enters the nanopore with an opposite orientation. This could be attributed to the quick exit of the DNA at the end, as a result, temporal resolution to find a specific RNAP binding site has huge error. Also, the  $x_{rel}$  histogram of third kind of events shows a maximum number of events with  $1.13 \mu\text{m}$  as

one of the binding sites. These events are similar to the first event of Fig. 4.8(c), when DNA is captured such that RNAP level occurs within the first folded level. These kind of events suggest the wrapping of DNA around protein consistent with what has been observed with fluid tapping mode Atomic Force Microscopy experiments [128]. RNAP winds up around DNA to form open complexes before starting transcription [128].

Finally, we plotted a histogram by combining all the data sets of Fig. 4.13 with respect to DNA length. We obtained four peaks at  $x_1 = 1.04 \mu\text{m}$ ,  $x_2 = 3.83 \mu\text{m}$ ,  $x_3 = 8.00 \mu\text{m}$ , and  $x_4 = 15.74 \mu\text{m}$  as shown in Fig. 4.14. The main peak at  $3.83 \mu\text{m} \pm 1.08 \mu\text{m}$  (37243 bp  $\pm$  3180 bp), corresponds to actual promoter regions 38003 bp and 35602 bp of  $\lambda$  DNA. The width of this peak includes both promoter sites. The peak at  $8.0 \mu\text{m} \pm 5.35 \mu\text{m}$  (24985 bp  $\pm$  15726 bp) is due to pseudo promoter regions at 27649 bp, 25620 bp and 23619 bp of RNAP on  $\lambda$  DNA. The peak at  $1.04 \mu\text{m} \pm 0.5 \mu\text{m}$  (45444 bp  $\pm$  1039 bp) is a result of quick capture of DNA+RNAP<sub>complex</sub> with RNAP level in the folded part of DNA (for example first event in both Fig. 4.8(c)). The peak at  $15.72 \mu\text{m} \pm 0.5 \mu\text{m}$  (2292 bp  $\pm$  1039 bp) is due to the capture of DNA in its opposite orientation, but corresponds to the peak at  $3.83 \mu\text{m}$ . As reported earlier, DNA speeds up at the end of its journey in the nanopore [127], as a result, peak obtained at 2292 bp does not provide actual binding site (it should be at 11000 bp) with an assumption of constant translocation speed. The second major peak at  $8 \mu\text{m}$  is very broad. As pseudo promoter sites are approximately at the middle of  $\lambda$  DNA length so DNA. Temporal resolution of the nanopore sensor is not good enough to separate out individual promoter and pseudo promoter positions, but width of two main peaks includes all the possible binding sites.

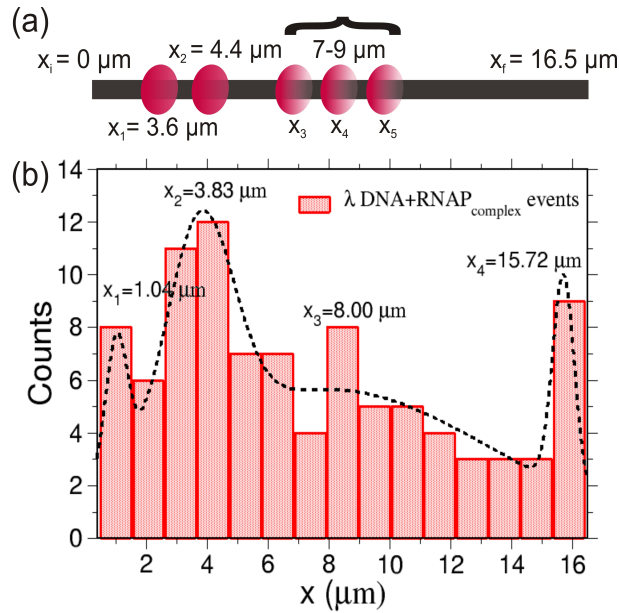


Figure 4.14: (a) A sketch for RNAP bound on five possible positions (two promoter sites:  $3.6 \mu\text{m}$  (38003 bp), and  $4.4 \mu\text{m}$  (35602 bp) and three pseudo promoter sites between  $7 - 9 \mu\text{m}$  (at about 27649 bp, 25620 bp and 23619 bp)) on a  $16.5 \mu\text{m}$  (48,502 bp) long  $\lambda$  DNA as reported previously [115]. (b) Estimated positions of RNAP bound on  $\lambda$  DNA using the solid state nanopore. RNAP has maximum tendency to bind at  $3.83 \mu\text{m}$  (37243 bp) followed by another site at  $8.00 \mu\text{m}$  (27243 bp). Another peak at  $15.74 \mu\text{m}$  (2095 bp) is due to capture of molecules in opposite orientation by nanopore and is basically counter part of 37243 bp peak. The peak at  $1.04 \mu\text{m}$  (45444 bp) is due to fast capture of RNAP with in a folded DNA level.

## 4.4 Conclusion

In conclusion, Nanopore analysis is a handy tool to study the statistics of the binding tendency of transcription factor or other proteins at different positions on long DNA molecules. We observe that in CLB buffer, the probability of RNAP molecule to bind a  $\lambda$  DNA molecule to make open complex is 42%. From the distinct current blockage signals, one can estimate the position of RNAP on a  $\lambda$  DNA molecule. Our data shows that RNAP has a high tendency to bind around 38390 bp  $\pm$ 4639 bp followed by a second site at 25920 bp  $\pm$ 3536 bp. However, these positions include two promoter regions and three pseudo promoter sites, respectively. Nanopore sensor with native setup can not distinguish between the individual RNAP binding site.

## 4.5 Materials and Methods

### 4.5.1 Nanopore Fabrication

The nanopores used for this work were fabricated using Ion Beam Sculpting (IBS) technique with diameter sizes ranging from 20 nm to 25 nm. IBS fabrication details are explained elsewhere [84]. Briefly, a 380  $\mu$ m thick silicon wafer with 275 nm Low pressure chemical vapor deposition (LPCVD) of  $\text{SiN}_x$  (low tensile, silicon rich and amorphous) on both sides, were used to fabricate a free  $\text{SiN}_x$  membrane. Next, a high energy (50 keV  $\text{Ga}^+$ ) focused ion beam (FIB) was used to drill a 100 nm hole in the free standing membrane. Then, a 3 mm\*3 mm single chip with a FIB pore was loaded into an Ion Beam Sculpting apparatus, where a 3 keV  $\text{He}^+$  ion beam was guided normally to  $\text{SiN}_x$  surface with a flux of about 1 ion/ $\text{nm}^2\text{sec}$ . Electrostatic lens systems were used to focus the ions that passed through the

FIB hole on the Channeltron style single ion detector. When ion beam strikes above the FIB hole surface, it brings out the lateral mass flow that eventually shrinks the top of the hole. As the hole size gets smaller, the number of ions passing through it also decreases. With the known initial area of FIB (measured with TEM) and assuming that nanopore area is proportional to the number of the ions passing through the hole, the beam was deflected away using LabVIEW controlled feedback system when the final size of the nanopore was achieved. Next, nanopores were annealed at 800°C for 1 hour in dry N<sub>2</sub> in a tube furnace. To measure the actual size, pores were imaged under TEM.

#### **4.5.2 Open pore Current and Current drop measurement**

Nanopores were first soaked for 15 minutes in acetone, 15 minutes in ethanol and finally stored in 20% ethanol for a few hours. The nanopore chip was then aligned between two  $\approx 40 \mu\text{l}$  chambers containing 1 M KCl, 10 mM Tris, and 1 mM EDTA at pH 8.0 solution. The salt solution was filtered with 20 nm filter and degassed at 40°C. These chambers were made up of poly-dimethyl-siloxane (PDMS) as explained elsewhere [129]. The Ag/AgCl electrodes were immersed in both the chambers. The whole system was placed in the vibration isolated Faraday cage. An Axopatch 200B and digidata 1322A combined system was used to apply the DC voltage and to measure the current across the nanopore. Signals were filtered at 10 kHz using low pass Bessel filtered and sampled at the rate of 200 kHz. All the nanopore used in this work were linearly IV characterized and have an  $I_{rms}$  below 20 pA.

### 4.5.3 Sample preparation

#### **RNAP<sub>bare</sub>**

20  $\mu\text{l}$  of 10 nM RNAP holoenzyme (New England Biolabs) in 1X CLB buffer (0.05 M HEPES  $pH = 8.0$ , 0.1 M NaCl, 5 mM MgCl<sub>2</sub> and 5% glycerol) was mixed with 20  $\mu\text{l}$  of 2M KCl having 20 mM Tris and 2mM EDTA solution at  $pH = 8$ , such that final concentration of RNAP was 5 nM with 1 M KCl and 2.5% glycerol.

#### **RNAP<sub>formaldehyde</sub>**

20  $\mu\text{l}$  of 10 nM RNAP holoenzyme in 1X CLB buffer (0.05 M HEPES  $pH = 8$ , 0.1 M NaCl, 5 mM MgCl<sub>2</sub> and 5% glycerol) was mixed with 1  $\mu\text{l}$  of 37% formaldehyde and was kept at 4°C for 30 mins. After that, 20  $\mu\text{l}$  of 2M KCl with 20 mM Tris and 2mM EDTA at  $pH = 8$  was added, so that final concentration of RNAP<sub>formaldehyde</sub> was 5 nM with 1M KCl and 2.5% glycerol.

#### **$\lambda$ DNA<sub>bare</sub>**

14  $\mu\text{l}$  of 15 nM  $\lambda$  DNA was mixed with 6  $\mu\text{l}$  of DI H<sub>2</sub>O and 2 M KCl with 10% glycerol.  $\lambda$  DNA<sub>bare</sub> concentration was 5 nM in 1 M KCl with 5% glycerol.

#### **$\lambda$ DNA<sub>formaldehyde</sub>**

20  $\mu\text{l}$  of 15 nM  $\lambda$  DNA, 6 $\mu\text{l}$  of 5X CLB (0.25 M HEPES  $pH = 8$ , 0.5 M NaCl, 25mM MgCl<sub>2</sub> and 25% glycerol), 2  $\mu\text{l}$  of formaldehyde and 2 $\mu\text{l}$  of DI H<sub>2</sub>O, mixture was kept at 4°C for 30 mintues. 20  $\mu\text{l}$  of this reaction mixture was mixed with 2 M KCl( 20 mM Tris and

2mM EDTA) with 5% glycerol at pH=8, such that the final mixture had 5 nM  $\lambda$  DNA in 1 M KCl and 5% glycerol.

### $\lambda$ DNA+RNAP *mixture*

We followed the protocol obtained by Sriram .et.al to prepare  $\lambda$  DNA and RNAP cross linked complexes. [115]. 30  $\mu$ l of reaction mixture was prepared by mixing 10  $\mu$ l of 15 nM  $\lambda$  DNA (New England Biolabs), 2  $\mu$ l of 450 nM RNAP holoenzyme (100% saturated with New England Biolabs), 6  $\mu$ l of 5X CLB buffer (0.25 M HEPES  $pH = 8$ , 0.5 M NaCl, 25 mM  $MgCl_2$  and 25% glycerol) and 12 $\mu$ l of purified DI  $H_2O$ . This reaction mixture was incubated for 15 minutes at 37°C. Finally, 2  $\mu$ l of 37% formaldehyde was added to reaction mixture at 4°C for 30 minutes. After 30 minutes, 20  $\mu$ l of the reaction mixture was mixed with 2 M KCl (20 mM Tris and 2mM EDTA) and was immediately transferred to the cis side of the nanopore system for a free translocation experiment.

## Chapter 5

### Sensing transcription factor binding sites on DNA with SSN-TFFSP apparatus

#### 5.1 Introduction

Transcription factor (TF) is an important enzyme that specifically binds on DNA and starts the transcription process to synthesize RNA from the DNA molecule. The binding of TF at a specific position on the genome is of key importance as it reveals gene regulation processes in cell life. Many theoretical models like Hidden Markov Models, Positional Weight Matrices have been proposed by computational biologists to predict transcription factor binding sites (TFBS) [130]. Many single molecule experimental approaches have also been designed to study initial interactions between TF and DNA. These techniques include AFM [113], Optical tweezers [112], nanofluidics combined with fluorescence microscopy [115–118] and nanopore sensors [126, 131].

Nanopore detection of TF, Zinc finger(Zif268) binding sites has been demonstrated recently [126]. Depending upon the current blockage peaks, specificity of binding has been predicted. Another report has discussed binding position of antibody on  $\lambda$  DNA using nanopore sensors [131]. Likewise in Chapter 3, we have discussed the binding efficiency and an estimation of RNAP binding sites on  $\lambda$  DNA molecules. As discussed previously, it is difficult to identify exact binding sites using traditional nanopore set up as DNA accelerates towards the end of its exit from a nanopore and also can enter pore in any possible orientation. In this chapter, we demonstrate mapping of binding sites of RNAP holoenzyme of  $\lambda$  DNA molecule using SSN-TFFSP system. We have discussed the advantages of SSN-TFFSP system over native nanopore set up to control the translocation speed of DNA while passing

through nanopore and orientation of complex capture is fixed, as it depends on the design of the molecule. The slow translocation rate  $> 100 \mu\text{s}$  per base obtained with SSN-TFFSP [47] could provide enough resolution to detect individual binding sites with high accuracy. We will discuss the capture of DNA and RNAP complex and trapping of single RNAP inside the nanopore. To explore the dynamics of RNAP inside the nanopore, we study the current power spectral density. Finally, we show resolution limit of SSN-TFFSP system to sense binding sites of RNAP on  $\lambda$  DNA and compare it with the other techniques.

## 5.2 Experimental Setup

The experimental setup of SSN-TFFSP apparatus is discussed extensively in Chapter 2. Briefly, a biotin labeled oligomer was first ligated to one end of  $\lambda$  DNA and then  $\lambda$  DNA+RNAP complex was prepared as explained in the preparation section of Chapter 4. Finally, the DNA-protein complex was attached to a probe tip via streptavidin-biotin interaction as explained in Chapter 3. The DNA-protein complex tethered tip was brought above the cis side of nanopore set up and was immersed in 1 M KCl salt solution. The tip was aligned above the nanopore membrane and moved down. Once tip approaches near the nanopore surface, the electric field across the nanopore captures the complex molecule. A schematic of the experimental set up is shown in Fig. 5.1.

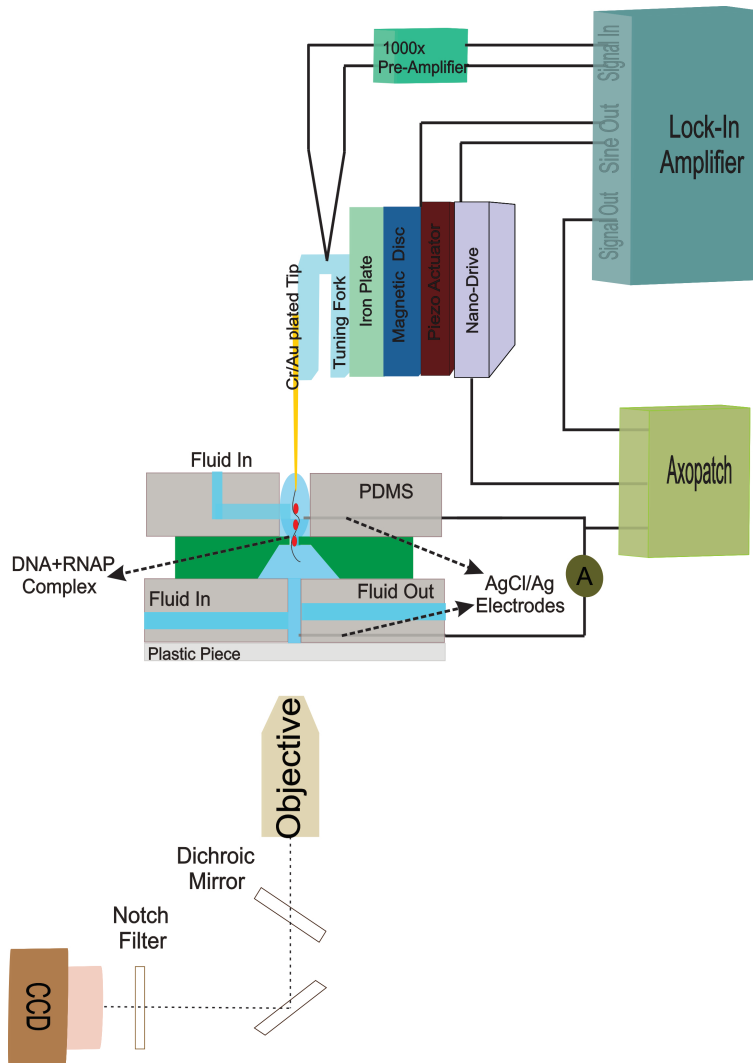


Figure 5.1: A schematic drawing for the experimental setup of a controlled translocation of  $\lambda$  DNA+RNAP<sub>complex</sub> with SSN-TFFSP apparatus. SSN is aligned between PDMS fluidic chambers, and  $\lambda$  DNA+RNAP<sub>complex</sub> are tethered to tip. Tip with complex molecules is brought inside the cis chamber. The DNA-tethered tip is attached to a tuning fork. The tuning fork is connected to a piezo actuator to excite the tuning fork at its resonance frequency. The tuning fork setup is connected to a nanopositioner for the positional control of tip. A lock-in amplifier is connected to the piezo actuator for excitation and a pre amplifier is used to amplify the signal 1000 times. The output signal of tuning fork after amplification is observed with the lock-in amplifier. Objective lens and CCD camera are located under the fluidic chambers for the tip and nanopore alignment.

## 5.3 Results and Discussion

### 5.3.1 Mapping RNAP position on $\lambda$ DNA

Similar to the results described in Chapter 2, Fig. 5.2 shows three signals: Ionic current from solid state nanopore of size 17 nm $\times$ 21 nm with 1M KCl at 120 mV, z position of tip above the nanopore and vibrational signal from tuning fork force sensing probe tip recorded simultaneously using an Axopatch system with a sampling frequency of 50 kHz . Initially, we observed an open pore current of 11.3 nA at 120 mV from this nanopore. Later on, the ionic current has increased to 16 nA at 120 mV and is attributed to an increase in size of the nanopore over time which has been characterized well previously [132]. This final open pore current corresponds to a nanopore of diameter 26 nm approximately. At  $t=0$  s, tip is 32.40  $\mu\text{m}$  away from SiN membrane and is moved downward. When tip is about 1.76  $\mu\text{m}$  above the nanopore a drop of 229 pA in ionic current is observed, as tip is moved further down current decreases with multiple levels. When tip touches the membrane (corresponds to vertical line (II)) vibrational amplitude of probe tip decreases sharply as shown in Fig. 5.2(c) and is used as a feedback to stop further downward movement of tip. When tip has approached SiN membrane, a final current drop of 1428 pA is recorded. When current level has become stable after multiple drops, tip is lifted up slowly with a step of 50 nm and the current level started increasing. Interestingly, when tip is lifted to about 6.9  $\mu\text{m}$  another drop of 250 pA in the current signal is observed. When tip is lifted up to 15.9  $\mu\text{m}$  away, DNA molecules are completely released from the nanopore and the ionic current has obtained its value close to initial  $I_o$ .

As discussed in Chapter 2, when a single  $\lambda$  DNA molecule was trapped inside the nanopore

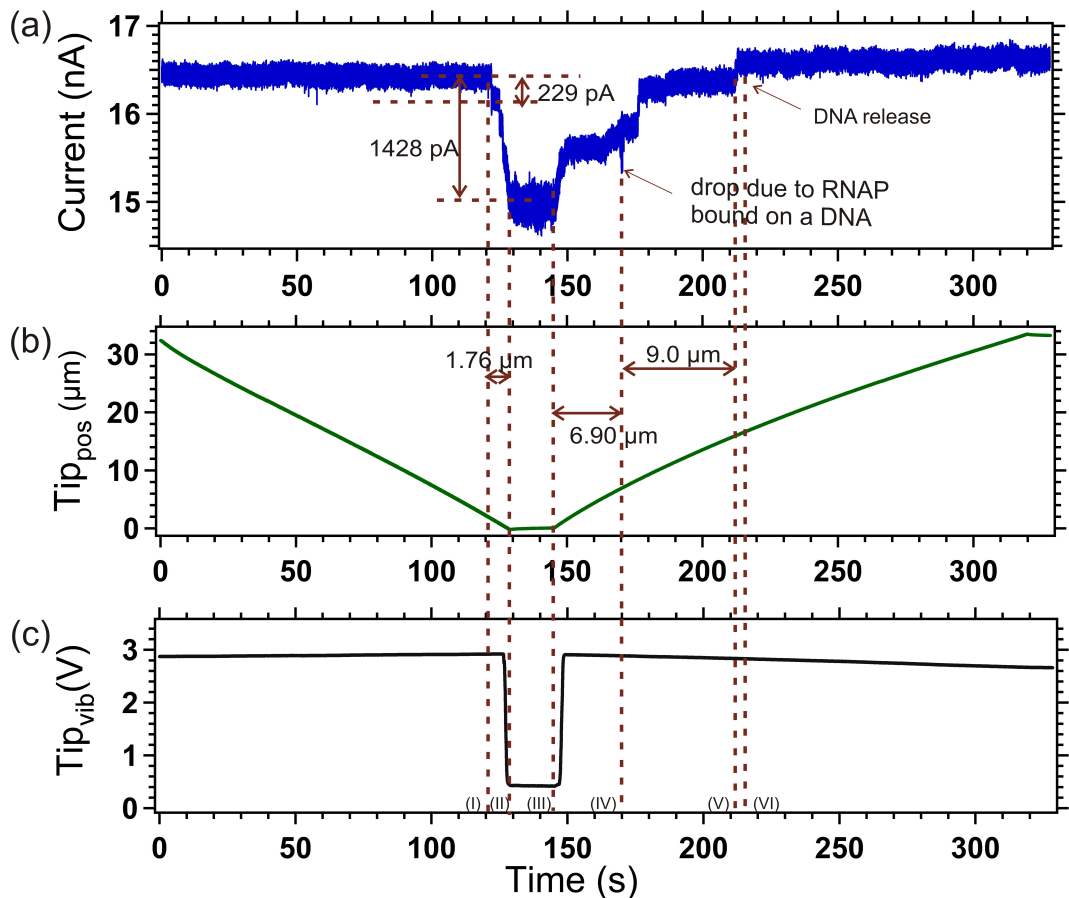


Figure 5.2: (a) Current measured from 17 nm by 21 nm pore at 120 mV with 1 M KCl, (b) vertical position of the tip, and (c) vibration signal from the tip attached to a tuning fork versus time measured simultaneously by the Axopatch, when the tip is approaching or being lifted from nanopore. A bundle of molecules are trapped inside the pore. A current drop of  $\approx 250$  pA is observed at about  $6.9 \mu\text{m}$  while lifting the tip. When tip is at  $15.9 \mu\text{m}$  away from nanopore, DNA are completely out of nanopore's electric field.

or pulled out of nanopore a drop of  $\approx 60$  pA was observed at 60 mV of applied voltage. During this experiment, when the tip is brought down at 60 mV voltage across the nanopore a current drop of 119 pA is observed at  $1.2 \mu\text{m}$  away from the nanopore membrane (Fig. 5.3). When the tip is close to the membrane at (II) vibrational amplitude drops (Fig. 5.3(c)) and further movement of the tip is ceased. At this point, current drop has reached to a value of 299 pA. When the tip has started moving up from (III) current drop has reduced to 119 pA and it is constant up to  $9.0 \mu\text{m}$ . Finally, DNA exits with a current recovery step of 43 pA and ionic current reaches its original value. A current drop of 119 pA suggests trapping of two DNA molecules as a single trapped DNA results in a  $\approx 60$  pA drop. A drop of 299 pA between (II) and (III) corresponds to 5 DNA captured by the nanopore. DNA release step of 43 pA also advocates the presence of two DNA molecules because current recovery steps predicted from COMSOL simulation (as shown in Chapter 2) also has a value of  $\approx 25$  pA. The contour length of  $\lambda$  DNA is  $16.5 \mu\text{m}$  so current drop level should persist until tip is lifted about  $16 \mu\text{m}$  as observed in Fig 2.8 but we observe a drop of 119 pA for  $9.0 \mu\text{m}$  only. This suggests that either the tip is away from the nanopore such that full  $\lambda$  DNA length is not captured or DNA is not stretched completely by the electric field across the nanopore or DNA molecule is not attached at the end of the tip.

Next, we explain traces obtained at 120 mV (Fig. 5.2(a)) at different tip positions in detail as shown in Fig. 5.4. According to 60 mV data, one should expect double current drop of about 120 pA at 120 mV with a single molecule captured inside the pore. In this case when the tip is close to the membrane, we observed initial current drop of 229 pA followed by multiple current drop levels with a final value of 1428 pA. This current value suggests capture of two DNA in the beginning followed by capture of 10 more DNA molecules compared to the

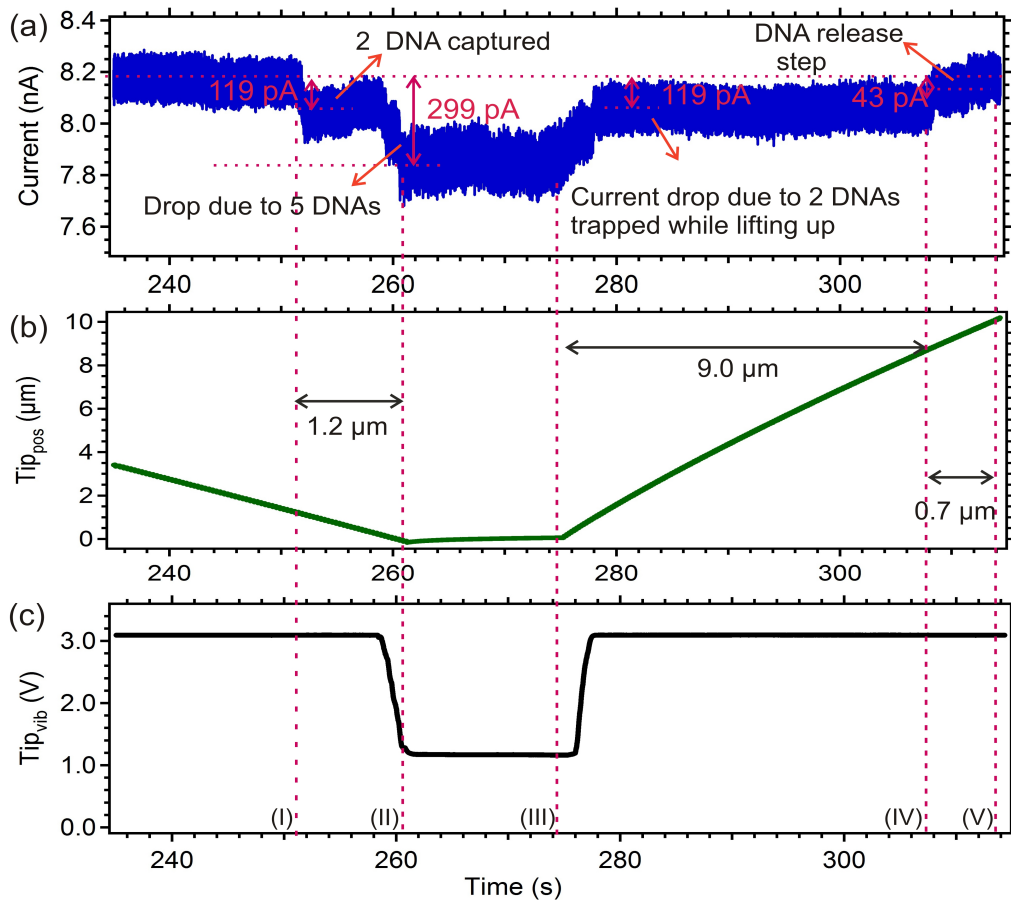


Figure 5.3: (a) Current measured from 17 nm by 21 nm pore at 60 mV with 1 M KCl, (b) vertical position of tip, and (c) vibration signal from tip attached to tuning fork versus time measured simultaneously by Axopatch when tip is approaching or being lifted from nanopore. While tip is moving down a current drop of 119 pA is observed at 1.2  $\mu\text{m}$  away from membrane. This drop of 119 pA is constant until the tip has lifted to 9.0  $\mu\text{m}$  above the membrane.

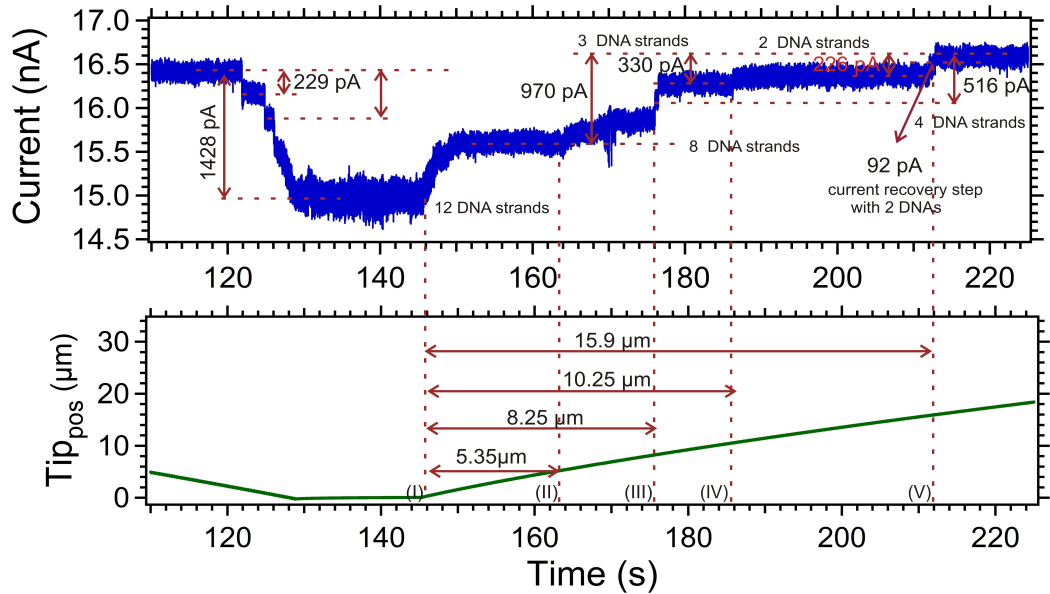


Figure 5.4: (a) Current measured from a 17 nm by 21 nm pore at 120 mV with 1 M KCl, and (b) vertical position of the tip versus time measured simultaneously by an Axopatch, when tip is approaching or being lifted from nanopore. A bundle of molecules are trapped inside the pore. While lifting up the tip a drop at about  $6.9 \mu\text{m}$  is observed. When tip is at  $15.9 \mu\text{m}$  away from nanopore, DNA are completely out of the nanopore electric field.

60 mV case (Fig. 5.3) and is due to larger force experienced by DNA at 120 mV. While pulling up tip, we observed several current recovery steps depending upon the capture of DNA molecules from different lengths. When tip is lifted up  $5.35 \mu\text{m}$  current drop has decreased to 970 pA reflecting 8 DNA molecules left inside. When the tip has reached  $8.25 \mu\text{m}$  above the nanopore, current drop has a value of 516 pA leaving 4 DNA inside the pore. At  $10.25 \mu\text{m}$ , only two DNA are left inside the nanopore. The current blockage due to 2 DNA persists up to  $15.9 \mu\text{m}$  which is equivalent to the length of the  $\lambda$  DNA molecule. Finally, current recovery step of 92 pA is observed, which is consistent with twice the value of the current recovery step observed at 60 mV shown in Fig. 5.3. The current drop observed at  $\approx 6.9 \mu\text{m}$  in Fig. 5.2(a) has reoccurred several times when tip was brought in and lifted out. Next figure (Fig. 5.5) shows ionic current signal (Fig. 5.5(a), (b), and (c))

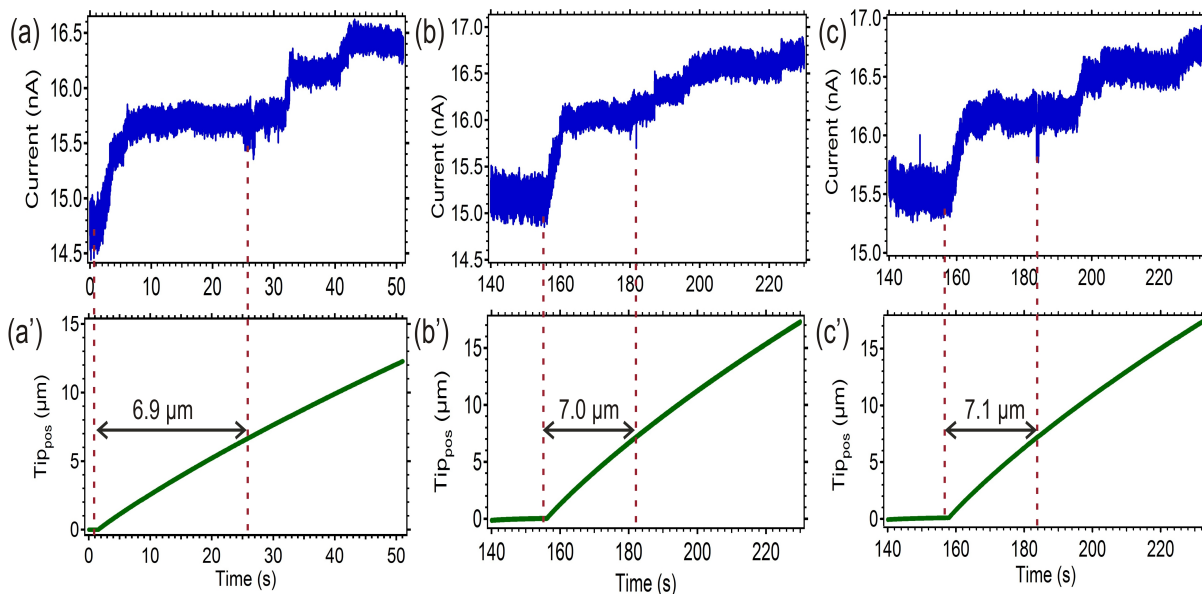


Figure 5.5: (a) Current blockage signal, and (a') position of the tip, when first tip is being lifted up. (b) Current blockage signal, and (b') position of the tip, where same tip is lifted up second time. (c) Current blockage signal and (c') position of the same tip, while it is being pulled out for third time. All the traces show a unique current drop of 250 pA at  $\approx 7 \mu\text{m}$ .

and corresponding position of tip while being pulled out (Fig. 5.5(a'), (b'), and (c')) for three consecutive approaches above the same pore. In all the current traces, we observed a unique current drop when tip has lifted up to  $\approx 7 \mu\text{m}$  above the nanopore membrane. This current drop is due to RNAP bound on one of  $\lambda$  DNA trapped inside the nanopore. As discussed in Chapter 4, RNAP can bind on five different positions (two promoter sites  $3.6 \mu\text{m}$ ,  $4.4 \mu\text{m}$  and three pseudo promoter sites between  $(7 - 9 \mu\text{m})$ ) on the  $\lambda$  DNA molecule [115]. Hence, current drop at about  $7 \mu\text{m}$  reflects RNAP bound to one of the pseudo promoter sites.

We performed another experiment with  $\lambda$  DNA and RNAP complex molecules attached to tip and with a nanopore of diameter  $24.5 \text{ nm}$ . The nanopore used for this experiment are of different geometry, nanopore fabrication process is discussed here [133]. This nanopore has a  $\approx 2 - 5 \mu\text{m}$  opening circle milled by Focused Ion Beam on the top surface followed by

1  $\mu\text{m}$  long cavity created by etching  $\text{SiO}_2$  and finally TEM nanopore was drilled in 20 nm thin SiN membrane at the bottom. These nanopores were observed to give a current drop of 200 pA at 100 mV with free  $\lambda$  DNA translocation [125, 133]. Figure 5.6(a) shows the current signal when DNA and protein complex is captured initially and tip is close to the membrane at (I) and amplitude of tip vibration is at the minimum (Fig. 5.6(c)). Once the molecule is captured completely tip is lifted up from (II), current drop value has decreased from 500 pA to 250 pA as shown in Fig. 5.6(b) and is constant until tip is lifted to 19.5  $\mu\text{m}$  close to the contour length of  $\lambda$  DNA. We observed a current recovery step of 43 pA before DNA exits from the nanopore electric field effect. As reported previously, during the  $\lambda$  DNA translocation through this type of nanopore, a current blockage of 250 pA is expected from a single  $\lambda$  DNA molecule at 120 mV. Similar to Fig. 5.2, we again observed two distinct current drops of  $\approx 150$  pA when tip is at 3.6  $\mu\text{m}$  and 4.5  $\mu\text{m}$  above the nanopore membrane as shown in Fig. 5.6. These positions are consistent with two promoter sites of RNAP on  $\lambda$  DNA.

### 5.3.2 Current Fluctuations while trapping

Along with a drop in current at  $\approx 7$   $\mu\text{m}$  in Fig. 5.2(a) while lifting up tip, we have also observed fluctuations in current signal. These current fluctuations were measured when a molecule is trapped inside the nanopore, and can describe information about dynamics of protein bound to DNA inside the nanopore. Zoomed in view of current drop signal at 6.9  $\mu\text{m}$  in Fig. 5.2(a) and at 3.6  $\mu\text{m}$  and 4.5  $\mu\text{m}$  in Fig. 5.6(a) are shown in Fig. 5.7(a), (b), and (c) respectively. Figure 5.7(a'), (b'), and (c') show the corresponding position of the tip when protein is near the nanopore. It is evident from Fig. 5.7(a) and (a') that these

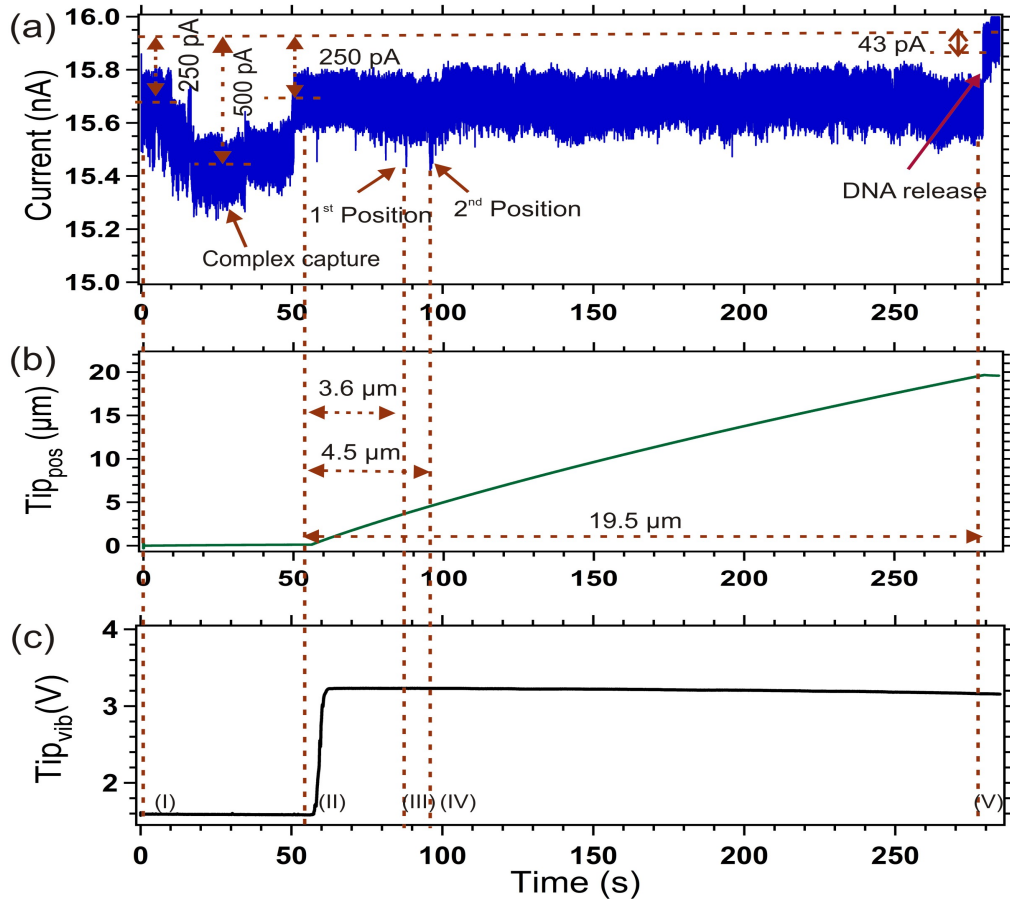


Figure 5.6: (a) Current measured from a 25 nm by 24 nm pore at 120 mV with 1 M KCl, (b) vertical position of the tip, and (c) vibration signal from the tip attached to a tuning fork versus time measured simultaneously by an Axopatch, starting with tip being close to nanopore membrane for 50 s and is being lifted afterwards. At 120 mV, DNA+ RNAP<sub>complex</sub> is trapped by nanopore when the tip is standing above the nanopore as a result current drop up to 500 pA occurs. When we start lifting up the tip, two current drops at 3.6  $\mu\text{m}$  and 4.5  $\mu\text{m}$  are observed. When the tip has lifted to 19.5  $\mu\text{m}$  above from nanopore, DNA is released from the nanopore completely and current gets back to its original value.

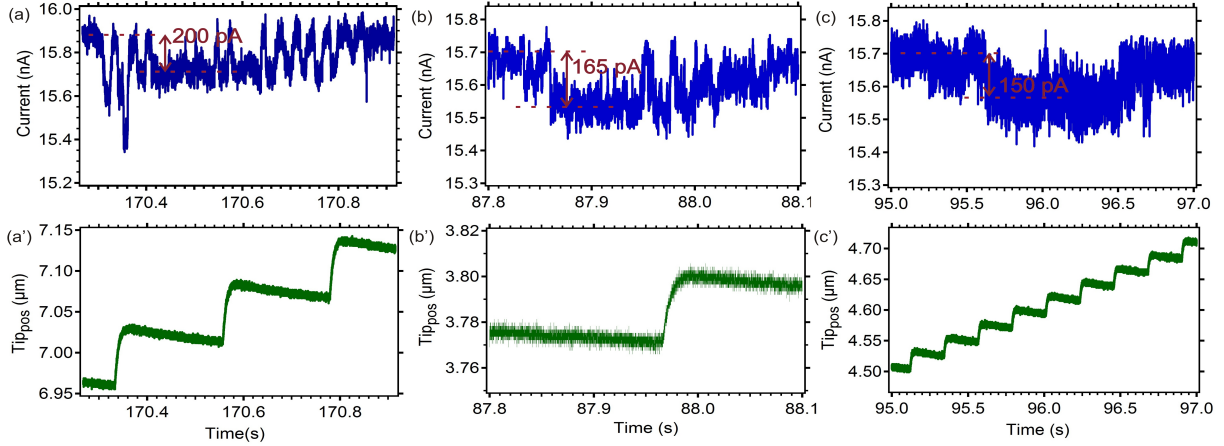


Figure 5.7: (a) Zoomed in view of current blockage signal observed at  $6.9 \mu\text{m}$  shown in Fig. 5.2(a) while pulling the DNA+RNAP<sub>complex</sub> from the nanopore. (a') Corresponding vertical position of the tip while moving up. (b) Zoomed in view of current drop signal observed at  $3.6 \mu\text{m}$  in Fig. 5.6(a) while pulling out DNA+RNAP<sub>complex</sub> attached to tip. (b') Vertical position of tip relative to current signal plotted in (b). (c) and (c') are the zoomed in view of the current signal and position of the tip for the current drop seen at  $4.5 \mu\text{m}$  in Fig. 5.6(a).

current fluctuations caused by protein last for  $150 \text{ nm}$  (three upward steps of tip) while moving the tip away from the pore. Similarly current fluctuations shown in Fig. 5.7(b) and (c) were observed for the tip movement of  $25 \text{ nm}$ , and  $125 \text{ nm}$  respectively. The possible cause of current variations in Fig. 5.7(a) and (b) could be the vibration of RNAP bound on DNA molecule. However, variation in current block shown in Fig. 5.7(c) could be due to interactions between RNAP and pore walls or different binding orientation of RNAP on DNA, as a result we observe a broad current blockage instead of short square pulse type fluctuations observed in Fig. 5.7(a) and (b). In past, ionic current fluctuations were studied to explain permeation of sugar [134, 135], ATP [136] and antibiotic [137] molecules through biological pores. Protonation kinetics in an open  $\alpha$  toxin protein have been revealed through current noise measurements [138]. To explore these fluctuations in a better way, we need to understand the statistical fluctuations or noise observed in the nanopore current

measurements and sources that contribute to these fluctuations.

### 5.3.3 Noise observed in Solid state nanopores

Current noise in solid state and graphene nanopores is explained very well previously [129, 139, 140]. Current noise measured in nanopores is characterized by examining the current power spectral density (PSD) of the measured current signal. PSD is a measure of power intensity of a signal in the frequency domain and is calculated from the Fourier transform of measured signal. To define it more specifically, let us assume  $I(t_n)$  measurement of the current signal made at discrete time intervals  $t_n$  (where  $n=0,1,2\dots N-1$ ) with a step size  $\delta t$ . Total time interval over which data is measured is defined by  $T$ , where  $T=N\delta t$ . The discrete Fourier transform of the current signal can be calculated by using the following equation,

$$I(f_k) = \sum_{n=0}^{N-1} I(t_n) e^{-i2\pi f_k n \delta t} \delta t \quad (5.1)$$

where  $k = 0, 1, 2, \dots, N - 1$  denote discrete frequency space intervals. Power spectral density of  $I(t_n)$  denoted by  $S_I(f_k)$  is defined as

$$S_I(f_k) = \frac{2}{T} |I(f_k)|^2 \quad (5.2)$$

PSD of a current trace measured from 17 nm by 21 nm pore at 120 mV with 1 M KCl salt solution is plotted in Fig. 5.8 and is estimated by dividing the data set  $I(t_n)$  into adjacent segments and calculated PSD for each segment, which are averaged together. It is shown earlier that high frequency current power spectral density is described well by the Johnson Noise of the electrical circuit of nanopore combined with the Axopatch system and low frequency regime has shown to have  $1/f$  noise behavior [139].

### 5.3.4 Johnson Noise or Thermal Noise

Johnson Noise is an electric noise due to thermal commotion of charge carriers inside a conductor at equilibrium [141]. It was measured first by John B. Johnson in 1928 [141] and was explained by Nyquist [142]. Johnson observed that voltage noise for any resistor is proportional to temperature and resistance [141]. For electrical circuits involving RC network voltage noise can be related to net Impedance ( $Z$ ) or admittance ( $Y$ ) of the circuit. The voltage power spectral density ( $S_V$ ) from Johnson Noise is given by [143],

$$S_V = 4k_B T \operatorname{Re}\left(\frac{1}{Y}\right) \quad (5.3)$$

where  $k_B$  is the Boltzmann constant,  $T$  is the temperature and  $Y$  is the admittance of the circuit. Finally, the current power spectral density can be written as [143],

$$S_I = |Y|^2 S_V \quad (5.4)$$

The current power spectral density can be calculated from nanopore admittance. The nanopore in a thin membrane is equivalent to a capacitor ( $C_m$ ) in parallel with resistance of the pore  $R_p$  [144]. Non ideal behavior of the nanopore capacitance has been shown to have an impact on measured noise during nanopore experiments [139] and can be modeled by taking into account an admittance in parallel with nanopore capacitance as shown in Fig. 5.8(a) and is given by the equation,

$$Y_{loss} = \omega C_p D = \omega C_m \tan \delta \quad (5.5)$$

where  $D$  is the dielectric loss and is equivalent to tangent of dissipation factor. This RC circuit is in series with resistance,  $R_\infty$ , a resistance between the nanopore and electrodes.

For circuit shown in Fig. 5.8(a), the net admittance is given by

$$Y = \frac{1}{R_\infty + \frac{1}{\frac{1}{R_p + i\omega C_m + \omega C_p \tan \delta}}} \quad (5.6)$$

The value of  $R_p$  is measured from the slope of IV curve of a nanopore. An example of IV curve for 17 nm by 21 nm nanopore is shown in Fig. 5.8(b) with a slope of 81.82 nS and hence  $R_p = 12 \text{ M}\Omega$ . Smeets. et. al estimated the value of  $C_m$  and  $R_\infty$  by observing the current response at 40 mV voltage jump with a membrane without a nanopore inside it [139]. The loss tangent value is reported to 0.27 for  $\text{SiN}_x/\text{SiO}_2$  membranes with nanopore [139]. We estimated  $C_p = 256 \text{ pF}$  with  $R_\infty = 35 \text{ k}\Omega$ . Using these values, current power spectral density calculated from Johnson Noise is plotted against frequency in Fig 5.8(c) on top of the measured current PSD form 17 nm  $\times$  21 nm. It is clear from Fig. 5.8(c) that Johnson Noise of nanopore circuit contributes in higher frequency range 400 Hz–10 kHz. Johnson Noise from RC feedback circuit and resistance of operational amplifier used in the Axopatch 200B system is also shown to have contribution in the higher frequency range [139].

### 5.3.5 1/f Noise

Low frequency current power spectral density observed in nanopore open current cannot be described by Johnson Noise. In earlier reports, low frequency fluctuations observed in nanopore current signal are modeled by 1/f noise [139, 145–149]. 1/f noise is generally referred to noise whose power spectral density is of the form  $S \propto 1/f^\alpha$  where  $0 < \alpha < 2$ . Smeets.et.al used phenomenological relation for low frequency proposed by Hooge [139]. According to Hooge's experimental work PSD is inversely proportional to the number of

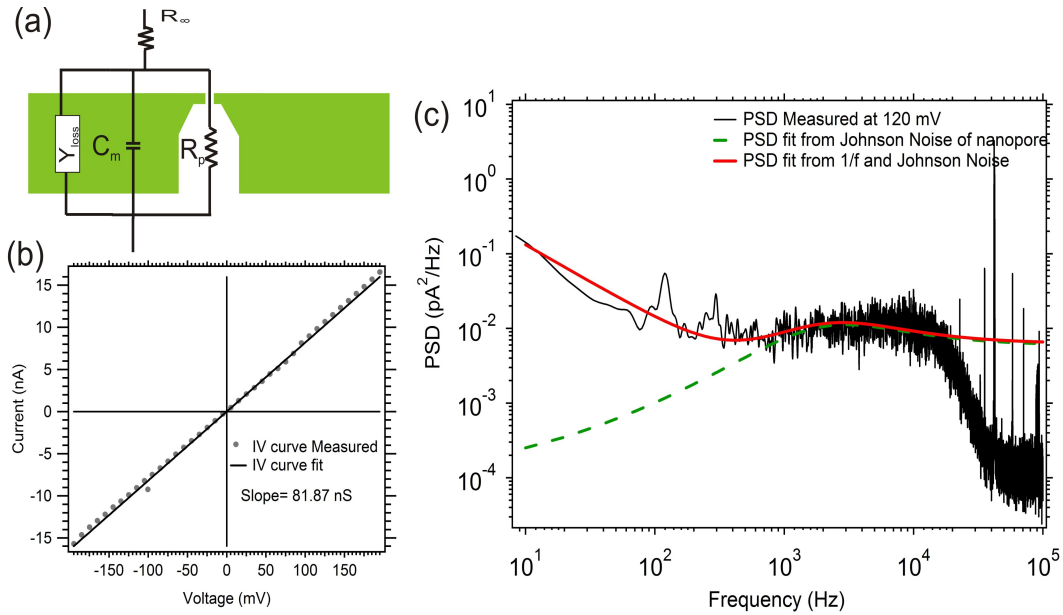


Figure 5.8: (a) An equivalent RC circuit for a nanopore.  $R_p$  is the resistance of nanopore is  $\approx 10 \text{ M}\Omega$ ,  $C_m$  is capacitance of SiN membrane is typically  $> 10 \text{ pF}$  and  $R_\infty$  access resistance away from pore is of the order of  $10 \text{ k}\Omega$ . (b) Current voltage characteristics of a  $17 \text{ nm}$  by  $21 \text{ nm}$  nanopore. Nanopore shows a linear I-V dependence and a straight line fit gives a slope of  $81.87 \text{ nS}$  (c) A plot between current Power Spectral Density (PSD) versus frequency for a open pore current signal from a nanopore of dimension  $17 \text{ nm}$  by  $21 \text{ nm}$ . A theoretical estimation of PSD calculated from Johnson Noise of the nanopore RC circuit (dotted line) and total theoretical estimation of power spectrum calculated by combining  $1/f$  noise and Johnson Noise (solid line) is plotted on top.

charge carriers,  $N_c$  and can be written as [139, 150],

$$S_I = \frac{I^2 \alpha}{N_c f} \quad (5.7)$$

where  $I$  is the current measured through the nanopore,  $\alpha$  is called Hooge's parameter. We fit current PSD region below 400 Hz with Eq. 5.7 with  $I = 10287$  pA  $N_c = 2.5 \times 10^4$  and obtained value of Hooge's parameter  $\alpha = 3 \times 10^{-4}$ , is of same order as reported earlier [139]. Next, we plotted the combined current PSD calculated from Johnson Noise of nanopore and 1/f Hooge's noise as shown in Fig. 5.8(b) (red solid line). These combined current power spectral densities describe well measured current PSD from nanopore up to 10 kHz and noise at higher frequencies is attributed to Johnson noise of amplifier configuration. As we will see next, to explain current fluctuations measured during protein capture (as described in previous section) we need to focus only on low frequency current fluctuations or 1/f noise. So, we can ignore the variation on the higher frequencies end.

### 5.3.6 Comparison between current PSD

As we have discussed in the previous section, some level of current fluctuations or noise is always observed from solid state nanopores even when no molecules are added. Now we compared this PSD signal with DNA blockage signal for free translocation data. We observed that current power spectral densities for current signal ( $I_o$ ) when no DNA is present and when DNA is passing through ( $I_B$ ) overlap on each other as shown in Fig. 5.9 (a). Similarly, in Fig. 5.9 (b), we compared current PSD when a RNAP is trapped inside the pore during free translocation of  $\lambda$  DNA+RNAP<sub>complex</sub> through 17 nm  $\times$  21 nm pore with no other molecule inside. In contrast to DNA trapped PSD (Fig. 5.9(a)) we observed that

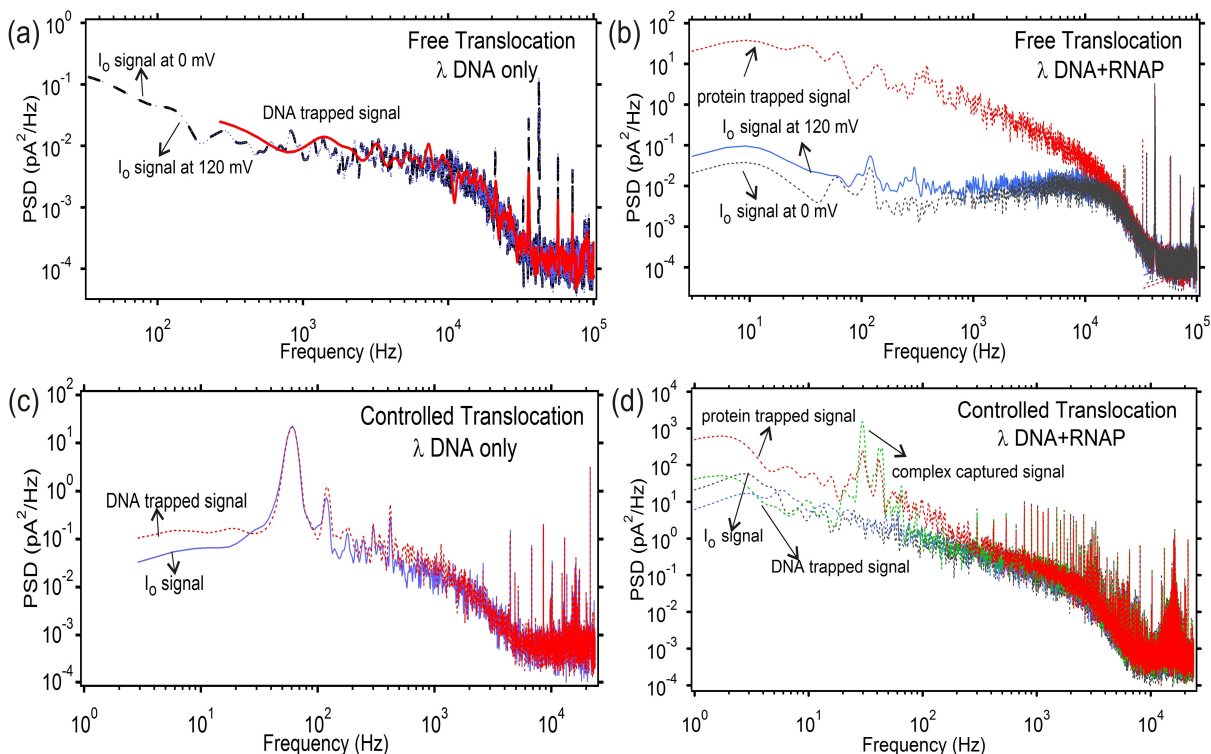


Figure 5.9: (a) Current power spectral densities are plotted for the current signal measured from a  $17.5 \text{ nm} \times 19 \text{ nm}$  nanopore for three different situations: with no external voltage, at 120 mV applied voltage and during the free translocation of  $\lambda$  DNA through nanopore. (b) Current power spectral densities are plotted from a  $17.5 \text{ nm} \times 21 \text{ nm}$  nanopore current measurements for three situations: with no bias voltage, at 120 mV applied voltage and when a RNAP molecule is trapped during the free translocation of  $\lambda$  DNA+RNAP through nanopore. (c) Current power spectral densities are plotted for the current signal when tip is far away from membrane (Fig. 2.8), and when the DNA is inside the nanopore and is being lifted up with tip (corresponding to the signal between (III) and (IV) in Fig. 2.8). (d) Current power spectral densities are plotted for the current measurements: when tip is far away from the nanopore (which corresponds to the region before 50 s in Fig. 5.2(a)), when the complex is captured by a nanopore (for current signal between (II) and (III) in Fig. 5.2), when DNA is inside the nanopore (while tip is being lifted up, for a region between (IV) and (V) of Fig. 5.2), and when a RNAP bound to a DNA is trapped inside corresponds to point (IV) in Fig. 5.2.

PSD for RNAP trapped signal is  $\approx 10^3$  times (in the low frequency region) higher than  $I_o$  signal. In other words,  $1/f$  noise deviates from the original signal's  $1/f$  noise. When RNAP is trapped inside the pore, the number of the charge carries,  $N_c$  inside the pores also decreases, as a result, one may expect  $1/f$  noise to increase in accordance with Eq. 5.7. But as  $N_c$  decreases the observed current  $I$  through the pore will also decrease, hence a change in  $N_c$  is balanced in Eq. 5.7. So this huge increase in the  $1/f$  noise can be attributed to the interactions between RNAP and pore walls such that the molecule vibrates inside the pore, and the applied electric force may not be strong enough to overtake dynamic motion of RNAP inside nanopore.

Next, we draw a comparison between current power spectral densities for controlled translocation of  $\lambda$  DNA and  $\lambda$  DNA+RNAP<sub>complex</sub> through the nanopore using tuning force sensing probe tip. Figure 5.9(c) shows PSD analysis for current signal when tip is far away (signal before 20 seconds Fig. 2.8(a)) and for the current signal measured when  $\lambda$  DNA is inside nanopore, which is being lifted up with the force sensing probe tip (current signal between (III) and (IV) of Fig. 2.8). It is evident from Fig. 5.9(c)  $1/f$  noise for both situations (with DNA and without DNA) is almost the same, similar to the free translocation case Fig. 5.9(a) except for a distinct peak observed at 60 Hz. This 60 Hz is due to poor isolation of surrounding electrical signals by Faraday Cage. Finally, we compare in Fig. 5.9(d) power spectral densities for current measured from 17.5 nm $\times$ 21.0 nm nanopore at 120 mV, during controlled translocation of  $\lambda$  DNA+ RNAP<sub>complex</sub> at different positions of the tip. These four different positions of the tip are: when tip is 35  $\mu$ m away from the membrane,  $I_o$  (corresponds to signal before 50 s in Fig. 5.2(a)), when DNA is trapped (for current signal between (IV) and (V) in Fig. 5.2), when the complex is initially captured by nanopore (for current signal

between (II) and (III) in Fig. 5.2), and when a single RNAP bound to DNA is trapped inside nanopore (corresponds to point (IV), where tip is at  $7 \mu\text{m}$  above the nanopore). Power Spectral densities signals calculated at these positions of tip are plotted in Fig. 5.2. Power spectral densities measured from  $I_o$ , and DNA trapped current signal are almost the same, on the other hand, PSD for current signals when complex is initially captured by nanopore, and when RNAP bound to DNA is trapped inside the nanopore, have two sharp peaks at 29 Hz and 41 Hz.  $1/f$  noise of the protein trapped current signal (when the tip is at  $7 \mu\text{m}$  in Fig. 5.2) is  $\approx 10^2$  times larger than initial current signal,  $I_o$ .

Next, we discuss the current fluctuations observed during DNA+RNAP complex capture, protein trapped at  $3.6 \mu\text{m}$  and DNA trapped (between (IV) and (V)) current signal observed in case of  $25 \text{ nm} \times 24 \text{ nm}$  pore shown in Fig. 5.6. Zoomed in view of DNA+RNAP<sub>complex</sub> capture by the nanopore is shown in Fig. 5.10(a). It is evident from Fig. 5.10(b) that when DNA+RNAP<sub>complex</sub> is released by the nanopore, current fluctuations which appeared during the complex capture (Fig. 5.10(a)) are not observed anymore. In Fig. 5.10(c), we plot PSD for various current signals when the tip is near the nanopore membrane corresponding to complex capture in Fig. 5.10(a), DNA trapped signal,  $I_o$  signal in Fig. 5.10(b) and when a single protein is trapped at  $3.6 \mu\text{m}$  for Fig. 5.6. In this case, we again find that  $1/f$  noise has increased by a factor of  $\approx 10^2$  during the initial capture of DNA and RNAP complex and trapping of RNAP when tip is at  $3.6 \mu\text{m}$  above the nanopore .

PSD analysis suggests that these additional current fluctuation appear only due to the presence of RNAP in nanopore. Even if the moving step for tip is 50 nm or 25 nm fluctuations do arise due to RNAP of size  $\approx 18 \text{ nm}$  on DNA.

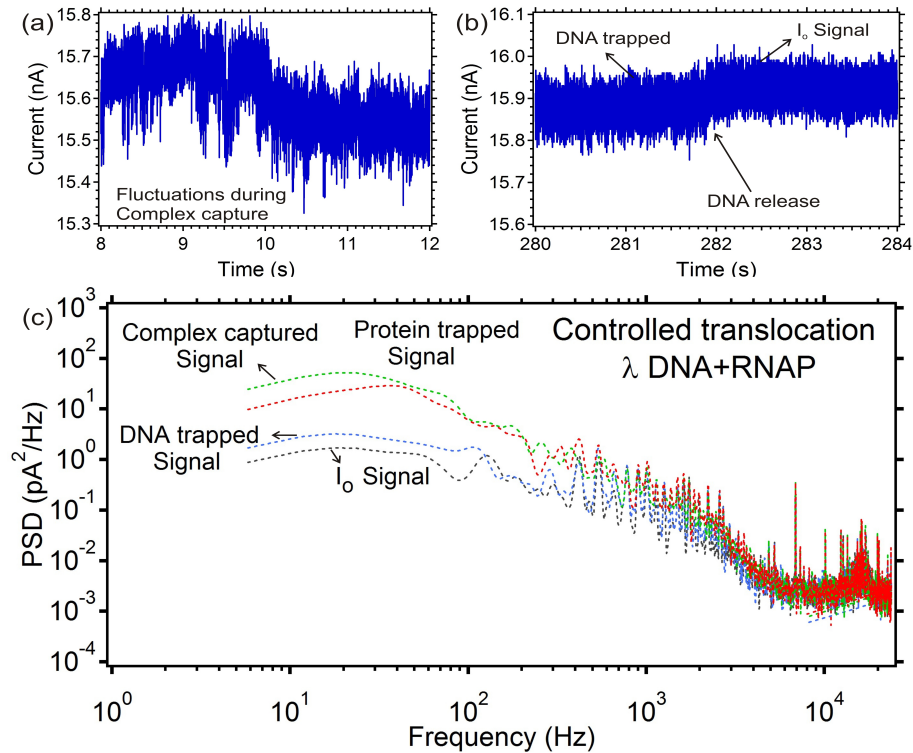


Figure 5.10: (a) A zoomed in view of current blockage signal while DNA+RNAP<sub>complex</sub> is being trapped by the nanopore (initial signal from Fig. 5.6(a)). (b) Zoomed in view of current signal while DNA+RNAP<sub>complex</sub> is being released from the nanopore (corresponds to situation (V) from Fig. 5.6(a)). Fluctuations are observed in the measured current signal during complex capture as compared to the DNA release from the pore. (c) Current power spectral densities are plotted for open pore current measured through 25 nm × 23 nm nanopore at 120 mV when tip is far away from nanopore (corresponds to region after (V) in Fig. 5.6(a)), when the complex is captured (initial current signal between (I) and (II) in Fig. 5.6), when DNA is inside the nanopore while lifting up tip (for a region between (IV) and (V) of Fig. 5.6), and when a single RNAP bound to DNA is trapped inside the nanopore which corresponds to the point (III) in Fig. 5.6.

### 5.3.7 TFFSP system Resolution to detect binding sites

Once  $\lambda$  DNA+RNAP complex is captured inside the pore, the tip has been approached down and lifted up from membrane several times and several current blockage traces are obtained from the same molecules. We observed that mean position of RNAP bound  $\lambda$  DNA is  $6.975 \mu\text{m} \pm 0.0957 \mu\text{m}$  (or 27999 bp  $\pm$  319 bp) as shown in Fig. 5.2 and Fig. 5.5. As discussed in the result section of the previous chapter, for promoter site standard deviation is about 3000 bp and it is 15726 bp for pseudo promoter sites. It has been reported earlier that with nanofluidics set up combined with fluorescence measurement, the promoter sites have a minimum standard deviation of 570 bp and for pseudo promoter sites, it is little broader between 1500 bp-550 bp [115]. It has also been observed that pseudo promoter sites have a broader peak than promoter sites [115] similar to what we have observed in Chapter 4. Other groups have also reported the relative binding sites of protein on DNA using free translocation of DNA and protein complexes through solid state nanopores. For example anti-DNA antibodies detection [131] and TF, Zinc finger's (Zif268) binding sites detection [126]. They have observed broad peaks around the binding sites that vary over the full length of DNA molecule. During free translocation experiment, the orientation of the molecule during capture and accelerated exit of DNA through the nanopore limits accurate estimation of the binding sites. However, the SSN-TFFSP setup gives us the exact position of the RNAP from the tip position trace and we can avoid the assumptions made about constant velocity of DNA in the free translocation case. The minimum standard deviation of 320 bp for pseudo promoter sites is obtained first time with our set up of tuning force force sensor combined with solid state nanopores.

## 5.4 Conclusion

We can detect possible binding sites of RNAP on the  $\lambda$  DNA molecule with very high accuracy with Solid State Nanopore combined to tuning fork force sensing probe set up as compared to native Solid State Nanopore setup. The resolution of the system to detect the exact binding site of RNAP is within 100 nm or  $\approx 300$  bp and has highest resolution as compared to other available techniques like fluorescence microscopy [115], AFM [113] etc. We observed current fluctuations as an individual protein had approached the nanopore detection region and were present for about 50 nm-150 nm. We study these fluctuations with current PSD, and find that the amplitude of current PSD has increased by a factor of  $10^2$  in the lower frequency spectrum . We propose that these current variations occur due to Brownian motion of RNAP bound on the  $\lambda$  DNA molecule as a result  $\approx 100$  nm deviation is measured on binding position of RNAP on the  $\lambda$  DNA.

## Chapter 6

### Summary

In this dissertation, a novel approach to characterize binding sites of RNAP holoenzyme on  $\lambda$  DNA molecule using an apparatus that integrates Solid State Nanopore with Tuning Fork Force Sensing Probe have been described. DNA tethered Force Sensing Probe tip is used to control the translocation of DNA through Solid State Nanopores. The  $\lambda$  DNA translocation time has increased from  $\approx 2 \mu\text{s}$  (observed with free translocation of  $\lambda$  DNA from a solid state nanopore) to  $\approx 30$  s. Binding chemistry of DNA to gold coated tip is tested using another experimental set up that combines fluorescence imaging and dielectrophoretic stretching. We have shown that at  $15 \mu\text{m}$  gap between the electrodes maximum stretching of the  $\lambda$  DNA is obtained with  $33 V_{PP}$  AC voltage and a large number of molecules are bound at the end of the tip.

From free translocation data set of  $\lambda$  DNA+RNAP<sub>complex</sub>, we estimated the binding efficiency of RNAP on the  $\lambda$  DNA is  $\approx 42\%$  and the position of the binding sites of RNAP are determined from relative start time of the RNAP peak in an event. RNAP has high tendency to bind around  $38390 \text{ bp} \pm 4639 \text{ bp}$  followed by a second site at  $25920 \text{ bp} \pm 3536 \text{ bp}$ . However these positions include two promoter regions and three pseudo promoter sites respectively. Hence a native nanopore setup can not distinguish between the individual RNAP binding sites.

Finally, we show that the SSN-TFFSP apparatus can sense the individual RNAP binding sites. This apparatus has a measurement accuracy of  $100 \text{ nm}$  or  $300 \text{ bp}$  to detect the binding sites of RNAP. Apart from high resolution measurement of binding sites, new insights on

dynamics of the  $\lambda$  DNA+RNAP<sub>complex</sub> translocation through the Solid State Nanopore at controlled speed are observed.

## Bibliography

- [1] J. D. Watson, F. H. Crick, *et al.*, *Nature* **171**, 737 (1953).
- [2] F. Sanger, (1977).
- [3] E. E. Schadt, S. Turner, and A. Kasarskis, *Human molecular genetics* **19**, R227 (2010).
- [4] L. Liu, Y. Li, S. Li, N. Hu, Y. He, R. Pong, D. Lin, L. Lu, and M. Law, *BioMed Research International* **2012** (2012).
- [5] Y. Wang, Q. Yang, and Z. Wang, *Frontiers in genetics* **5**, 449 (2013).
- [6] D. Branton, D. W. Deamer, A. Marziali, H. Bayley, S. A. Benner, T. Butler, M. Di Ventra, S. Garaj, A. Hibbs, X. Huang, *et al.*, *Nature biotechnology* **26**, 1146 (2008).
- [7] F. Ding, M. Manosas, M. M. Spiering, S. J. Benkovic, D. Bensimon, J.-F. Allemand, and V. Croquette, *nAture methods* **9**, 367 (2012).
- [8] P. Cheng, P. M. Oliver, M. J. Barrett, and D. Vezenov, *Electrophoresis* **33**, 3497 (2012).
- [9] R. Treffer, X. Lin, E. Bailo, T. Deckert-Gaudig, and V. Deckert, *Beilstein journal of nanotechnology* **2**, 628 (2011).
- [10] D. W. Deamer and M. Akeson, *Trends in biotechnology* **18**, 147 (2000).
- [11] G. Church, D. W. Deamer, D. Branton, R. Baldarelli, and J. Kasianowicz, “Measuring physical properties,” (1998), uS Patent 5,795,782.
- [12] J. J. Kasianowicz, E. Brandin, D. Branton, and D. W. Deamer, *Proceedings of the National Academy of Sciences* **93**, 13770 (1996).
- [13] K. Yamashita, Y. Kawai, Y. Tanaka, N. Hirano, J. Kaneko, N. Tomita, M. Ohta, Y. Kamio, M. Yao, and I. Tanaka, *Proceedings of the National Academy of Sciences* **108**, 17314 (2011).
- [14] J. Li, D. Stein, C. McMullan, D. Branton, M. J. Aziz, and J. A. Golovchenko, *Nature* **412**, 166 (2001).
- [15] J. Li, M. Gershow, D. Stein, E. Brandin, and J. Golovchenko, *Nature materials* **2**, 611 (2003).
- [16] B. Cornell, V. Braach-Maksvytis, L. King, P. Osman, B. Raguse, L. Wiczorek, and R. Pace, *NATURE-LONDON-*, 580 (1997).
- [17] W. Coulter, United States Patent Office. Patentiert am **20**, 1953 (1953).
- [18] D. Fologea, J. Uplinger, B. Thomas, D. S. McNabb, and J. Li, *Nano letters* **5**, 1734 (2005).

- [19] G. S. Manning, Quarterly reviews of biophysics **11**, 179 (1978).
- [20] D. Fologea, E. Brandin, J. Uplinger, D. Branton, and J. Li, Electrophoresis **28**, 3186 (2007).
- [21] A. J. Storm, J. Chen, H. Zandbergen, and C. Dekker, Physical Review E **71**, 051903 (2005).
- [22] M. Wanunu, J. Sutin, B. McNally, A. Chow, and A. Meller, Biophysical journal **95**, 4716 (2008).
- [23] A. Meller, L. Nivon, E. Brandin, J. Golovchenko, and D. Branton, Proceedings of the National Academy of Sciences **97**, 1079 (2000).
- [24] D. Stoddart, A. J. Heron, J. Klingelhofer, E. Mikhailova, G. Maglia, and H. Bayley, Nano letters **10**, 3633 (2010).
- [25] E. N. Ervin, G. A. Barrall, P. Pal, M. K. Bean, A. E. Schibel, and A. D. Hibbs, BioNanoScience **4**, 78 (2014).
- [26] M. Faller, M. Niederweis, and G. E. Schulz, Science **303**, 1189 (2004).
- [27] I. M. Derrington, T. Z. Butler, M. D. Collins, E. Manrao, M. Pavlenok, M. Niederweis, and J. H. Gundlach, Proceedings of the National Academy of Sciences **107**, 16060 (2010).
- [28] E. A. Manrao, I. M. Derrington, M. Pavlenok, M. Niederweis, and J. H. Gundlach, PLoS One **6**, e25723 (2011).
- [29] E. A. Manrao, I. M. Derrington, A. H. Laszlo, K. W. Langford, M. K. Hopper, N. Gillgren, M. Pavlenok, M. Niederweis, and J. H. Gundlach, Nature biotechnology **30**, 349 (2012).
- [30] T. Z. Butler, M. Pavlenok, I. M. Derrington, M. Niederweis, and J. H. Gundlach, Proceedings of the National Academy of Sciences **105**, 20647 (2008).
- [31] G. M. Cherf, K. R. Lieberman, H. Rashid, C. E. Lam, K. Karplus, and M. Akeson, Nature biotechnology **30**, 344 (2012).
- [32] S. Kumar, C. Tao, M. Chien, B. Hellner, A. Balijepalli, J. W. Robertson, Z. Li, J. J. Russo, J. E. Reiner, J. J. Kasianowicz, *et al.*, Scientific reports **2** (2012).
- [33] A. S. Mikheyev and M. M. Tin, Molecular ecology resources **14**, 1097 (2014).
- [34] T. Laver, J. Harrison, P. O'Neill, K. Moore, A. Farbos, K. Paszkiewicz, and D. J. Studholme, Biomolecular detection and quantification **3**, 1 (2015).

- [35] A. Storm, J. Chen, X. Ling, H. Zandbergen, and C. Dekker, *Nature materials* **2**, 537 (2003).
- [36] B. M. Venkatesan, B. Dorvel, S. Yemenicioglu, N. Watkins, I. Petrov, and R. Bashir, *Advanced Materials* **21**, 2771 (2009).
- [37] S. Garaj, W. Hubbard, A. Reina, J. Kong, D. Branton, and J. Golovchenko, *Nature* **467**, 190 (2010).
- [38] G. F. Schneider, S. W. Kowalczyk, V. E. Calado, G. Pandraud, H. W. Zandbergen, L. M. Vandersypen, and C. Dekker, *Nano letters* **10**, 3163 (2010).
- [39] C. A. Merchant, K. Healy, M. Wanunu, V. Ray, N. Peterman, J. Bartel, M. D. Fischbein, K. Venta, Z. Luo, A. C. Johnson, *et al.*, *Nano letters* **10**, 2915 (2010).
- [40] S. Liu, B. Lu, Q. Zhao, J. Li, T. Gao, Y. Chen, Y. Zhang, Z. Liu, Z. Fan, F. Yang, *et al.*, *Advanced Materials* **25**, 4549 (2013).
- [41] M. Wanunu, T. Dadoosh, V. Ray, J. Jin, L. McReynolds, and M. Drndić, *Nature nanotechnology* **5**, 807 (2010).
- [42] S. Garaj, S. Liu, J. A. Golovchenko, and D. Branton, *Proceedings of the National Academy of Sciences* **110**, 12192 (2013).
- [43] K. S. Novoselov, A. K. Geim, S. Morozov, D. Jiang, Y. Zhang, S. Dubonos, , I. Grigorieva, and A. Firsov, *science* **306**, 666 (2004).
- [44] U. F. Keyser, B. N. Koeleman, S. Van Dorp, D. Krapf, R. M. Smeets, S. G. Lemay, N. H. Dekker, and C. Dekker, *Nature Physics* **2**, 473 (2006).
- [45] H. Peng and X. S. Ling, *Nanotechnology* **20**, 185101 (2009).
- [46] E. H. Trepagnier, A. Radenovic, D. Sivak, P. Geissler, and J. Liphardt, *Nano letters* **7**, 2824 (2007).
- [47] C. Hyun, H. Kaur, R. Rollings, M. Xiao, and J. Li, *Acs Nano* **7**, 5892 (2013).
- [48] C. Hyun, R. Rollings, and J. Li, *small* **8**, 385 (2012).
- [49] G. King and J. Golovchenko, *Physical review letters* **95**, 216103 (2005).
- [50] U. Mirsaidov, W. Timp, X. Zou, V. Dimitrov, K. Schulten, A. P. Feinberg, and G. Timp, *Biophysical journal* **96**, L32 (2009).
- [51] Q. Zhao, G. Sigalov, V. Dimitrov, B. Dorvel, U. Mirsaidov, S. Sligar, A. Aksimentiev, and G. Timp, *Nano letters* **7**, 1680 (2007).

- [52] A. Singer, M. Wanunu, W. Morrison, H. Kuhn, M. Frank-Kamenetskii, and A. Meller, *Nano letters* **10**, 738 (2010).
- [53] R. Kawano, T. Osaki, H. Sasaki, M. Takinoue, S. Yoshizawa, and S. Takeuchi, *Journal of the American Chemical Society* **133**, 8474 (2011).
- [54] D. Fologea, B. Ledden, D. S. McNabb, and J. Li, *Applied physics letters* **91**, 053901 (2007).
- [55] E. C. Yusko, J. M. Johnson, S. Majd, P. Prangkio, R. C. Rollings, J. Li, J. Yang, and M. Mayer, *Nature nanotechnology* **6**, 253 (2011).
- [56] M. Firnkes, D. Pedone, J. Knezevic, M. Doblinger, and U. Rant, *Nano letters* **10**, 2162 (2010).
- [57] W.-J. Lan, D. A. Holden, B. Zhang, and H. S. White, *Analytical chemistry* **83**, 3840 (2011).
- [58] A. S. Prabhu, T. Z. N. Jubery, K. J. Freedman, R. Mulero, P. Dutta, and M. J. Kim, *Journal of Physics: Condensed Matter* **22**, 454107 (2010).
- [59] L. Bacri, A. Oukhaled, B. Schiedt, G. Patriarche, E. Bourhis, J. Gierak, J. Pelta, and L. Auvray, *The Journal of Physical Chemistry B* **115**, 2890 (2011).
- [60] J. Nivala, D. B. Marks, and M. Akeson, *Nature biotechnology* **31**, 247 (2013).
- [61] R. Smeets, S. Kowalczyk, A. Hall, N. Dekker, and C. Dekker, *Nano letters* **9**, 3089 (2008).
- [62] S. W. Kowalczyk, A. R. Hall, and C. Dekker, *Nano letters* **10**, 324 (2009).
- [63] A. R. Hall, S. van Dorp, S. G. Lemay, and C. Dekker, *Nano letters* **9**, 4441 (2009).
- [64] C. Raillon, P. Cousin, F. Traversi, E. Garcia-Cordero, N. Hernandez, and A. Radenovic, *Nano letters* **12**, 1157 (2012).
- [65] A. Spiering, S. Getfert, A. Sischka, P. Reimann, and D. Anselmetti, *Nano letters* **11**, 2978 (2011).
- [66] A. Sischka, A. Spiering, M. Khaksar, M. Laxa, J. König, K.-J. Dietz, and D. Anselmetti, *Journal of Physics: Condensed Matter* **22**, 454121 (2010).
- [67] B. Hornblower, A. Coombs, R. D. Whitaker, A. Kolomeisky, S. J. Picone, A. Meller, and M. Akeson, *Nature Methods* **4**, 315 (2007).
- [68] B. Dorvel, G. Sigalov, Q. Zhao, J. Comer, V. Dimitrov, U. Mirsaidov, A. Aksimentiev, and G. Timp, *Nucleic acids research* **37**, 4170 (2009).

- [69] A. Ivankin, S. Carson, S. R. Kinney, and M. Wanunu, *Journal of the American Chemical Society* **135**, 15350 (2013).
- [70] P. Jing, F. Haque, D. Shu, C. Montemagno, and P. Guo, *Nano letters* **10**, 3620 (2010).
- [71] H. Fang, P. Jing, F. Haque, and P. Guo, *Biophysical journal* **102**, 127 (2012).
- [72] G. Binnig, H. Rohrer, C. Gerber, and E. Weibel, *Physical review letters* **49**, 57 (1982).
- [73] G. Binning, *Physical Review Letters* **56**, 930 (1986).
- [74] Y. L. Lyubchenko, *Cell biochemistry and biophysics* **41**, 75 (2004).
- [75] B. M. Venkatesan, J. Polans, J. Comer, S. Sridhar, D. Wendell, A. Aksimentiev, and R. Bashir, *Biomedical microdevices* **13**, 671 (2011).
- [76] L. S. Connelly, B. Meckes, J. Larkin, A. L. Gillman, M. Wanunu, and R. Lal, *ACS applied materials & interfaces* **6**, 5290 (2014).
- [77] K. Karrai and R. D. Grober, *Ultramicroscopy* **61**, 197 (1995).
- [78] A. Ruiter, K. Van Der Werf, J. Veerman, M. Garcia-Parajo, W. Rensen, and N. Van Hulst, *Ultramicroscopy* **71**, 149 (1998).
- [79] H. Edwards, L. Taylor, W. Duncan, and A. Melmed, *Rev. Sci. Instrum* **70**, 3614 (1997).
- [80] G. King, J. Lamb, and G. Nunes, *Applied physics letters* **79**, 1712 (2001).
- [81] L. Novotny and B. Hecht, *Principles of nano-optics* (Cambridge university press, 2012).
- [82] F. J. Giessibl, *Applied Physics Letters* **76**, 1470 (2000).
- [83] K. Kim, Y. Seo, H. Jang, S. Chang, M.-H. Hong, and W. Jhe, *Nanotechnology* **17**, S201 (2006).
- [84] B. T. Ledden, *Fabrication of Solid state nanopores using feedback controlled ion beam sculpting techniques*, Ph.D. thesis, University of Arkansas (2004).
- [85] A. Balducci, P. Mao, J. Han, and P. S. Doyle, *Macromolecules* **39**, 6273 (2006).
- [86] J. E. Reiner, J. J. Kasianowicz, B. J. Nablo, and J. W. Robertson, *Proceedings of the National Academy of Sciences* **107**, 12080 (2010).
- [87] S. Y. Noskov, W. Im, and B. Roux, *Biophysical journal* **87**, 2299 (2004).
- [88] J. Li and D. S. Talaga, *Journal of Physics: Condensed Matter* **22**, 454129 (2010).

- [89] D. Y. Ling and X. S. Ling, *Journal of Physics: Condensed Matter* **25**, 375102 (2013).
- [90] P. R. Selvin and T. Ha, *Single-molecule techniques* (Cold Spring Harbor Laboratory Press, 2008).
- [91] M. D. Wang, H. Yin, R. Landick, J. Gelles, and S. M. Block, *Biophysical journal* **72**, 1335 (1997).
- [92] S. B. Smith, L. Finzi, and C. Bustamante, *Science* **258**, 1122 (1992).
- [93] V. Namasivayam, R. G. Larson, D. T. Burke, and M. A. Burns, *Analytical chemistry* **74**, 3378 (2002).
- [94] S. Ferree and H. W. Blanch, *Biophysical journal* **85**, 2539 (2003).
- [95] V. R. Dukkupati and S. W. Pang, *Applied physics letters* **90**, 083901 (2007).
- [96] N. Demyantseva, S. Kuzmin, M. Solunin, S. Solunin, and A. Solunin, *Technical Physics* **57**, 1465 (2012).
- [97] A. Pohl, H. Berg, W. Forster, HE Jacob, W. Jungstand, and P. Miihlig, *Stud. Biophys* **74**, 31 (1978).
- [98] R. Pethig, *Critical Reviews in Biotechnology* **16**, 331 (1996).
- [99] S. Takashima, *Biopolymers* **4**, 663 (1966).
- [100] C. L. Asbury, A. H. Diercks, G. van den Engh, *et al.*, *Electrophoresis* **23**, 2658 (2002).
- [101] M. Washizu and O. Kurosawa, *Industry Applications, IEEE Transactions on* **26**, 1165 (1990).
- [102] N. M. Green, *Advances in protein chemistry* **29**, 85 (1974).
- [103] I. Le Trong, Z. Wang, D. E. Hyre, T. P. Lybrand, P. S. Stayton, and R. E. Stenkamp, *Acta Crystallographica Section D: Biological Crystallography* **67**, 813 (2011).
- [104] P. C. Weber, D. Ohlendorf, J. Wendoloski, and F. Salemme, *Science* **243**, 85 (1989).
- [105] J. DeChancie and K. Houk, *Journal of the American Chemical Society* **129**, 5419 (2007).
- [106] F. Sanger, A. R. Coulson, G. Hong, D. Hill, and G. d. Petersen, *Journal of molecular biology* **162**, 729 (1982).
- [107] C. Hyun, H. Kaur, D. S. McNabb, and J. Li, *Nanotechnology* **26**, 125501 (2015).
- [108] M. L. Bulyk, *Current opinion in biotechnology* **17**, 422 (2006).

- [109] B. Dey, S. Thukral, S. Krishnan, M. Chakrobarty, S. Gupta, C. Manghani, and V. Rani, *Molecular and cellular biochemistry* **365**, 279 (2012).
- [110] S. Weiss, *Science* **283**, 1676 (1999).
- [111] J. Elf, G.-W. Li, and X. S. Xie, *Science* **316**, 1191 (2007).
- [112] Y. Harada, T. Funatsu, K. Murakami, Y. Nonoyama, A. Ishihama, and T. Yanagida, *Biophysical Journal* **76**, 709 (1999).
- [113] Y. Ebenstein, N. Gassman, S. Kim, and S. Weiss, *Journal of Molecular Recognition* **22**, 397 (2009).
- [114] Z. Gueroui, C. Place, E. Freyssingeas, and B. Berge, *Proceedings of the National Academy of Sciences* **99**, 6005 (2002).
- [115] K. Sriram, J.-W. Yeh, Y.-L. Lin, Y.-R. Chang, and C.-F. Chou, *Nucleic acids research* **42**, e85 (2014).
- [116] S. E. Halford and J. F. Marko, *Nucleic acids research* **32**, 3040 (2004).
- [117] J. H. Kim and R. G. Larson, *Nucleic acids research* **35**, 3848 (2007).
- [118] J. Gorman, F. Wang, S. Redding, A. J. Plys, T. Fazio, S. Wind, E. E. Alani, and E. C. Greene, *Proceedings of the National Academy of Sciences* **109**, E3074 (2012).
- [119] Y. Wang, L. Guo, I. Golding, E. C. Cox, and N. Ong, *Biophysical journal* **96**, 609 (2009).
- [120] C. Plesa, S. W. Kowalczyk, R. Zinsmeister, A. Y. Grosberg, Y. Rabin, and C. Dekker, *Nano letters* **13**, 658 (2013).
- [121] C. Raillon, P. Granjon, M. Graf, and A. Radenovic, in *2013 35th Annual International Conference of the IEEE Engineering in Medicine and Biology Society (EMBC)* (IEEE, 2013) pp. 4106–4109.
- [122] A. Han, M. Creus, G. Schurmann, V. Linder, T. R. Ward, N. F. de Rooij, and U. Staufer, *Analytical chemistry* **80**, 4651 (2008).
- [123] B. P. Hudson, J. Quispe, S. Lara-González, Y. Kim, H. M. Berman, E. Arnold, R. H. Ebright, and C. L. Lawson, *Proceedings of the National Academy of Sciences* **106**, 19830 (2009).
- [124] T. Ito, L. Sun, and R. M. Crooks, *Analytical chemistry* **75**, 2399 (2003).
- [125] M. Mihovilovic, N. Hagerty, and D. Stein, *Physical review letters* **110**, 028102 (2013).

- [126] A. Squires, E. Atas, and A. Meller, *Scientific reports* **5** (2015).
- [127] C. Plesa, N. van Loo, P. Ketterer, H. Dietz, and C. Dekker, *Nano letters* **15**, 732 (2014).
- [128] S. Kasas, N. H. Thomson, B. L. Smith, H. G. Hansma, X. Zhu, M. Guthold, C. Bustamante, E. T. Kool, M. Kashlev, and P. K. Hansma, *Biochemistry* **36**, 461 (1997).
- [129] R. C. Rollings, *The Geometry and Sensitivity of Ion-Beam Sculpted Nanopores for Single Molecule DNA Analysis* (2013).
- [130] A. Mathelier and W. W. Wasserman, *PLoS Comput Biol* **9**, e1003214 (2013).
- [131] C. Plesa, J. W. Ruitenbergh, M. J. Witteveen, and C. Dekker, *Nano letters* **15**, 3153 (2015).
- [132] R. Rollings, E. Graef, N. Walsh, S. Nandivada, M. Benamara, and J. Li, *Nanotechnology* **26**, 044001 (2015).
- [133] X. Liu, M. M. Skanata, and D. Stein, *Nature communications* **6** (2015).
- [134] S. Nekolla, C. Andersen, and R. Benz, *Biophysical journal* **66**, 1388 (1994).
- [135] S. M. Bezrukov, L. Kullman, and M. Winterhalter, *FEBS letters* **476**, 224 (2000).
- [136] T. K. Rostovtseva and S. M. Bezrukov, *Biophysical journal* **74**, 2365 (1998).
- [137] E. M. Nestorovich, C. Danelon, M. Winterhalter, and S. M. Bezrukov, *Proceedings of the National Academy of Sciences* **99**, 9789 (2002).
- [138] S. M. Bezrukov and J. J. Kasianowicz, *Physical review letters* **70**, 2352 (1993).
- [139] R. M. Smeets, U. F. Keyser, N. H. Dekker, and C. Dekker, *Proceedings of the National Academy of Sciences* **105**, 417 (2008).
- [140] S. Heerema, G. Schneider, M. Rozemuller, L. Vicarelli, H. Zandbergen, and C. Dekker, *Nanotechnology* **26**, 074001 (2015).
- [141] J. B. Johnson, *Physical review* **32**, 97 (1928).
- [142] H. Nyquist, *Physical review* **32**, 110 (1928).
- [143] K. Benndorf, in *Single-Channel Recording* (Springer, 1995) pp. 129–145.
- [144] R. Sherman-Gold, *The Axon Guide* (Molecular Devices, 3rd edition, 2007).
- [145] J. D. Uram, K. Ke, and M. Mayer, *ACS nano* **2**, 857 (2008).

- [146] V. Tabard-Cossa, D. Trivedi, M. Wiggin, N. N. Jetha, and A. Marziali, *Nanotechnology* **18**, 305505 (2007).
- [147] M. R. Powell, I. Vlassiuk, C. Martens, and Z. S. Siwy, *Physical review letters* **103**, 248104 (2009).
- [148] M. R. Powell, C. Martens, and Z. S. Siwy, *Chemical Physics* **375**, 529 (2010).
- [149] M. Powell, N. Sa, M. Davenport, K. Healy, I. Vlassiuk, S. Letant, L. Baker, and Z. Siwy, *The Journal of Physical Chemistry C* **115**, 8775 (2011).
- [150] F. N. Hooge, *Physics letters A* **29**, 139 (1969).